The Balloon-borne Large Aperture Submillimeter Telescope: BLAST

by

Enzo Pascale

A thesis submitted in conformity with the requirements
for the degree of Doctor of Philosophy
Graduate Department of Physics
University of Toronto

Your file Votre référence
ISBN: 978-0-494-39633-9
Our file Notre référence
ISBN: 978-0-494-39633-9

Abstract

The Balloon-borne Large Aperture Submillimeter Telescope: BLAST

Enzo Pascale

Doctor of Philosophy

Graduate Department of Physics

University of Toronto

2007

The Balloon-borne Large Aperture Submillimeter Telescope (BLAST) is a sub-orbital submillimetric experiment designed to survey the sky with a 2 m Cassegrain telescope, using large-format bolometric detector arrays in three wavebands centered at 250 μm, 350 μm, and 500 μm. The number of detectors, and diffraction-limited beams of 30″ FWHM at 250 μm give BLAST unprecedented mapping speed and resolution.

Flown from a high-altitude balloon-borne platform, BLAST is designed to study the evolutionary history and processes of star formation in local galaxies (including the Milky Way), and galaxies at cosmological distances.

BLAST is a technology demonstrator for the SPIRE instrument on the Herschel satellite, and flew from Fort Sumner, NM (2003), in a 24 h test flight; from Kiruna, Sweden (2005), where 100 h of data were collected on Galactic targets; and from McMurdo, Antarctica (2006), where 250 h of data were collected in both Galactic and extragalactic surveys.

This work reviews BLAST and the experimental techniques we have implemented, which led to the success of the project. I also discuss in greater details those aspects of BLAST that will be of relevance for future experiments.

I discuss the diffraction limited optics and the detector system that provide point-source sensitivities of 250 mJy$\sqrt{s}$ in each waveband, and resolutions from 30″ to 60″, from

250 μm to 500 μm, respectively.

A new pointing system, based on a day-time star tracker and gyroscopes, was developed, and a pointing reconstruction pipe-line implemented, allowing attitude determination with an accuracy of better than 5″ RMS, at a rate of 100 Hz.

The number of detectors, the large volume of data, and the correlations among channels, common in a multi-pixel focal plane, required the implementation of a new data reduction pipe-line. The output of the pipe-line are calibrated maps and simulated maps which enable Monte Carlo analysis.

This work also presents the in-flight performance of the instrument. While the design noise was achieved in both the Kiruna and McMurdo flight, the optics performed correctly only during the Antarctic flight.

Contents

Table of Acronyms

ACS	Attitude Control System
ADU	Analog to Digital Unit
AGN	Active Galactic Nucleus
BLAST	Balloon Borne Large Aperture Submillimeter Telescope
CMB	Cosmic Microwave Background
CSBF	Columbia Scientific Balloon Facility
CTE	Coefficient of Thermal Expansion
DAS	Data Acquisition System
EKF	Extended Kalman Filter
FIR	Far InfraRed
FIRB	Far InfraRed Background
FOG	Fiber Optic Gyroscope
FOV	Field of View
FTS	Fourier Transform Spectrometer
FWHM	Full Width at Half Maximum
IF	Inner Frame of the telescope
IRAM	Instituto de Radioastronomia Millimétrica
IRAS	Infrared Astronomical Satellite
JCMT	James Clerk Maxwell Telescope, Manua Kea, HW
JFET	Junction Field Effect Transistor
LDB	Long Duration Balloon
LOS	Line-of-Sight
$L_{\rm FIR}$	Far InfraRed Luminosity
$M_{\odot}$	Mass of the Sun
MAMBO	Max-Planck Millimeter Bolometer array
MMSE	Minimum Mean-Square Error
NEFD	Noise Equivalent Flux Density
OF	Outer Frame of the telescope
PSD	Power Spectral Density
QE	Quantum Efficiency
SC	Source Counts
SCUBA	Submillimetre Common-User Bolometer Array
SED	Spectral Energy Distribution
SF	Star Formation
SFR	Star Formation Rate
SNR	Signal-to-Noise Ratio
RMS	Root Mean Square
ULIRG	Ultra-Luminous InfraRed Galaxy
ZPD	Zero Path Difference

Chapter 1

Introduction

1.1 Science Case Overview

The extragalactic Far Infrared Background (FIRB), discovered and constrained with the FIRAS and DIRBE instruments [1, 2], on the Cosmic Microwave Background Explorer (COBE) mission, shows that the integrated background in the FIR-submillimetre is comparable with that in the optical-Near IR. This background, unlike the Cosmic Microwave Background (CMB), is a repository of all the stellar energy emitted during the history of the Universe, in addition to Black Hole accretion and Active Galactic Nuclei (AGN), which constitute a significant but somewhat less important component. Thus, measuring the contribution of one class of objects to the background, enables us to understand the importance that this class has had in the Star Formation history of the Universe.

Elliptical galaxies contains 75% of all the observed stars, but they do not present evolution at moderate redshifts. Already old at redshifts $\sim$ 1, a high star formation rate of several hundreds to thousands of $M_{\odot}$/year is required at high redshifts, in order to build the amount of stars observed in the available cosmolgical time. Since star forma-

tion arises in optically obscured, dust-enshrouded regions, the history of how these stars formed must have left an imprint in the FIRB (particularly in the submillimetre).

Pioneering blind and targeted surveys conducted with SCUBA [3, 4] at 850 μm and 450 μm from the JCMT 15 m telescope at Mauna Kea, Hawaii, and MAMBO [5] at 1.2 mm from the IRAM 30 m telescope on Pico Veleta, Spain, discovered a large number of highly luminous infrared objects. These sources are spread over a redshift range from 1 to 5 with a peak at $z \sim 2-3$. Given the favorable k-correction in the submillimetre [6], it was also possible to estimate the FIR rest frame luminosity of these sources. Values $L_{FIR} \geq 10^{12} L_{\odot}$ are found [7, 8, 6], suggesting IRAS ULIRG-like [9, 10] dust-enshrouded objects, whose high IR luminosity is due to UV energy (emitted by star being formed and AGN) reprocessed by dust, and a typical SFR of $\sim 300 M_{\odot}$/year.

Source Counts (SC) from IRAS/ISO/SCUBA show a strong evolution of the luminosity function with redshift. Observations in the submillimetre are constrained to a few atmospheric wavelength windows, and very small patches of the sky. SC cannot be constrained at both the bright and faint end of the submillimetre flux densities. In particular, observations of larger sky patches can constrain the high-luminosity, low-density end of the SC curve, which carries information about the clustering properties of the submillimetre population [11]. Higher resolution, deeper surveys can, conversely, constrain the faint end of the SC and resolve the submillimetric portion of the FIRB. The information on the clustering properties of the submillimetric sources are of fundamental importance for understanding how these surces formed and evolved.

1.2 Science Goals

BLAST is the first long-duration balloon-borne telescope to take advantage of the bolometric focal-plane arrays being developed for the SPIRE instrument on *Herschel* [12].

BLAST provides the first surveys at 250 μm, 350 μm, and 500 μm, and significantly extends the wavelength range, sensitivity, and area of existing ground-based extragalactic and Galactic surveys.

Taking advantage of the unique spectral-coverage, resolution and sensitivity, the primary scientific goals of BLAST are i) to conduct both confusion-limited and shallow wide-area extragalactic surveys to constrain the redshift-distribution, star formation history and evolution of optically-obscured luminous galaxies, by measuring robust photometric-redshifts [13], and the spatial clustering of this population; ii) to improve our understanding of the earliest stages of star formation by determining the physical properties and mass-function of cold pre-stellar cores, and the efficiency of star formation within different Galactic environments; and iii) to investigate the nature and structure of the interstellar medium by making high resolution maps of diffuse Galactic emission.

BLAST had a test flight in 2003 and two science flights: the first from Kiruna, Sweden in 2005, and the second from McMurdo, Antarctica in 2006.

In the Sweden 100 h flight (Figure 1.1), BLAST targeted five star-forming regions, including the well-studied Cygnus–X field, as well as three regions of intermediate/high-velocity cirrus, the Cas–A supernova remnant, several individual bright targets, and one extragalactic field in the ELAIS–N1 region.

In the Antarctic 250 h flight (Figure 1.1), BLAST conducted deep, confusion-limited (0.8 deg-sq) and shallow (10 deg-sq) extragalactic surveys. Detection of thousands of distant submillimetric galaxies is expected, thus providing the first significant statistical sample of these objects. Deep (40 deg-sq) and larger (200 deg-sq) maps of the Galactic plane were also collected to study the physical properties of star formation, and of dust in the Interstellar Medium.

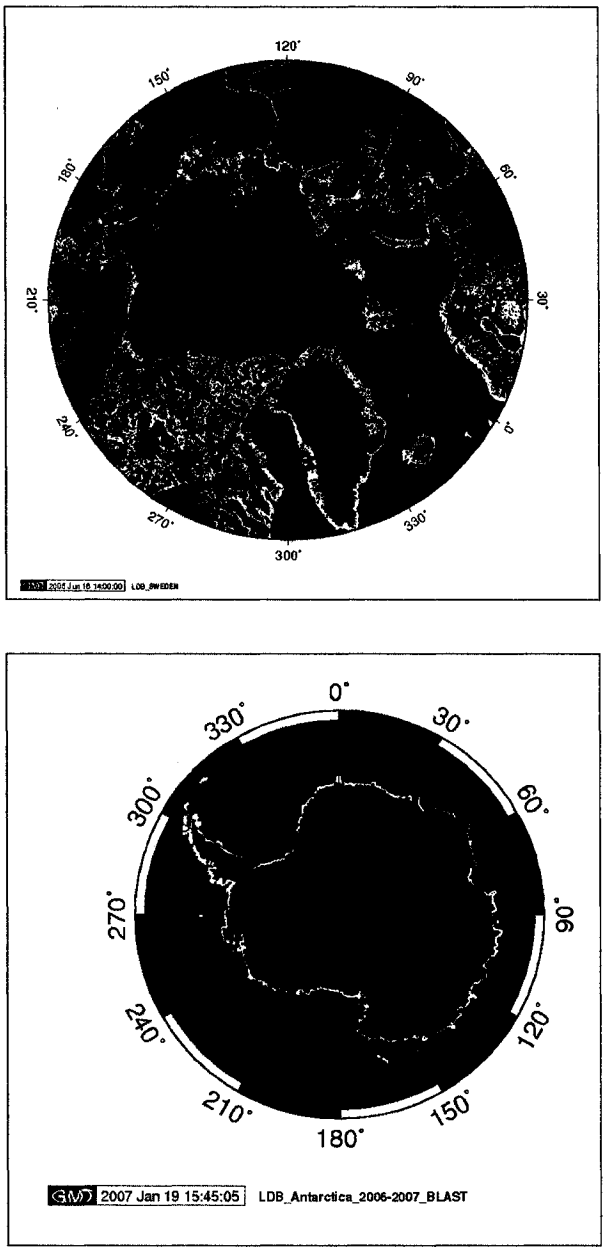

Figure 1.1: GPS flight paths for the two science flights. In the first flight (top panel), BLAST flew from Kiruna, in the northern part of Sweden, to Victoria Island, Canada; launched on June 12th 2005, it landed after 4.5 days of flight across the Atlantic. In the second science flight (bottom panel), BLAST was launched on December 21th 2006, and flew over the Antarctic continent, landing after 12.5 days.

1.3 Thesis Overview

BLAST is an innovative and technically challenging experiment. State-of-the-art technology was implemented in the various flights and several subsystems of the payload are

being duplicated by other projects.

I had a leadership role in the integration and deployment of the experiment in all the flight campaigns. Therefore, I have been involved in almost all aspects of BLAST.

The whole experiment is described in Appendix B, where Pascale *et al.* (2007) is included. In this thesis I will review in more detail those aspects of BLAST that will be of relevance for the next generation of sub-orbital experiments.

I will begin Chapter 2 with a review of the BLAST optical system, and I will continue describing the design of the pointing system. Chapter 3 contains a discussion on how the pointing system is used to achieve a reconstruction of the line of sight with less than $5''$ RMS accuracy.

Chapter 4 contains a characterization of the optical bandpass, and in Chapter 5 the pipeline implemented to analyze BLAST is reviewed; the instrument performance in the Kiruna 2005 flight is discussed there as well.

This work will make use of the data collected in the Kiruna campaign. The McMurdo flight will be only briefly mentioned for completeness.

Chapter 2

Instrument Overview

BLAST observes the sky at 250 μm, 350 μm, and 500 μm, with a 2 m Cassegrain telescope. As the atmosphere is opaque at these wavelengths due to water vapor content, BLAST operates at stratospheric balloon altitude (about 38 km) where the air pressure is $\sim$ 5 mbar. While the main scientific target is the population of submillimetre galaxies from moderate to high redshifts, as an observatory, the telescope can image many different sources of galactic origin, from star-forming regions to diffuse cold dust. The optics and the detectors are optimized for mapping speed, angular resolution and frequency coverage of the most interesting broad-band features at these wavelengths. Long integration times are required to detect the faint submillimetre galaxies, and many hours are needed to scan large, bright regions of our galaxy. Moreover, having a thermally stable environment is very important when using bolometric detectors. An Arctic or Antarctic long-duration balloon (LDB) flight, in the summer when the Sun never sets, provides such an environment where float altitude can be maintained for many days, and solar panels can be used to power the experiment. A typical LDB flight from the Arctic takes off from Kiruna, Sweden, and lands in Canada after several days. Antarctic flights can last for weeks.

Three bolometric cameras (one at each wavelength) are cooled to 300 mK. The cameras look at the sky through a diffraction-limited optical system made of an F/5 Cassegrain, feeding the detectors through 2 K reimaging optics. Detectors and reimaging optics are housed in an ^{3}He/^{4}He LDB cryostat, the receiver, with hold-time of about 11 days. The beam that each detector projects in the sky is Gaussian in shape, with 30", 42", and 60" FWHM at 250 μm, 350 μm, and 500 μm, respectively.

The instrument is mounted on an alt-azimuth aluminum frame (the gondola, see Figure 2.1) made of an outer frame (OF) providing azimuth directionality and holding an inner frame (IF) for elevation pointing. The OF is hung from the $\sim 800,000\,\mathrm{m}^3$ helium balloon, provided by NASA's Columbia Scientific Balloon Facility (CSBF), through a steel cable and parachute. Control computers, and telemetric systems are mounted on the OF. Data are stored on these computers and partially transmitted through satellite links to the ground station. Sun shields, made of aluminized mylar panels, keep sunlight from heating the telescope, and are mounted on the OF.

The IF is built to house the mirror, the receiver, its readout electronics and the pointing sensors, all rigidly mounted with respect to each other to ensure that mechanical alignment of the systems is maintained throughout the flight.

BLAST has been flown three times: in 2003 from New Mexico for a test flight, in 2005 from Kiruna, Sweden, for the Arctic LDB campaign, and in 2006 from McMurdo, for the Antarctic LDB flight. While the instrument underwent some modifications after each flight, its main subsystems remained constant. This work describes the Sweden instrument, although the McMurdo instrument was different only in the warm optics. Full details on both instruments and flights can be found in [14], included in Appendix B. Here I review in details some of the sub-systems.

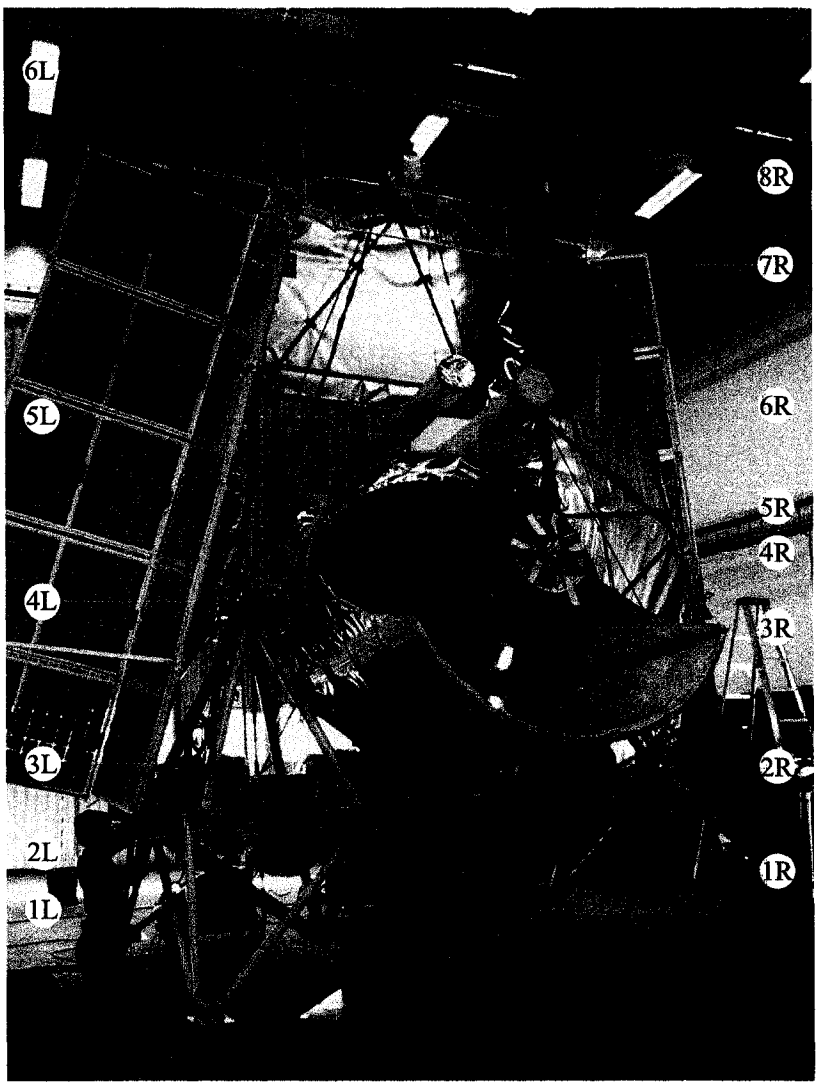

1L	Outer Frame	1R	CSBF Telemetry
2L	Reaction wheel	2R	Flight computers
3L	ACS electronics	3R	Primary mirror
4L	Inner frame bearing	4R	Secondary mirror
5L	Star Cameras	5R	Suspension cable
6L	Attitude GPS antenna	6R	Sun shields
		7R	Solar panels
		8R	Pivot

Figure 2.1: BLAST instrument. This figure portrays the payload ready for launch. Some of the most relevant subsystems are labeled with numbers.

2.1 Optics

The BLAST optical configuration is shown in Figure 2.2. The optical system collects radiation coming from an astrophysical source (object) and focuses on the detectors at the focal plane (image). Key points in the design are high optical efficiency and angular resolution. The optics are optimized to deliver a diffraction-limited image of the sky at the detector focal plane, with 30″, 42″, and 60″ beams at 250 μm, 350 μm, and 500 μm, respectively.

A 2 m, F/5 Cassegrain telescope (M1 and M2) focuses the incoming radiation 20 cm behind the primary's surface, feeding a reimaging optical system (M3, M4, and M5) kept inside a cryostat at a temperature of about 2 K. A Lyot-stop (M4) controls the level of sidelobes, the illumination of the primary, and reject stray radiation that would otherwise illuminate the detectors.

The detectors are fed through smooth-walled conical feed horns in a flat focal plane. Optical frequency bands are selected with the feed horn waveguides, and high-pass filters.

While the main design has not changed throughout the flight campaigns, different optics (M1 to M5) have been flown, after the main telescope suffered damage at launch and recovery during the Kiruna campaign. In the following sections, I will discuss some aspects of the optical system in detail, and refer to Appendix B for further explanations.

2.1.1 Primary Telescope

A Cassegrain is used to provide high telescope speed (low F/#, giving a larger FOV) in a relatively compact volume, which is essential when real estate is a very expensive variable as it is on a stratospheric gondola. In the Kiruna campaign, we used a carbon fiber (CF)

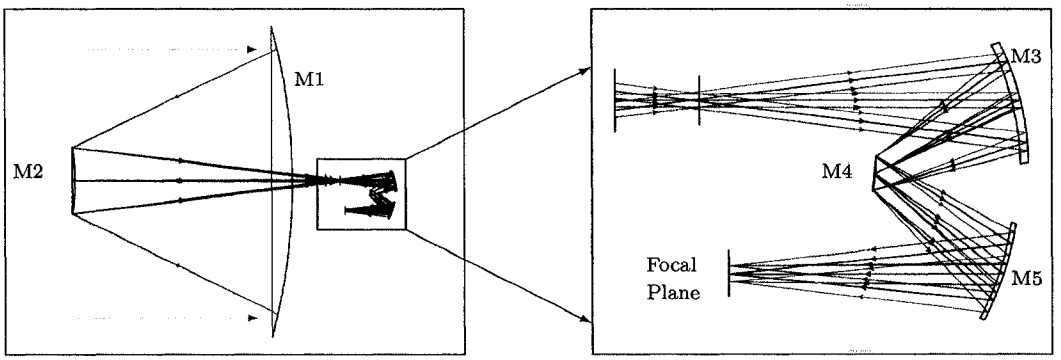

(a) Complete optics. (b) Cold optics.

Figure 2.2: The optical layout of the BLAST05 telescope and receiver are shown on the left. The 2 K optics, located within a cryostat not shown here, are shown on the right. The image of the sky at the input aperture is re-imaged onto the bolometer detector array at the focal plane. The mirror M4 is a Lyot stop defining the illumination of the primary mirror for each element of the bolometer array. The three wavelength bands are defined by a pair of dichroic beamsplitters (not shown) which are located between M5 and the focal plane.

spherical primary (manufactured by Composite Optics Incorporated[1], Figure 2.4a) holding an aluminum correcting secondary with a CF support. The shape of the secondary was designed to compensate for the spherical aberrations of the primary. The primary reflective surface was gold-plated over a SiO_2 (silicon dioxide) coating, giving a roughness 2.4 μm RMS. For such surface, the efficiency is given by the Ruze equation [15]:

$$e^{(-4\pi\sigma/\lambda)^2} \simeq 99\%. \tag{2.1}$$

This loss is negligible with respect to the total Cassegrain efficiency which depends on the diffraction (some of the power is lost in sidelobes) and obstructions (secondary and secondary support), and amounts to $\sim$ 75%. Of the 2 m diameter of the primary, 1.7 m was illuminated, with an edge taper of -30 db.

The COI mirror was damaged in the Kiruna campaign, and for the Antarctic flight we used a 1.8 m aluminum primary (Figure 2.4b). This was the same mirror deployed in

[1]Composite Optics Incorporated (COI), 9617 Distribution Avenue, San Diego, CA 92121.

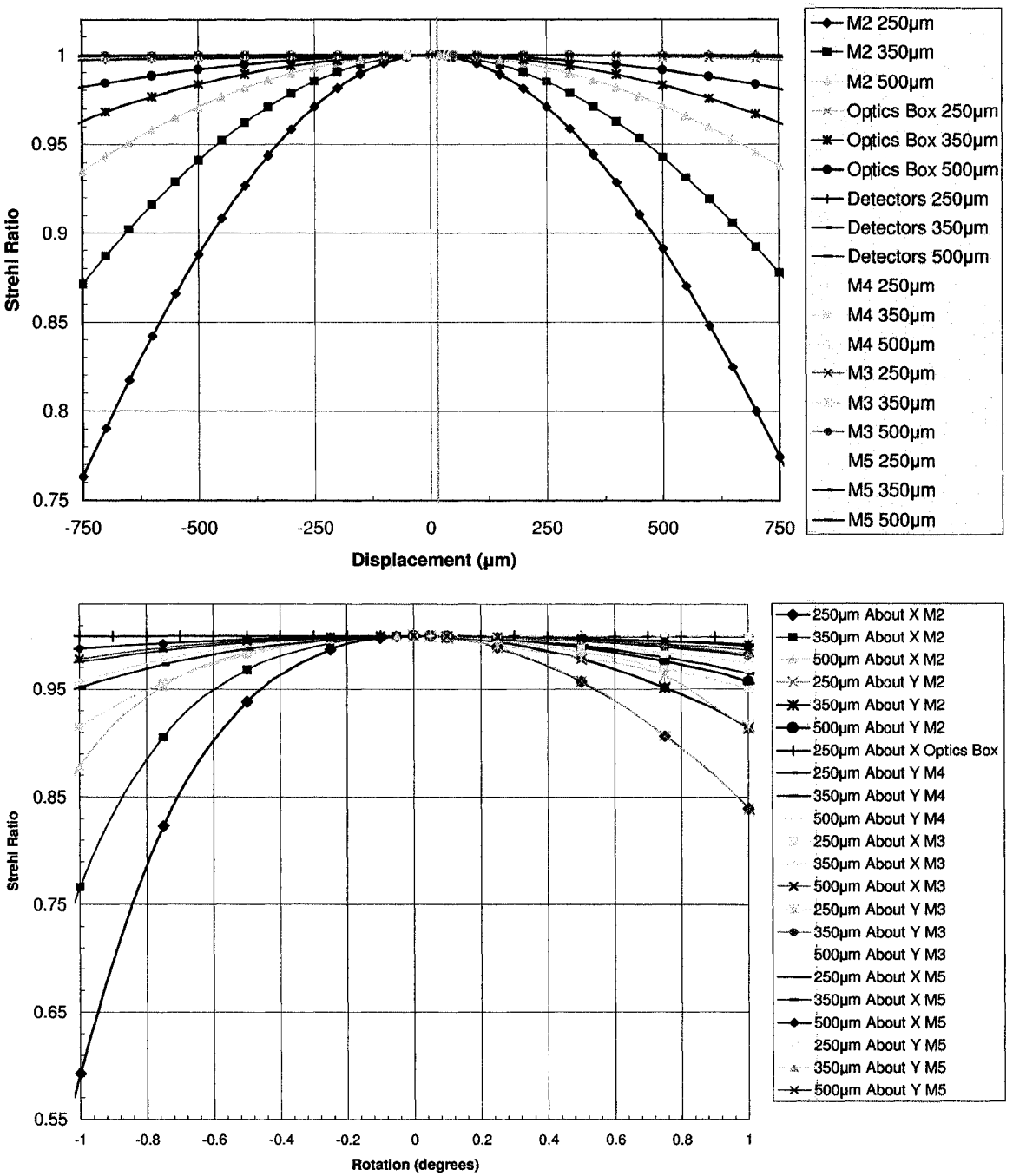

Figure 2.3: Analysis of the tolerances in aligning the optical elements (see Figure 2.2 for a description of the various symbols). The system is forgiving in most of the elements, with the exception of the M1/M2 distance that needs to be set to better than $\lambda/2$.

the test flight, but its surface was re-cut and polished by Lawrence Livermore National Laboratory. This facility was able to machine the aluminum surface to an accuracy

of better than 4 μm RMS. The secondary has been re-cut by Diamond Turning Inc., delivering an optical reflective surface. In this configuration, M2 was supported by four zero CTE carbon fiber struts.

The necessity of having a fast, large-aperture telescope, in a small volume, sets very tight requirements on the alignment of the system. Using commercially available optical design software, we estimated the required accuracy of the optical alignment. The analysis was carried requiring a Strehl ratio [2] larger than 0.99 to maximize point source sensitivity and angular resolution (and maintain low sidelobes at the same time). The results are summarized in Figure 2.3. The correct alignment of M1/M2 is the most critical, with the distance between the primary and the secondary to be maintained within $\lambda/2$, or efficiency is seriously compromised. To reach this accuracy, for the McMurdo campaign we implemented a refocussing system. The secondary mirror was held by three motorized actuators that allowed axial displacement of M2 relative to M1 with an accuracy of $\simeq 1\,\mu$m. The focus of the system was verified in flight, and had to be corrected by 300μm relative to the position set at launch.

2.1.2 Reimaging Optics

The Cassegrain focus is located about 20 cm behind the primary surface. The collected radiation is split, and focussed on three flat focal planes where the detector arrays are housed. We use reimaging optics made of two off-axis mirrors (M3 and M5) that feed smooth-walled conical horns (at the focal plane in Figure 2.2, but not shown there) at F/5, and correct aberrations from the main telescope. A third mirror (M4) is placed between M3 and M5, where an image of the primary is formed. This provides a Lyot-

[2] The Strehl ratio is one commonly used measure of optical image quality for very high quality imaging systems. The Strehl ratio is defined as the peak intensity of the diffraction PSF divided by the peak intensity of the diffraction PSF in the absence of aberrations.

stop that controls the illumination of the primary. The compact horns have a broad angular response. In order to make sure that stray radiation is rejected, the Lyot stop is designed to ensure that all the unwanted rays from the horns end in a cold (T = 2 K) dark stop. For this, the reimaging optics are held inside an emissive, and light tight box (Figure 2.4c), inserted inside a long-duration cryostat (Figure 2.4d), with only one aperture located at the Cassegrain focus. The off-axis nature of M3/M5 allows enough space for two dichroic beam splitters to be placed in front of the focal plane, making simultaneous measurements possible with all three arrays.

2.1.3 Bolometric Detectors and Feeds

Silicon-nitride micromesh (spider-web) bolometric detector arrays are used at each wavelength. The arrays contain 149, 88, and 43 detectors at 250 μm, 350 μm, and 500 μm. The detectors are $2F\lambda$ spaced to maximize optical efficiency [16] to point sources and are similar to the ones that will be flown on SPIRE.

Smooth-walled conical feeds collect the re-imaged radiation emerging from M5 onto the bolometer, and provide a tapered illumination of M4 (see [17] for a relation between feed sizes and field taper). A circular waveguide at the throat of each horn rejects wavelengths longer than the waveguide size, thus providing a frequency high-pass filter (see Section 4.1) Feeds details are given in Table 2.1 and Figure 2.5.

2.2 Attitude Sensors

The primary pointing sensors for BLAST are a pair of CCD-based star cameras which provide absolute pointing, and Fiber-Optic rate Gyros (FOGs) that provide velocity information. The gyro angular velocities can be integrated to interpolate the gondola

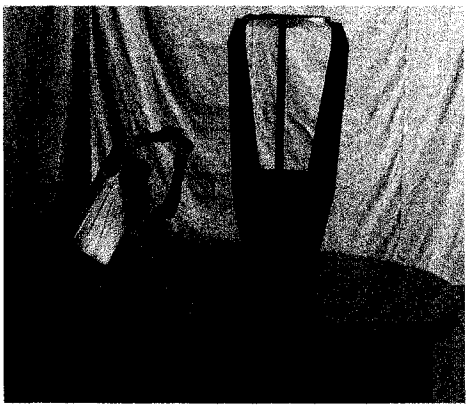

(a) The BLAST 2 m spherical primary. This Carbon Fiber mirror was flown in Kiruna in 2005.

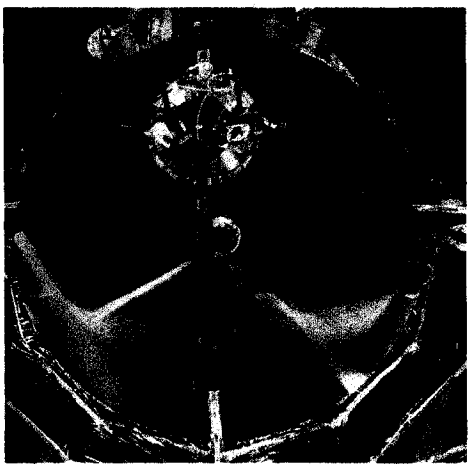

(b) The 1.8 m parabolic aluminum primary flown in both the test flight, in 2003, and in the Antarctic flight, in 2006.

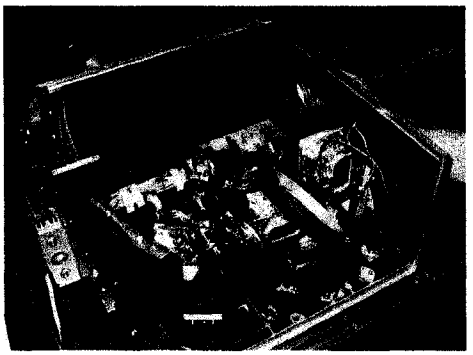

(c) The 2 K optics box is laid on a side and opened, to show the details of the reimaging mirrors and filters.

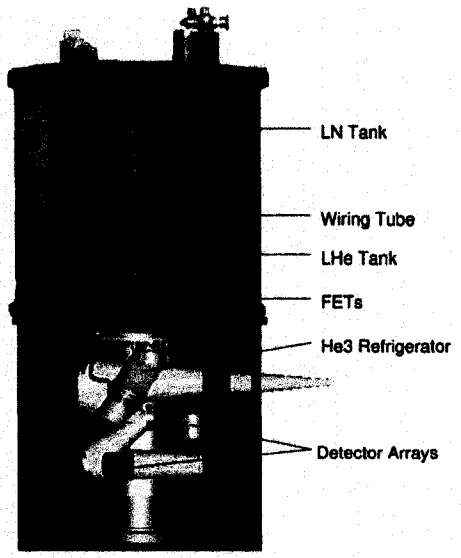

(d) The cryostat encloses the optics box and the detectors keeping them at 2 K, and 300 mK, respectively, for more than 11 days.

Figure 2.4: BLAST optics and cryogenic receiver.

attitude between star camera solutions. Coarse attitude determination is provided by several additional sensors. In elevation, there is an encoder on the elevation axis, and a tilt sensor on the inner frame. In azimuth, there is a Sun sensor, a differential GPS unit, and a magnetometer. The system provides post-flight pointing reconstruction to

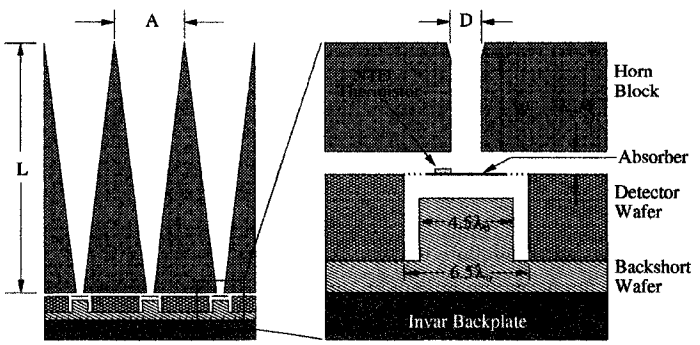

Figure 2.5: Cross section of BLAST detector array, showing the feed horns, circular waveguide section and detector cavity (from [18]).

λ_o (μm)	L (mm)	A (mm)	D (μm)	Waveguide Length (μm)
250	23.68	2.40	171	500
350	32.75	3.23	239	700
500	46.36	4.90	342	1000

Table 2.1: Feed horn and cavity dimensions

$< 5''$ RMS.

2.2.1 Day Time Star Tracker

BLAST developed a new star tracker that can be used during the day at balloon float altitudes (about 38 km). The star tracker is BLAST's main absolute-pointing sensor.

The $30''$ diffraction-limited beam at 250 μm requires the telescope absolute-pointing reconstruction to be accurate to better than a fifth of the beam.

Therefore the star tracker has been optimized with the following goals:

- it has to provide an absolute pointing accuracy of $\sim 5''$;

it has to allow integration times to be short enough to avoid significant smearing

it has to allow integration times to be short enough to avoid significant smearing at the maximum normal scan angular-velocity of the gondola ($0.1^\circ\,s^{-1}$, see Appendix B);

- the system must *always* detect stars to calibrate gyroscope drifts;

- the frequency of the solutions must be high enough to control the $1/f$ random walk noise in the integrated gyroscopes.

Our star sensor is designed to provide pointing solutions to better than $2''$ RMS, at a rate of one solution every 1.5 s. Gyroscopes (see Sections 2.2.3 and 3.5) are used to extrapolate the pointing solution between two consecutive star tracker solutions.

Two star trackers have been implemented: one based on the Kodak KAF 1401e, and one on the Sony ICX285AL CCD sensors (see Table 2.2; see [19] for a more detailed discussion about the hardware implementation).

In the following sections I review the theory of operation of these sensors, and their in-flight performance.

Star Intensity

Let I_λ be the flux of a star, outside Earth's atmosphere, at the wavelength λ. The bolometric magnitude, m_b, is defined as [20]

$$m_b = -2.5 \log\left\{ -19 + \int_0^\infty I_\lambda \, d\lambda \right\} \tag{2.2}$$

CCD	KAF 1401e	Sony ICX285AL
Pixels	1312 × 1024	1360 × 1036
Pixel Size	6.8 μm × 6.8 μm	6.45 μm × 6.45 μm
Quantum Efficiency at Peak Response	60%	60%
Dynamic Range	14 bit	12 bit
Well Depth	45,000 e^-	18,000 e^-
Pixel FOV	7″	7″
Camera FOV	2.5° × 2°	2.5° × 2°
Lens Diameter	100 mm	
Lens F/#	2	
Lens Optical Efficiency	0.8	
Filter Cut-off	600 nm	

Table 2.2: Specifications of the two CCD Star Cameras. Though both CCDs are nearly identical, the Kodak one has deeper pixel wells. It was also found to have a lower measured optical efficiency, significant readout noise and gain variations across the chip compared to the Sony sensor. However, despite requiring longer integration times to reach a given signal-to-noise ratio, the greater dynamic range of the Kodak afforded by the extra well depth enabled it to function in backgrounds 1.6 times larger than for the Sony. The shape of the spectral response for each camera is similar with peaks in the range from 400 nm to 850 nm (see Figure 2.6).

when I_λ is measured in $W\ m^{-2}\ nm^{-1}$. The visual magnitude, m_v, is defined in a similar way, with the integral of I_λ restricted to the visual wavelengths.

The bolometric correction is defined as the difference between the visual and the bolometric magnitudes:

$$BC = m_v - m_b \tag{2.3}$$

and it is always negative. Therefore, the star flux outside the Earth's atmosphere can be expressed as

$$I_{tot} = 10^{-0.4\,(m_v+BC+19)} \left(\frac{\mathrm{W}}{\mathrm{m}^2}\right) \tag{2.4}$$

Assuming that stars radiate with a black body spectral shape at a temperature $T = T_{eff}$, then

$$I_\lambda = 10^{-0.4\,(m_v+BC+19)} \frac{BB(T_{eff},\lambda)}{\int BB(T_{eff},\lambda)\,d\lambda} \tag{2.5}$$

$$= 10^{-0.4\,(m_v+BC+19)} \frac{BB(T_{eff},\lambda)}{\sigma T_{eff}^4/\pi} \left(\frac{\mathrm{W}}{\mathrm{m}^2\,\mathrm{nm}}\right), \tag{2.6}$$

where $BB(T_{eff},\lambda)$ is the black body function, σ is the Stefan–Boltzmann constant, and λ is given in nm.

Diffuse Sky Background

Sunlight in the visible and near IR is scattered by the atmosphere through:

- Molecular scattering: it is a Rayleigh $\sim \lambda^{-4}$ scattering.
- Dust and aerosol scattering: negligible above 30 km of altitude.

Therefore, only Rayleigh scattering needs to be considered at balloon altitudes.

The Thomson scattering differential cross section per molecule is (see [21])

$$\frac{d\sigma_{\mathrm{T}}(\lambda)}{d\Omega} = \frac{3}{16\pi}\sigma_{\mathrm{T}}(\lambda)\,(1+\cos^2(\theta)) \tag{2.7}$$

where θ is the angle between the Sun and the line of sight and $\sigma_{\mathrm{T}}(\lambda)$ is the total Thomson scattering cross section per molecule at the wavelength λ.

If $f_{\odot\lambda}$ is the solar flux outside the Earth's atmosphere, the sky brightness is then

$$\begin{aligned} B_\lambda &= f_{\odot\lambda}\frac{d\sigma_{\mathrm{T}}(\lambda)}{d\Omega}\int_{\mathrm{LOS}} N dl \\ &= f_{\odot\lambda}\chi(e_0)\frac{d\sigma_{\mathrm{T}}(\lambda)}{d\Omega}\int N dh \\ &= f_{\odot\lambda}\chi(e_0)\frac{\mathrm{p}}{m_0\, g}\frac{d\sigma_{\mathrm{T}}(\lambda)}{d\Omega} \end{aligned} \tag{2.8}$$

In the this expression, the integral $\int_{\mathrm{LOS}} N dl$ is over the line-of-sight (LOS) and represents the total number of scattering molecules per unit surface along the LOS. It is expressed as $\chi(e_0)\int N(h)dh$, where the integral is now over the altitude. $\chi(e_0)$ is the air mass, described in [20], and it is a function of the elevation e_0 of the LOS. The differential cross section was not included in the integral sign, since it does not vary too much with the altitude. Finally, p is the pressure at balloon float altitude and m_0 and g are the mean molecular mass and the gravitational acceleration, respectively.

The exponential absorption coefficients per unit pressure are defined as $k_\lambda = \sigma_{\mathrm{T}}(\lambda)/(m_0\, g)$ (see [22] for their numerical values). Therefore

$$B_\lambda = \frac{3}{16\pi}\,\mathrm{p}\,k_\lambda\, f_{\odot\lambda}\,\chi(e_0)\,(1+\cos^2\theta). \tag{2.9}$$

A fraction of the sunlight can also be scattered off the ground and then scattered again by the sky. This contribution can be as important as the sunlight that is directly scattered. This extra term adds a DC component to the above equation, and is proportional to the

Sun elevation.

Equation 2.9 shows that the sky diffuse background is directly proportional to the atmospheric pressure p, to the air mass $\chi(e_0)$, and it is minimum at 90° from the Sun.

Principle of Operation

The sky background at balloon altitudes is a fraction of a percent of that at sea level, but it is still quite bright, glowing much like the sky at dusk from sea level. The Rayleigh nature of the scattering, and the Rayleigh-Jeans emission of the Sun and the star, make the total contrast between the two increase as $\sim \lambda^4$.

Equation 2.9 is evaluated using Modran [23] and it is plotted in Figure 2.6 along with the CCD spectral response [3]. A red, highpass filter at 600 nm cuts off the bright end of the sky background. The output signal from each CCD's photo-element can be written as

$$S_{\text{tot}} = S_{\text{star}} + S_{\text{sky}} + S_{\text{dark}} + \text{Noise} \tag{2.10}$$

with

$$S_{\text{star}} = \frac{\pi}{4} R \eta \frac{\Phi^2}{n} T_{\text{int}} \int T_\lambda I_\lambda d\lambda \tag{2.11}$$

$$S_{\text{sky}} = \frac{\pi}{4} R \eta \Phi^2 \Omega T_{\text{int}} \int T_\lambda B_\lambda d\lambda \tag{2.12}$$

$$\text{Noise} = \sqrt{S_{\text{sky}} + S_{\text{star}} + S_{\text{dark}}} \simeq \sqrt{S_{\text{sky}}}. \tag{2.13}$$

Here, S_{dark} is the dark current of the CCD sensor, and

[3] Multiply the CCD spectral response by the peak quantum efficiency (QE) given in Table 2.2 to estimate the QE at each wavelength.

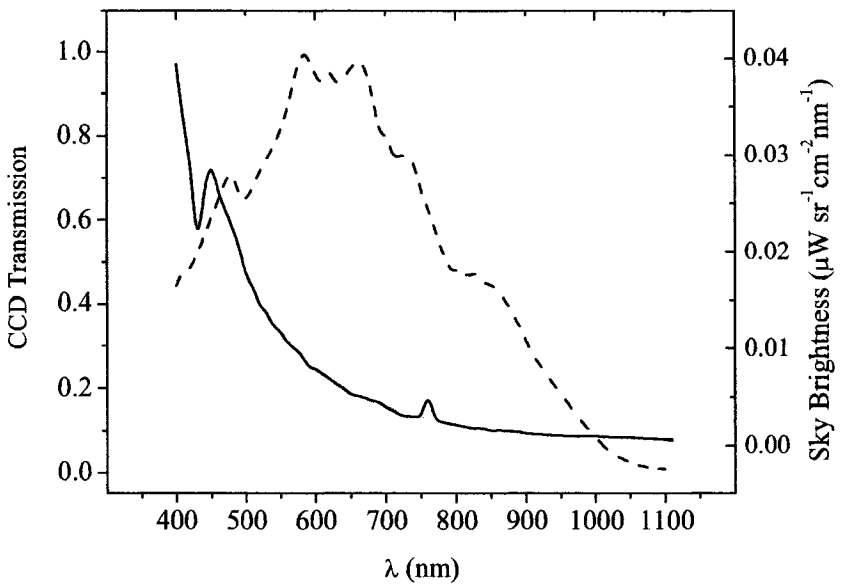

Figure 2.6: The brightness of the sky background at balloon altitude is plotted as a solid line. The overlaid dashed line is the CCD spectral response. The daytime star tracker uses the near infrared sensitivity (longward of 600 nm) of the CCD sensor to enhance the star signal over the background. The sky background is calculated for a reference geometry where: $e_\odot = 30°$, $e_0 = 45°$, altitude = 38 km, and an azimuth of the camera line-of-sight at 180° from the Sun.

Ω	the pixel solid angle;
Φ	the the input lens diameter;
T_{int}	the exposure time;
T_λ	the CCD spectral response, plotted in figure 2.6;
R	the responsivity in number of e^- / Joules;
n	the size of the lens PSF in number of pixels;
η	the total optical transmission.

All units are number of electrons collected in a pixel.

The camera is baffled to reject stray light coming from the Sun, but also from the balloon, the ground, and from the edges of the Sun shields. This is most important for

day-time operation, where the intensity of these parasitic signals could be strong enough to saturate the sensor.

We require that the sensor does not saturate, and stars to be detected with some signal-to-noise ratio:

$$\text{saturation} > \quad S_{\text{tot}} \simeq S_{\text{sky}} \quad \sim (\Phi/f)^2 \, T_{\text{int}} \tag{2.14}$$

$$5 < \quad \frac{S_{\text{star}}}{\text{Noise}} \quad \sim \Phi \, f \, \sqrt{T_{\text{int}}}. \tag{2.15}$$

where f is the star camera lens focal length. These two relations show how to optimize the sensor. For instance, f, and therefore the pixel field of view (FOV), is a very effective way to control the SNR, *and* the saturation of the CCD. On the contrary, acting on the integration time, or the aperture size of lens, would increase the sky signal linearly, and the SNR with the square root.

Figure 2.7 shows the number of stars that are, on average, available for a given star tracker FOV. This depends from the chosen pixel FOV, and the number of pixels the sensor has.

Figure 2.8 plots the signals that stars of different magnitude have on the sensor, together with the sky signal, as a function of the pixel FOV. The signal-to-noise ratio is shown there as well.

Finally, Figure 2.9 shows the effects of choosing different cut-offs for the high-pass optical filter used to attenuate the bright background at short wavelengths.

To build the star tracker we have the following requirements:

1: at least 3 stars have to be available, on average, in each camera frame;

2: exposure times should not exceed 100 ms, or the images would suffer by striping

due to the scan angular rate of the telescope (about $0.1°s^{-1}$);

3: the sky signal does not saturate the sensor;

4: the final pointing solution has to be better than $5''$ RMS, to oversample the $30''$ beam.

We have chosen a pixel FOV of $7''$. This set f to 200 mm given the pixel sizes of both the Kodak and the Sony sensors.

The lens aperture has been chosen to be the widest we could find, $\Phi = 100$ mm, to minimize exposure times.

With this lens, and 100 ms integrations, we can detect $m_v = 9$ stars at 5σ, using a red filter passing wavelengths longward of 600 nm.

With this filter and this overall configuration, the sky signal is at 2/3 of the full scale, allowing some safe margin of operation.

In-Flight Performance

Both star trackers performed well, being able to detect $m_v = 9$ stars with 100 ms integration times. The deeper well depth of the Kodak sensor allowed us to see stars even on those rare occasions when the scanned sky region, with low star surface density, required longer integration times, saturating the Sony sensor.

Each star camera frame taken is dominated by the background signal expressed by Equation 2.9. In Figure 2.10, this equation is plotted along with the in-flight measured values of the background, acquired during the Antarctic campaign. In this example, the telescope moved in elevation up and down a few times, then started an azimuth scan.

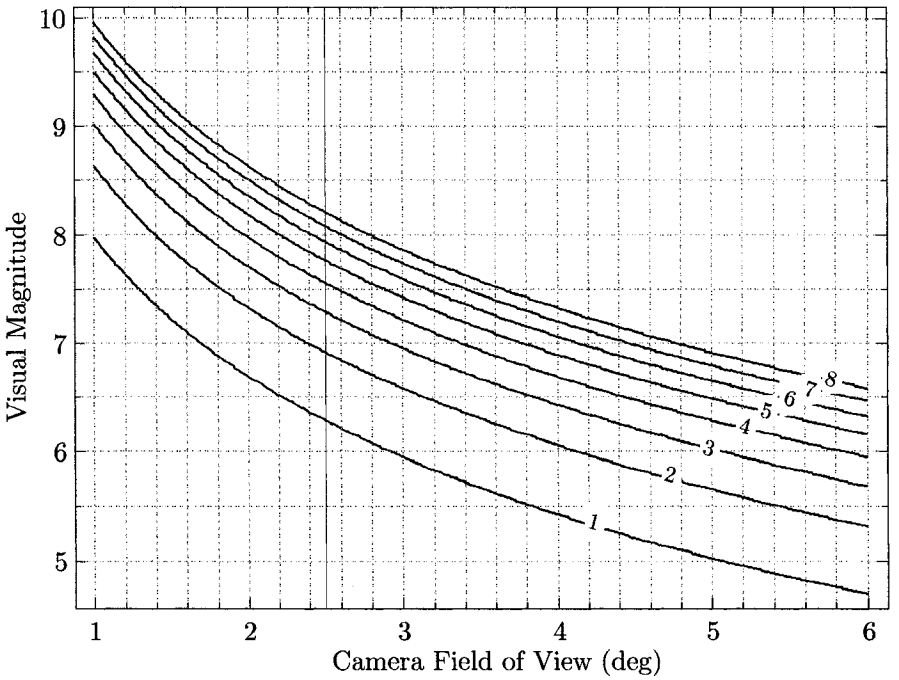

Figure 2.7: Visual magnitude vs. the star tracker FOV that allows a number N of stars to be available at any time, in each camera frame. The curves shown here are calculated for $N = 1$ to 8, and are accurate only when the star tracker observes at low Galactic latitudes. For the BLAST extragalactic region, chosen for the low level of background signals, we make sure, by direct inspection of a star catalogue, that enough stars are available.

The pressure at float is calculated using

$$T = -131.21 + 0.00299\,h \quad (^{\circ}\mathrm{C}) \tag{2.16}$$

$$p = 0.025\left[\frac{T + 273.15}{216.66}\right]^{-11.388} \quad (\mathrm{atm}) \tag{2.17}$$

where T is the ambient temperature, h is the altitude in meters and p is the pressure. This formula is valid for the upper stratosphere ($h > 25\,\mathrm{km}$). See [24].

A conversion factor from the camera native a/d unit (ADU) to ke$^-$ is found. The noise is dominated by the sky signal, and it is Poisson distributed. The signal is proportional to the number of electrons collected in the pixel well, and the noise is proportional to its

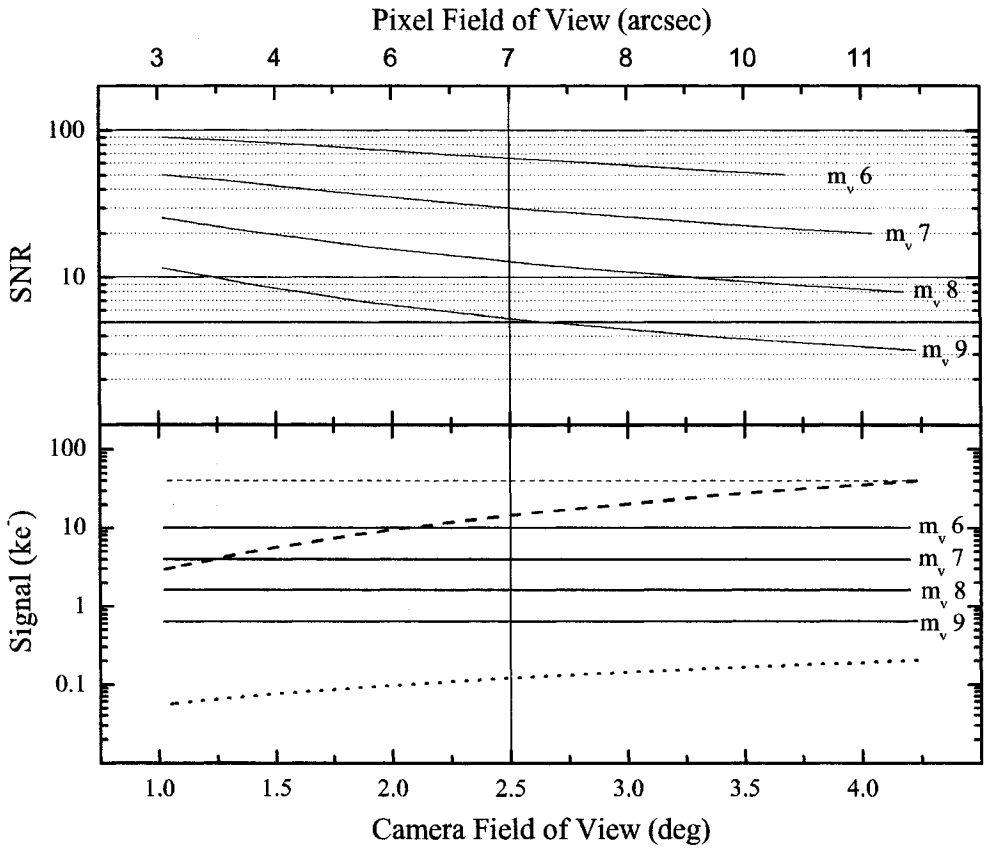

Figure 2.8: Day Time Star Tracker optimization. Top panel: the signal-to-noise ratio (SNR) of different magnitude stars as a function of the pixel and camera FOV. Bottom panel plots the sky signal (dashed line), the noise (dotted line) and the signal from the stars; the saturation level for the Kodak sensor is given as reference (thin dashed line). The computation is done assuming a lens with a diameter $\Phi = 100\,\text{mm}$, with 80% optical efficiency, and using a red filter at 600 nm. The sky radiance is from Figure 2.6. A magnitude 9 star can be detected at about 5 sigma, when the pixel FOV is $7''$. This translates to a total available 2.5° FOV for the sensor we used (see Table 2.2).

square-root. Let K be the constant of proportionality:

$$\text{Signal (ADU)} = K\,ne^{-}, \tag{2.18}$$

$$\text{Noise (ADU)} = K\sqrt{ne^{-}}. \tag{2.19}$$

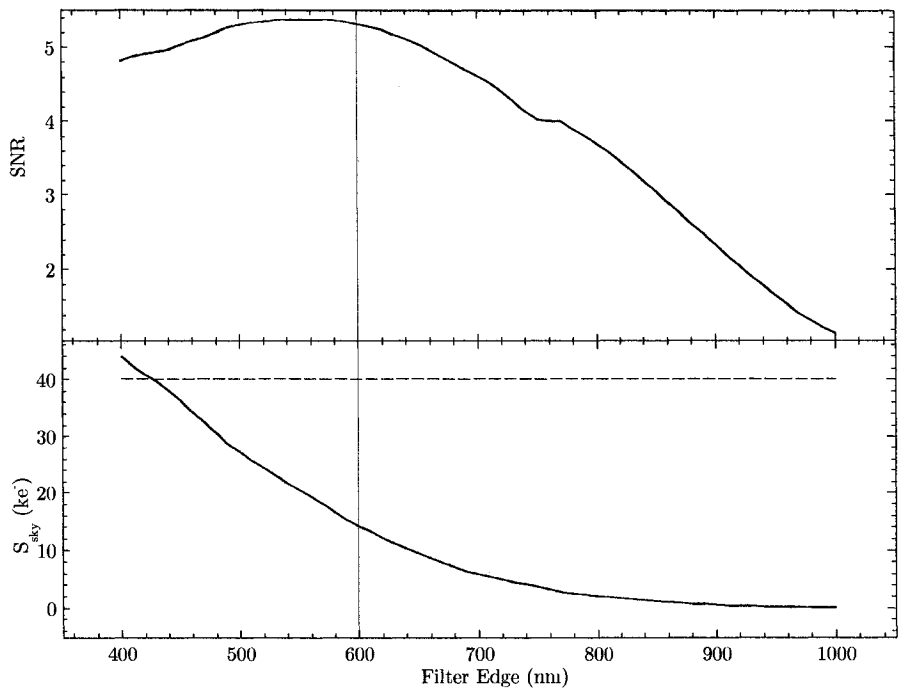

Figure 2.9: Effect of adding a red filter to the CCD. The top panel plots the SNR curve, for a magnitude 9 star as a function of the filter cut-off. The calculation is done assuming the same observation geometry used to generate Figure 2.8. The bottom panel shows the sky signal as a function of the cut-off, and the sensor saturation as a reference. In this case, a pixel FOV of 7″ is assumed. We have chosen to filter at 600 nm, slightly longward of the peak of the SNR curve, placing our working point about 2/3 away from saturation.

Therefore, measuring both the signal and its RMS at different illuminations, we solve for K in a least-square sense.

The average level of the sky signal is between 80 ke^-s^{-1}, and 100 ke^-s^{-1} at an altitude of 38 km. It is well fit by the model assuming a pressure of 0.003 atm (3 mbar), calculated from Equation 2.17.

In Figure 2.11, the histograms of the total number of stars detected in each frame are shown for the two cameras. The telescope was in this case scanning over a region chosen to be low in forground signal. Two to four stars were observed on average. While the FOV of each CCD pixel is 7″ on sky, the final absolute pointing accuracy is better than 2″ (see Figure 2.12). This is possible for two reasons: i) more than one star is usually

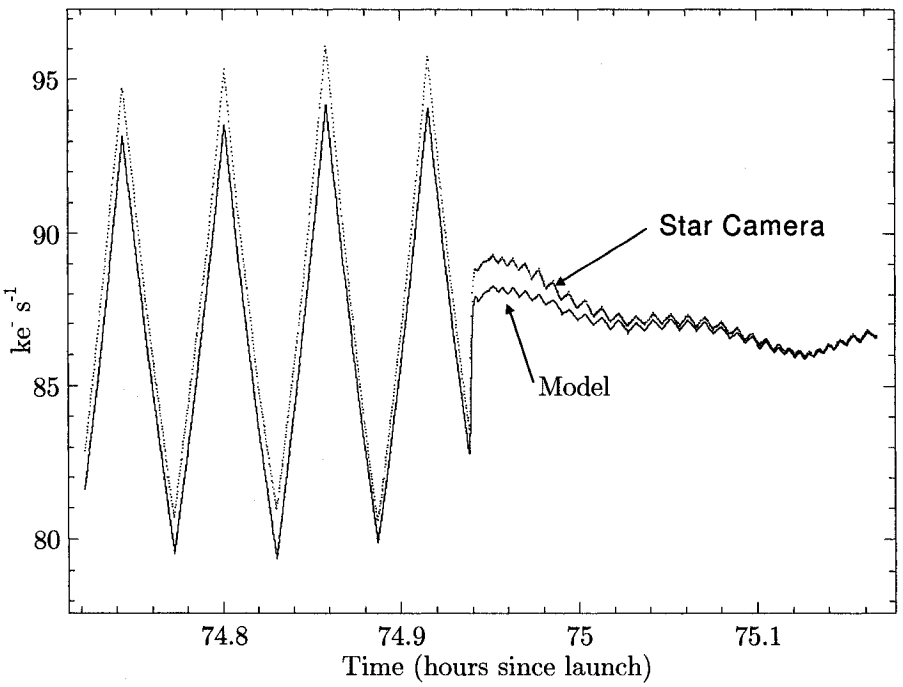

Figure 2.10: Background sky signal at float altitude (38 km, acquired during the Antarctic campaign) where the air-pressure is about 0.5% of that at sea level. The black curve shows the original mean signal in a CCD frame as a function of time, once an arbitrary DC term has been added. The red curve, shows the same signal Calculated from Equation 2.9.

available in each frame, and ii) the Airy disk of the Point Spread Function (PSF) is, for the lens used, about 5″. Therefore the star's image is spread over 3 or 4 CCD pixels, better constraining its position within the frame.

The accuracy achieved with the final pointing solution is discussed in Section 3.5.

Conclusions

We have designed, built and operated a day-time star-tracker for stratospheric balloon platforms. The sensor operated as designed during the two science flights.

I have presented most of the details that we have considered while building and operating this sensor, with the hope they may be used as a reference by those experimenters who will need such a sensor.

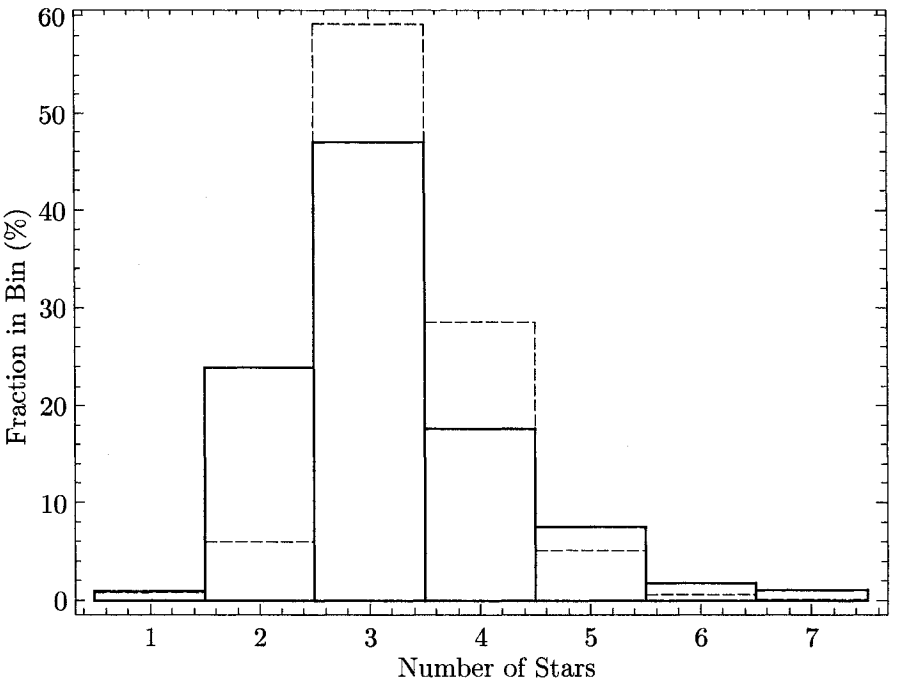

Figure 2.11: Histogram of the number of stars the two cameras detected scanning one extragalactic region during the Antarctic flight. The solid line refers to the Kodak-based camera, the dashed line to the Sony.

Copies of this star-tracker are being implemented by a number of other balloon borne, and ground based experiments, including SPIDER [25], EBEX [26], InFOCμs [27], OLIMPO and ACT.

2.2.2 Star Camera Algorithms

The star tracker needs to operate autonomously. It has to:

- acquire a picture of the sky;
- identify candidate stars in each frame as blobs emerging from the background noise;
- estimate the position of the blobs;
- match the candidate stars to a catalogue;

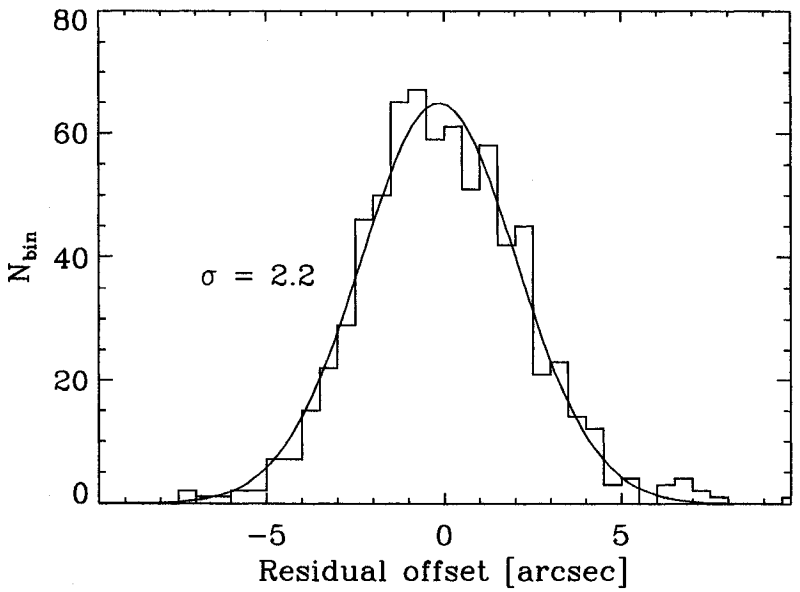

Figure 2.12: The angular offset between the two star cameras was measured from 721 pointing solutions from simultaneous images over 28 minutes while the telescope was stationary on the ground. The mean offset was removed, and the residual offset is shown here as a histogram. The standard deviation of the Gaussian fit to the histogram is $2.2''$. Assuming the errors in the two star camera pointing solutions are independent, the absolute uncertainty in an individual pointing solution inferred for one star camera is $2.2''/\sqrt{2} = 1.6$ RMS.

- estimate the bore-sight direction.

Blobs of candidate stars are selected as isolated signals emerging more than 5σ from the background noise. A least-squares fit of a paraboloid to the peak signal provides an estimate of the blob position within the frame. These positions are then matched to a star catalogue (Guide Star Catalogue 1.1, [28]).

After a positive identification is obtained, and spurious glares rejected, a least-square algorithm is used to calculate the bore-sight of the camera RA and Dec, $[\alpha, \delta]$.

Let $[\alpha_i, \delta_i]$ be the celestial coordinates of the i^{th} star, $[x_i, y_i]$ its coordinate in the frame (tangent plane coordinates), and let the camera bore-sight have celestial coordinates

$[\alpha_o, \delta_o]$ and be placed at the center of the frame, i.e. at coordinates $(0, 0)$. Celestial angular distances between the ith star and the bore-sight are:

$$cos(d_i) = \sqrt{x_i^2 + y_i^2 + 1}, \tag{2.20}$$

$$cos(D_i) = \cos(\alpha_i - \alpha_o)\cos\delta_i \cos\delta_o + \sin\delta_i \sin\delta_o. \tag{2.21}$$

$[\alpha_o, \delta_o]$ can be evaluated by minimizing the expression:

$$\chi^2 = \sum_i (d_i - D_i) \tag{2.22}$$

A similar algorithm can be subsequently used to estimate the rotation angle between the celestial meridian and the star camera.

Pyramid: Algorithm for Robust Star Pattern Recognition

A star pattern recognition algorithm was implemented as follows. A list of blob positions, composed of real stars as well as spurious glares, is morphologically compared to a catalog to identify the real astronomical sources in the list. The star tracker can detect stars down to a visual magnitude 9, which makes the catalog quite large. There are about 121,000 stars down to magnitude 9. The possible morphological combination to explore for a list of, say, 4 stars are about a billion. A blind search in the catalogue would take much longer than a hour on a reasonably fast computer.

One way to approach the problem is to reduce the size of the catalogue, having some rough information of where the telescope is pointing. A more appealing system is based on the Pyramid [29, 30] technique, currently used on several space missions.

Pyramid solves the Lost in Space problem: identify the stars detected in each CCD frame, without any *a priori* knowledge of the position, in a reasonable amount of time (usually

less than a second). We have implemented Pyramid from the basic algorithm [30]. The main idea is:

- Pyramid matches groups of 4 stars, detected in the same CCD frame, against a pre-built catalogue of star-pairs angular distances. This catalogue, called "k-catalogue" [31], is at the heart of the algorithm. The goal is to find 4 stars that have the same star-to-star angular distances as the one detected by the star-tracker. This group of 4 stars is called the "pyramid".

- The algorithm uses a "search-less" algorithm to look-up star pairs in the k-catalogue, making Pyramid extremely fast.

- Once a pyramid is identified, it is used to match all the other stars detected in the CCD frame. This approach is highly successful at rejecting glares.

- A number of exceptions are implemented to deal with cases where only three candidate stars are available in the blob list.

- Frames containing one or two stars are rejected, unless other information is available.

A pyramid is built bottom-up: at first, 3 star blobs are considered, and their relative angular distances are calculated. Three lists of star-pairs having the same angular distances (within some tolerance set assuming measurement errors) are extracted from the k-catalogue. Star-triangles are searched within these lists looking for three star-pairs (one from each list) forming a triangle.

Finally a 4^{th} blob is used to build the pyramid. Usually, only one of the matched triangles builds the pyramid, hence concluding the algorithm. If a match is not achieved, the recursion continues until all possible combination of 3-blobs are explored.

Pyramid was developed for wide field-of-view ($> 10^o$) star trackers, sensitive down to magnitude 6 stars. A k-catalogue with a similar depth is relatively small compared to the one required for BLAST, sensitive down to magnitude 9.

We had to implement one modification to the original method. While the search-less k-catalogue algorithm is extremely effective at extracting stars-pairs from the catalogue, the depth of the catalogue itself makes the number of pairs too large to be explored in a reasonable amount of time (less than a second).

Therefore we have implemented a binary search [4] to speed up this portion of the algorithm to a few tens of milliseconds. Star pairs are ordered with respect to their ID-index in the star catalogue. While the first list of star-pairs is explored one-by-one, a binary search is conducted in the second of the three lists, looking for star-pairs having one star in common with the first list (this is done checking the star ID). Once the match is achieved, a search for a star-pair having the same two stars is repeated in the third list.

Pyramid is very reliable, as discussed in [30], and we have not found any false-positives during normal operation.

The software is currently in a very mature stage and is available under the GNU public licence upon request.

2.2.3 Fiber Optic Gyroscope

Gyroscopes measure the rotation rate around one axis. BLAST has two sets of gyros. Each set is equipped with three sensors mounted so that the angular velocity components along three independent axes can be measured at any given time. One set mounts three

[4] We use a modified version of the "bsearch" algorithm implemented in the GNU libc. In case of multiple records matching the search criteria, the original bsearch algorithm returns one of the matches; our implementation always return the first record in the ordered list. We use "qsort" (implemented in the same library) to sort the input lists.

KVH E-core 2000 and the other mounts three KVH DSP 3000 interferometric fiber optics gyros (I-FOG) in two different temperature controlled boxes. Constant temperature is required in order to have a constant zero velocity bias. In fact, experience has shown that the zero velocity set point of these sensors depends on temperature gradients.
The operation of an I-FOG [32] is based on the Sagnac effect [33]. It measures the phase shift between the co-rotating and the counter-rotating beams through a fiber (see Figure 2.13). When light propagates on a rotating fiber coil, the transit time is proportional to the rotation rate. This results in a phase difference between beams propagating on the loop in opposite directions. The phase difference, ϕ_r, detected by an interferometer

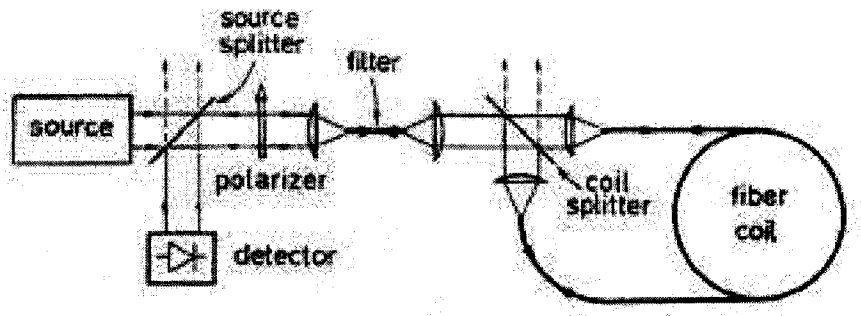

Figure 2.13: Minimum configuration of an Interferometric Fiber Optic Gyroscope. A laser beam is split in two and each portion is injected at both extremities of a fiber optic coil. The phase shift between the two emerging beams is a function of the angular velocity at which the coil rotates and is detected with an interferometer (from [34]).

is a measure of the rotation rate $\mathbf{\Omega}$: $\phi_r = 4\omega/c^2\mathbf{A}\cdot\mathbf{\Omega}$ (here $\mathbf{A}$ is the area vector enclosed by the optical path and ω is the angular frequency of the light source). Performance of these sensors is listed in Table 2.3[5].

In the early 1980s it was recognized that a phase shifts may also occur as a result of magnetic fields [36] through Faraday rotation [37]. When the gondola rotates, the Earth's magnetic field induces a bias variation that results in a modulation of the angular rate measured by the gyros, and it is comparable to the Earth's rotation angular velocity. In

[5]The Allen variance [35] is used to estimate the angle random walk.

	Ecore 2000	DSP 3000
Maximum Rotation Rate (deg/sec)	±30	±375
Angle Random Walk (asec/$\sqrt{sec}$)	4.8	4.0
Bandwidth (Hz)	100	500

Table 2.3: BLAST I-FOG parameters. The angular random walk is the relevant parameter that will be used in the pointing solution. It sets the temporal length on which the gyros can be integrated, before the random error grows too much. For BLAST, this is about 1.5 – 2 seconds.

order to minimize this spurious signal, gyros are mounted in boxes wrapped with high μ material foil, as suggested in [36]. This results in a –10 db reduction of the sensitivity to magnetic fields.

The output of each gyro is proportional to the component of the angular velocity parallel to its axis, so each gyro box measure,

$$\mathbf{\Omega} = \omega + \mathbf{b}, \tag{2.23}$$

where $\mathbf{\Omega}$ is the true angular velocity, and ω is the gyro output. A slow-varying bias, $\mathbf{b}$, has a brown spectrum. Therefore, $\mathbf{b}$ can be modeled as driven by a Gaussian white noise (called in the next chapter Process Noise):

$$\dot{\mathbf{b}} = \mathbf{n_b}, \tag{2.24}$$

with some variance σ_b^2.

In the presence of noise, Equation 2.23 becomes:

$$\tilde{\mathbf{\Omega}} = \omega + \mathbf{b} + \mathbf{w}_\omega \tag{2.25}$$

where $\mathbf{w}_\omega$ is Gaussian white noise with some variance σ_ω^2.

Orthogonalization

In each of the two boxes, three gyros are mounted to measure the components of the angular velocity vector along three independent directions. We require these directions to be mutually orthogonal. Therefore an orthogonalization process must be performed. This requires moving the gondola around three perpendicular axes. First, we rotate the inner frame around its elevation axis several times. Then we point frame at zero and 90 degrees, and rotate the gondola around its azimuth. Let $\hat{x}$, $\hat{y}$ and $\hat{z}$ be the direction vectors in the orthogonal reference frame, and $\hat{1}$, $\hat{2}$ and $\hat{3}$ be the direction vector of each gyro in a box. We also assume that $\hat{x}$, $\hat{y}$ and $\hat{z}$ define the pitch, roll and azimuth axes. Then,

$$\omega_x\hat{x} + \omega_y\hat{y} + \omega_z\hat{z} = g_1\hat{1} + g_2\hat{2} + g_3\hat{3}, \tag{2.26}$$

with g_1, g_2, and g_3 the quantities measured by the three gyros and ω_x, ω_y, and ω_z the angular velocity components in the orthogonal frame. From this we write

$$\begin{pmatrix} \omega_x \\ \omega_y \\ \omega_z \end{pmatrix} = \begin{pmatrix} \hat{1}\cdot\hat{x} & 0 & 0 \\ 0 & \hat{3}\cdot\hat{y} & 0 \\ 0 & 0 & \hat{2}\cdot\hat{z} \end{pmatrix} \begin{pmatrix} 1 & \frac{\hat{3}\cdot\hat{x}}{\hat{1}\cdot\hat{x}} & \frac{\hat{2}\cdot\hat{x}}{\hat{1}\cdot\hat{x}} \\ \frac{\hat{1}\cdot\hat{y}}{\hat{3}\cdot\hat{y}} & 1 & \frac{\hat{2}\cdot\hat{y}}{\hat{3}\cdot\hat{y}} \\ \frac{\hat{1}\cdot\hat{z}}{\hat{2}\cdot\hat{z}} & \frac{\hat{3}\cdot\hat{z}}{\hat{2}\cdot\hat{z}} & 1 \end{pmatrix} \begin{pmatrix} g_1 \\ g_2 \\ g_3 \end{pmatrix}. \tag{2.27}$$

Once the gondola is steady and only the inner frame is rotated, the angular velocity is $\omega = (\omega_x, 0, 0)$. The gyros detect:

$$g_1 = \omega_x\hat{1}\cdot\hat{x}, \tag{2.28}$$

$$g_2 = \omega_x\hat{2}\cdot\hat{x}, \tag{2.29}$$

$$g_3 = \omega_x\hat{3}\cdot\hat{x}. \tag{2.30}$$

From this we can build the two quantities

$$g_2 = g_1 \frac{\hat{2} \cdot \hat{x}}{\hat{1} \cdot \hat{x}}, \tag{2.31}$$

$$g_3 = g_1 \frac{\hat{3} \cdot \hat{x}}{\hat{1} \cdot \hat{x}}. \tag{2.32}$$

Plotting g_2 and g_3 vs g_1, a linear least-square method allows us to measure the angular coefficients that are elements in the orthogonalization matrix in Equation 2.27. Doing the same for the other two gondola rotations, we completely measure the orthogonalization matrix. The other matrix in Equation 2.27 is just a gain matrix. This can be measured by rotating the telescope by some known angular amount.

An analysis of the errors in the orthogonalization parameters has not been carried out, but the values measured where within the accuracies required to obtain a satisfactory pointing reconstruction from the Kiruna flight, as shown in Section 3.5

2.2.4 Coarse Sensors

A number of less accurate pointing sensors are used to guide the gondola toward a selected target (a region of the sky that we want to observe). Once the telescope is close enough to this target, the star cameras enter in their operative range, and the coarse sensors are automatically overridden by the inertial solution in which they are assigned a smaller weight relative to the star trackers.

Attitude GPS

A Differential Global Position System (DGPS) is used to provide geographic coordinates, time, and the three Euler angles that fully describe the gondola attitude (see Section 3.2). Four different antennas are required for the DGPS operation. They were rigidly mounted

on the outer frame at the very top of the gondola so that each antenna has an unobstructed view of the sky.

The accuracy of the DGPS strongly depends on the position of the antennas. The wider apart they are, one from the other, the higher is the accuracy. This, at least, up to a maximum distance defined by the manufacturer. BLAST mounted the antennas 2 m apart to achieve accuracies of about 10′ RMS.

Unfortunately, the DGPS was also found to be unreliable. During the Kiruna flight it did not work. In the Antarctic flight, it worked for the second part of the flight, only.

We believe that this erratic behavior was due to the relative position of the antennas, which has to be known to one cm. The antennas are surveyed before flight, but when the gondola is hung from the launch vehicle, this position can change slightly, due to structural bending.

It is impossible to survey the positions before flight, since the satellite signal is obstructed by the launch vehicle.

While it is possible to re-calibrate the DGPS antennas in flight, we have never tried this procedure.

We have concluded that the DGPS is not a reliable sensor, and its use on future balloon flights will have to be re-considered.

Encoder

A 16 bit absolute encoder is used on the inner frame axis to measure the relative rotation of the inner frame with respect to the outer frame. 20″ precision was achieved. The encoder was used in-flight, to controll the position of the inner frame.

Sun Sensor

The BLAST Sun sensor was mounted on the outer frame, on the back side of the gondola. It consists of two 2048-pixel linear CCDs oriented at 90 degrees with respect to each other. Each linear camera has an orthogonal slit in front of it. In this configuration, one camera is sensitive to azimuthal rotations while the other is to pitch. This sensor provides azimuth and pitch of the gondola outer frame with respect to the Sun. A calibrated look-up table is acquired before flight. The Sun position is calculated at any given time to transform the Sun sensor output into azimuth and elevation.

Once the Sun shines onto the cameras through the slits, the flight code samples the pixels and returns a weighted average of the pixel position by its intensity.

This sensor had a short-time relative precision of 2', but an overall absolute accuracy of 5°.

Magnetometer

A flux gate magnetometer is also used. It measures the flux of the Earth's magnetic vector through two orthogonal coils. The coils are mounted so that only the component of the magnetic vector that is parallel to the horizon is measured. The sensor is intrinsically very precise once characterized through a look-up table (few arc-seconds RMS). Magnetic field direction changes with the geographical location, and the model that quantifies this variation (the World Magnetic Model [6]) has an accuracy of 10%. Bias drifts, and coupling of pitch and roll into azimuth (in particular at the poles where the magnetic vector has a high inclination) complicate its use. An overall accuracy of 5 deg. peak to peak was achieved.

[6] http://www.ngdc.noaa.gov/seg/WMM/DoDWMM.shtml

Chapter 3

Attitude Determination

3.1 Pointing Reconstruction Requirements

The problem of estimating the beam's position in sky, at each bolometric sample, is the problem of estimating the rotation (attitude) of the payload with respect to the celestial sphere.

Knowing the direction were a detector is pointing as a function of time enables the reduction of the array time streams into maps, as will be discussed in Chapter5.

Blast beams are well described by gaussians of 30", 42", and 60" FWHM at 250 μm, 350 μm, and 500 μm, respectively:

$$B(\theta) = e^{-\frac{\theta^2}{2\sigma_b^2}}, \tag{3.1}$$

where the beam FWHM is $\sigma_b\sqrt{8\log 2}$.

Assuming the reconstructed attitude has an angular error described by a random white noise process of variance σ_p^2, the effect of the pointing errors is to widen the telescope

beam as

$$B(\theta) = e^{-\frac{\theta^2}{2(\sigma_b^2+\sigma_p^2)}}. \tag{3.2}$$

A large error σ_p will i) reduce the telescope resolution, and ii) reduce the sensitivity to point sources.

Requiring that point source sensitivity would not be reduced by more than 1%, gives

$$\sigma_p^2 < 0.01\ \sigma_b^2. \tag{3.3}$$

For the 250 μm beam this is about 1.5" RMS.

3.2 Euler Angles and the Attitude Matrix

Positions on the celestial sphere may be specified by using a spherical polar coordinate system, defined in terms of some fundamental plane and a line in that plane chosen to represent zero longitude. Mathematicians usually work with the co-latitude, with zero at the principal pole, whereas most astronomical coordinate systems use latitude, reckoned plus and minus from the equator. Astronomical coordinate systems may be either right-handed (*e.g.* right ascension and declination $[\alpha, \delta]$, Galactic longitude and latitude $[l^{II}, b^{II}]$), or left-handed (*e.g.* hour angle and declination $[h, \delta]$). Azimuth and geographical longitude are examples of alternate conventions that have been used in the past; azimuth is now generally reckoned north through east (making a left-handed system); geographical longitude is now usually taken to increase eastwards (a right-handed system) but astronomers used to employ a west-positive convention. In reports and program comments it is wise to spell out what convention is being used, if there is any possibility of confusion.

The $[\alpha, \delta]$ coordinate system is the one generally used to present scientific results, and

is the one we will adopt throughout this work. Even if the payload is best represented in $[Az, El]$, these coordinates depend on time and are not inertial, introducing extra parameters into the problem (i.e. one has to take in to account that the Earth rotates on its axis when interpreting the gyroscopes).

The payload is a rigid body and three Euler angles are required in order to measure its rotation relative to the stars. We set a reference frame (Figure 3.1) $[X_G, Y_G, Z_G]$ on the gondola and assign a similar reference frame to the celestial sphere, $[X_I, Y_I, Z_I]$. The rotation between the two frames is fully described by three Euler angles that can be chosen with some freedom. The three angles we choose are yaw, pitch and roll, representing a rotation around Z_G, X_G and Y_G respectively ($[\alpha, \delta, \rho]$ where the orientation is set by the right hand rule). The order of the rotations has to be respected since they do not commute. Using this convention, yaw and pitch coincide with right ascension and declination.

The attitude of the telescope is represented through a rotation matrix or attitude matrix, $\mathcal{A}$. If $\mathbf{b}_G$ and $\mathbf{b}_I$ are the directions of the telescope bore-sight in sky, in the gondola and inertial frame, respectively, they are related by

$$\mathbf{b}_I = \mathcal{A}\, \mathbf{b}_G. \tag{3.4}$$

Going from the inertial to the gondola frame, we need to first rotate yaw, then pitch, and then roll. Going in the opposite direction the order of the rotations is inverted. Therefore

$$\mathcal{A} = \mathcal{A}_{yaw}(\alpha)\, \mathcal{A}_{pitch}(\delta)\, \mathcal{A}_{roll}(\rho), \tag{3.5}$$

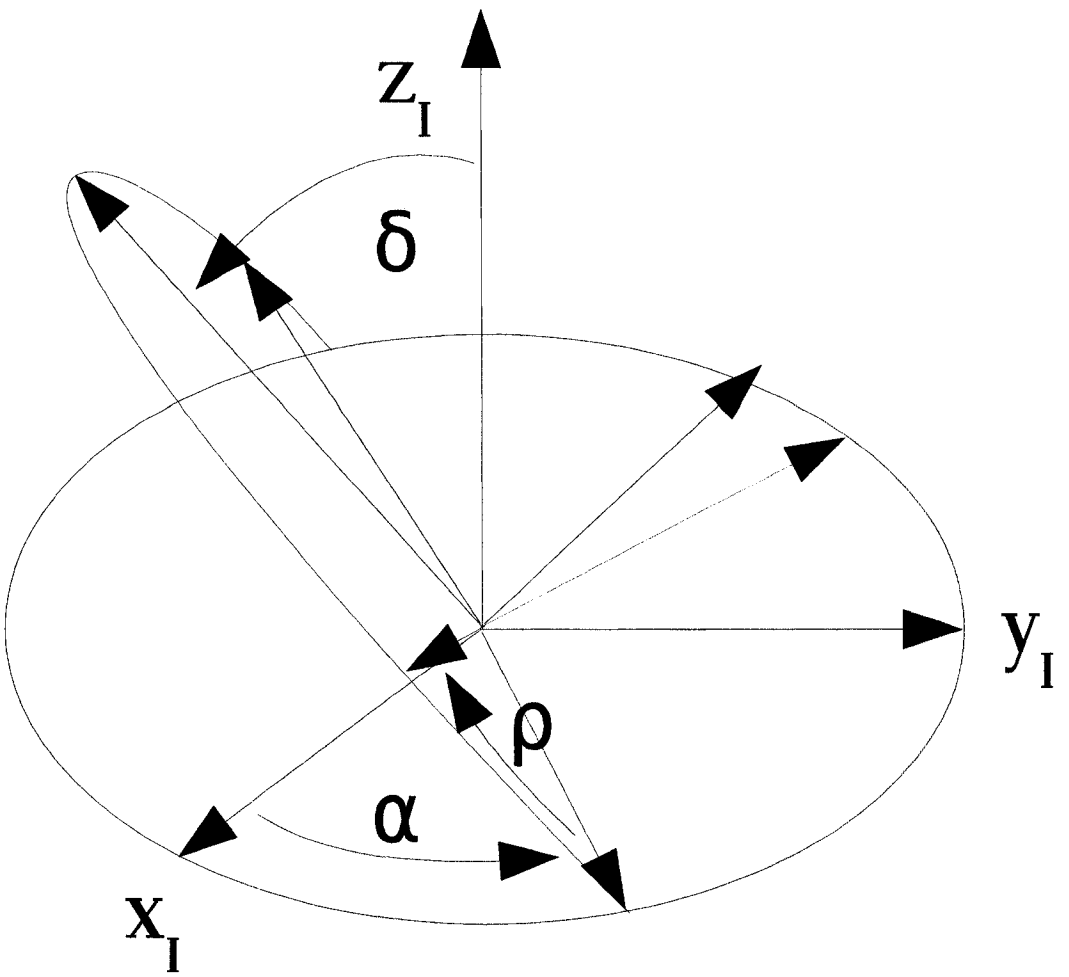

Figure 3.1: The three Euler angles chosen to represent the rotation of the gondola relative to a inertial system. The rotation are executed in order: first around Z by an angle α, then around X by an angle δ, and finally around Y by ρ. α and δ are the right ascension and declination.

$$\mathcal{A}_{yaw}(\alpha) = \begin{pmatrix} \cos(\alpha) & -\sin(\alpha) & 0 \\ \sin(\alpha) & \cos(\alpha) & 0 \\ 0 & 0 & 1 \end{pmatrix}, \quad \mathcal{A}_{pitch}(\delta) = \begin{pmatrix} 1 & 0 & 0 \\ 0 & \cos(\delta) & -\sin(\delta) \\ 0 & \sin(\delta) & \cos(\delta) \end{pmatrix},$$

$$\mathcal{A}_{roll}(\rho) = \begin{pmatrix} \cos(\rho) & 0 & \sin(\rho) \\ 0 & 1 & 0 \\ -\sin(\rho) & 0 & \cos(\rho). \end{pmatrix}$$

For the discussion that follows (see Figure 3.1):

i) $\mathbf{b}_G // Y_G$;

ii) yaw is the Ra of the $\mathbf{b}_G$ vector in the inertial coordinate frame;

iii) pitch is the Dec of the $\mathbf{b}_G$ vector in the inertial coordinate frame;

iv) roll is the rotation of the gondola coordinate frame around the direction $\mathbf{b}_G$.

3.3 Quaternions

While rotations can be represented through an attitude matrix, there are other formal methods to apply these transformations. It is known that a rotation in the complex plane can be represented with a multiplication by the complex number $e^{i\phi}$. Similarly, rotations in a 3D space can be represented with *quaternions*, first invented by William Rowan Hamilton [38] [1]. A quaternion q is defined as a set of 4 real numbers $q = (q_0, q_1, q_2, q_3)$. q_0 is said to be its real part while q_1, q_2, q_3 are the imaginary parts. A quaternion can also be represented with a real number and a vector $q = (s, \mathbf{v})$.

The following definitions apply:

[1] The idea for quaternions occurred to him while he was walking with his wife along the Royal Canal on his way to a meeting of the Irish Academy in Dublin, and Hamilton was so pleased with his discovery that he scratched the fundamental formula of quaternion algebra ($i^2 + j^2 + k^2 = ijk = -1$) into the stone of the Brougham bridge [39].

Unit:	$I = (1, \mathbf{0})$
Norm:	$\|\|(s, \mathbf{v})\|\| = s^2 + \mathbf{v} \cdot \mathbf{v}$
Conjugate:	$(s, \mathbf{v})^* = (s, -\mathbf{v})$
Inverse:	$q^{-1} = q^*/\|\|q\|\|$
Addition:	$(s1, \mathbf{v1}) + (s2, \mathbf{v2}) = (s1 + s2, \mathbf{v1} + \mathbf{v2})$
Subtraction:	$(s1, \mathbf{v1}) - (s2, \mathbf{v2}) = (s1 + s2, \mathbf{v1} - \mathbf{v2})$
Multiplication:	$(s1, \mathbf{v1})\ (s2, \mathbf{v2}) = (s1s2 - \mathbf{v1} \cdot \mathbf{v2},\ s1\,\mathbf{v2} + s2\ \mathbf{v1} + \mathbf{v1} \times \mathbf{v2})$
Division:	$q_1/q_2 = q_1\, q_2^{-1}$

Additions and subtractions are both associative and commutative. Multiplication is associative, but not commutative. A quaternion q is a unit quaternion if $\|\|q\|\| = qq^* = q^*q = I$. A unit quaternion can always be expressed as $(\cos(\psi), \hat{\mathbf{u}}sin(\psi))$ where $\hat{\mathbf{u}}$ is a unit vector, and ψ is a real number.

For a given vector $\mathbf{v}$ in $\Re^3$, it is natural to build the quaternion $(0, \mathbf{v})$. The connection between rotations and quaternions is as follow: let $q = (cos(\frac{1}{2}\psi), \hat{\mathbf{u}}\ sin(\frac{1}{2}\psi)$ is a unit quaternion and $\mathbf{v}_1$ a vector. Then the vector $\mathbf{v}_2$ defined by

$$\begin{pmatrix} 0 \\ \mathbf{v}_2 \end{pmatrix} = q \begin{pmatrix} 0 \\ \mathbf{v}_1 \end{pmatrix} q^*, \tag{3.6}$$

is the vector $\mathbf{v}_1$ rotated by an angle ψ about the axis $\hat{\mathbf{u}}$.

Given the operations defined for the quaternions, it is easy to show that

$$\mathcal{A}_{yaw}(\alpha) \Rightarrow q_{yaw}(\alpha) = \begin{pmatrix} \cos\left(\frac{1}{2}\alpha\right) \\ \hat{\mathbf{z}}\ \sin\left(\frac{1}{2}\alpha\right) \end{pmatrix}, \tag{3.7}$$

$$\mathcal{A}_{pitch}(\delta) \Rightarrow q_{pitch}(\delta) = \begin{pmatrix} \cos\left(\frac{1}{2}\delta\right) \\ \hat{\mathbf{x}}\ \sin\left(\frac{1}{2}\delta\right) \end{pmatrix}, \tag{3.8}$$

$$\mathcal{A}_{roll}(\rho) \Rightarrow q_{roll}(\rho) = \begin{pmatrix} \cos\left(\frac{1}{2}\rho\right) \\ \hat{\mathbf{y}} \sin\left(\frac{1}{2}\rho\right) \end{pmatrix}, \tag{3.9}$$

$$\tag{3.10}$$

and

$$\begin{pmatrix} 0 \\ \mathbf{b}_I \end{pmatrix} = q^*_{yaw}(\alpha) q^*_{pitch}(\delta) q^*_{roll}(\rho) \begin{pmatrix} 0 \\ \mathbf{b}_G \end{pmatrix} q_{roll}(\rho) q_{pitch}(\delta) q_{yaw}(\alpha). \tag{3.11}$$

Using quaternions instead of matrices does not save computation time: a multiplication of quaternions uses the same number of operations as a multiplication of matrices, but quaternions have other more appealing advantages. Quaternions use fewer elements (4 vs 9) reducing the number of degenerate parameters, and they are easy to renormalize. Quaternions are also more intuitive (a rotation is defined by one angle and one axis of rotation, easily visible in this notation) helping to reduce the the possibility of making an error while formulating a problem or coding it into a computer.

Gyroscopes measure ω_{yaw}, ω_{pitch}, ω_{roll}, the angular velocities along the yaw, pitch and roll axis. Let q_o be the the attitude quaternion at time t_o. At time $t_1 = t_o + \Delta T$ the gondola has rotated by $\omega_{yaw}\Delta T$, $\omega_{pitch}\Delta T$ and $\omega_{roll}\Delta T$. Therefore the attitude quaternion at the time t_1 is

$$q_1 = \begin{pmatrix} \cos\left(\frac{1}{2}\omega_{yaw}(t_o)\Delta T\right) \\ \hat{\mathbf{z}} \sin\left(\frac{1}{2}\omega_{yaw}(t_o)\Delta T\right) \end{pmatrix} \begin{pmatrix} \cos\left(\frac{1}{2}\omega_{pitch}(t_o)\Delta T\right) \\ \hat{\mathbf{x}} \sin\left(\frac{1}{2}\omega_{pitch}(t_o)\Delta T\right) \end{pmatrix} \begin{pmatrix} \cos\left(\frac{1}{2}\omega_{roll}(t_o)\Delta T\right) \\ \hat{\mathbf{y}} \sin\left(\frac{1}{2}\omega_{roll}(t_o)\Delta T\right) \end{pmatrix} q_o. \tag{3.12}$$

To first order in ΔT, this can be written as

$$q_1 = \begin{pmatrix} 1 \\ \frac{1}{2}\omega_0 \Delta T \end{pmatrix} q_o, \tag{3.13}$$

and at an arbitrary time t_n

$$q_n = \begin{pmatrix} 1 \\ \frac{1}{2}\omega_{n-1}\Delta T \end{pmatrix} q_{n-1}\, q_{n-2} \cdots q_o. \tag{3.14}$$

The differential relation between the rate of change of the quaternion and the coordinate angular velocity is then

$$\dot{q}(t) = \frac{1}{2} \begin{pmatrix} 0 \\ \omega(t) \end{pmatrix} q(t). \tag{3.15}$$

We will use quaternion notation to estimate the attitude of the telescope.

3.4 Kalman Filter

In this section we introduce the concept of a state model, and an optimal estimator of the telescope's attitude given both the causal available past (Kalman Filter) and the not causal future (Kalman Smoother). The Kalman Filter is a predictor-corrector method that uses all the available information to produce an estimate of the state quaternion in a Minimum Mean-Square Error (MMSE) sense.

3.4.1 State Model

A state model describes the behavior of a dynamical system. For example, the gondola is a dynamical system that can be described by its attitude quaternion and the rate at which this quantity changes with time.

A general time-invariant m-input p-output N-dimensional continuous-time system can

be represented by the state model,

$$\begin{cases} \dot{\mathbf{x}}(t) = A(\mathbf{x}(t), \mathbf{w}(t)), \\ \mathbf{s}(t) = C(\mathbf{x}(t)). \end{cases} \tag{3.16}$$

Here $\mathbf{x}(t)$ is the N-dimensional state vector, $\mathbf{s}(t)$ is the p-dimensional output vector, and $\mathbf{w}(t)$ is the m-dimensional input vector. A and C are functions that describe the dynamics of the system. One more Equation relates the state vector with the measurement $\mathbf{z}(t)$:

$$\mathbf{z}(t) = \mathbf{s}(t) + \mathbf{n}(t) \tag{3.17}$$

where $\mathbf{n}(t)$ is the *measurement noise* on the p-dimensional measurement vector. To clarify what this means, one can think of the components of $\mathbf{x}(t)$ to be the components of the attitude quaternion. $\mathbf{w}(t)$ are external perturbations to the gondola, like the driving effects of the motors or the more stochastic perturbations induced by winds on the structure. For these reason, $\mathbf{w}(t)$ is often called *process noise.* The expression $C(\mathbf{x}(t))$ relates the state vector to the measurements provided by the attitude sensors.

The problem as formulated can be highly non-linear, but a linear first order approximation can be made in most cases. Therefore Equation 3.16 can be expressed as:

$$\begin{cases} \dot{\mathbf{x}}(t) = A\mathbf{x}(t) + B\mathbf{w}(t) \\ \mathbf{s}(t) = C\mathbf{x}(t) \end{cases} \tag{3.18}$$

where A, B, and C are linear operators from the first order expansion of Equation 3.16. The complete solution, with initial state $\mathbf{x}(t_o)$ at the initial time t_o, is

$$\mathbf{x}(t) = e^{A(t-t_o)}x(t_o) + \int_{t_o}^{t} e^{A(t-\tau)}B\mathbf{w}(\tau)\,d\tau, \quad t > t_o. \tag{3.19}$$

In order to implement the state model on a computer, we need to discretize it. To

accomplish this, let ΔT be the sampling interval and set $t_o = n\,\Delta T$ and $t = (n+1)\,\Delta T$ (n is the discrete time index). This yields

$$\mathbf{x}[(n+1)\,\Delta T] = e^{A\,\Delta T}\mathbf{x}(n\,\Delta T) + \left\{\int_{n\,\Delta T}^{(n+1)\,\Delta T} e^{A[\,(n+1)\,\Delta T - \tau]} B\,d\,\tau\right\}\mathbf{w}(n\,\Delta T) \tag{3.20}$$

where we assumed that $\mathbf{w}(\tau)$ is approximately constant over each time interval, and $\mathbf{w}(\tau) \simeq \mathbf{w}(n\Delta T)$, for $n\Delta T \leq \tau \leq (n+1)\Delta T$.

Letting

$$\Gamma = \int_{n\,\Delta T}^{(n+1)\,\Delta T} e^{A\,((n+1)\,\Delta T - \tau)} B\,d\,\tau, \tag{3.21}$$

and

$$\Phi = e^{A\,\Delta T}, \tag{3.22}$$

the time discrete state model can be written as

$$\mathbf{x}_{n+1} = \Phi\,\mathbf{x}_n + \Gamma\,\mathbf{w}_n \tag{3.23}$$

$$\mathbf{z}_n = C\,\mathbf{x}_n + \mathbf{n}_n \tag{3.24}$$

In this formulation

- Φ, Γ, and C are known deterministic matrices with respective dimensions $N \times N$, $N \times m$, and $p \times N$;

- $\mathbf{w}_n$ is stationary *process noise*, an m-vector zero-mean white-noise random process with $m \times m$ covariance matrix Q, i.e.,

$$E\left[\mathbf{w}_i \mathbf{w}_j^T\right] = Q\,\delta(i-j); \tag{3.25}$$

- $\mathbf{n}_n$ is stationary *measurement noise*, a p-vector zero-mean white noise random pro-

cess with $p \times p$ covariance matrix R, i.e.,

$$E\left[\mathbf{n}_i \mathbf{n}_j^T\right] = R\,\delta(i-j). \tag{3.26}$$

The *a priori* and *a posteriori* Estimates

The Kalman filter provides an estimate of the state vector described by the state model 3.24 through a prediction correction algorithm. Assume we have $n-1$ measurements $\{\mathbf{z}_{n-1} \ldots \mathbf{z}_0\}$; an *a priori* estimate of the state vector is built as

$$\hat{\mathbf{x}}_n^- = \text{the MMSE estimate of } \mathbf{x}_n \text{ given } \{\mathbf{z}_{n-1} \ldots \mathbf{z}_0\}.$$

When a new measurement z_n becomes available, a new *a posteriori* estimate of the state vector is evaluated as

$$\hat{\mathbf{x}}_n = \text{the MMSE estimate of } \mathbf{x}_n \text{ given } \{\mathbf{z}_n,\ \mathbf{z}_{n-1} \ldots \mathbf{z}_0\}.$$

Both of these estimates have an associated error. Denoting the estimation error by a tilde, these are

$$\tilde{\mathbf{x}}_n^- = \mathbf{x}_n - \hat{\mathbf{x}}_n^- = \text{the } a \textit{ priori} \text{ error}, \tag{3.27}$$

$$\tilde{\mathbf{x}}_n = \mathbf{x}_n - \hat{\mathbf{x}}_n = \text{the } a \textit{ posteriori} \text{ error}. \tag{3.28}$$

The associated covariance matrices are

$$P_n^- = \mathrm{Cov}[\tilde{\mathbf{x}}_n^-] = E\left[\tilde{\mathbf{x}}_n^- \tilde{\mathbf{x}}_n^{-T}\right], \tag{3.29}$$

and

$$P_n = \mathrm{Cov}[\tilde{\mathbf{x}}_n] = E\left[\tilde{\mathbf{x}}_n \tilde{\mathbf{x}}_n^T\right]. \tag{3.30}$$

Kalman Filter Algorithm

Finally, the Kalman recursive algorithm to evaluate the state vector is given by [40]:

- *Measurement update.* Acquire z_n and compute *a posteriori* quantities:

$$K_n = \frac{P_n^- C^T}{C P_n^- C^T + R}, \tag{3.31}$$

$$\hat{\mathbf{x}}_n = \hat{\mathbf{x}}_n^- + K_n \left[z_n - C \hat{\mathbf{x}}_n^- \right], \tag{3.32}$$

$$P_n = P_n^- - K_n C P_n^-. \tag{3.33}$$

- *Time update.* Compute *a priori* quantities for time $n+1$:

$$\hat{\mathbf{x}}_n^- = \Phi \hat{\mathbf{x}}_n, \tag{3.34}$$

$$P_n^- = \Phi P_n \Phi^T + \Gamma Q \Gamma^T. \tag{3.35}$$

- *Time increment.* Increment n and repeat.

The *a priori* update propagates the state vector in the absence of a new measurement. It can be executed as many times as needed, since there is usually not a new measurement available at each time step. The *a posteriori* update corrects the *a priori* estimate with a weighted correction introduced by a new measurement. The weight is given by the Kalman gain K_n.

Extended Kalman Filter Algorithm

In the case in which the state model is non-linear, a first order linear model can be implemented. The resulting estimator of the state vector is known as *extended Kalman*

filter (EKF). Let the state model be

$$\mathbf{x}_{n+1} = \Phi(\mathbf{x}_n) + \Gamma(\mathbf{w}_n), \tag{3.36}$$

$$\mathbf{z}_n = C\,\mathbf{x}_n + \mathbf{n}_n, \tag{3.37}$$

with first order expansions:

$$\Phi(\mathbf{x}_n) = \Phi(\hat{\mathbf{x}}_n) + J_\Phi[\mathbf{x}_n - \hat{\mathbf{x}}_n], \tag{3.38}$$

$$\Gamma(\mathbf{w}_n) = \Gamma(\hat{\mathbf{w}}_n) + J_\Gamma[\mathbf{w}_n - \hat{\mathbf{w}}_n], \tag{3.39}$$

where J_Φ and J_Γ are the Jacobian of Φ and Γ respectively.

The Kalman chain becomes [40]:

- *Measurement update.* Acquire z_n and compute *a posteriori* quantities:

$$K_n = \frac{P_n^- C^T}{C\,P_n^- C^T + R} \tag{3.40}$$

$$\hat{\mathbf{x}}_n = \hat{\mathbf{x}}_n^- + K_n\left[z_n - C\,\hat{\mathbf{x}}_n^-\right] \tag{3.41}$$

$$P_n = P_n^- - K_n\,C\,P_n^- \tag{3.42}$$

- *Time update.* Compute *a priori* quantities for time $n+1$:

$$\hat{\mathbf{x}}_n^- = \Phi(\hat{\mathbf{x}}_n), \tag{3.43}$$

$$P_n^- = J_\Phi\,P_n J_\Phi^T + J_\Gamma Q J_\Gamma^T. \tag{3.44}$$

- *Time increment.* Increment n and repeat.

3.4.2 Gondola State Model

We now want to obtain an estimate of the gondola attitude quaternion at each time step n. The state model is built upon the quaternion time propagator, as defined in Equation 3.14. The gyro-measured angular rates need to be corrected by a slow-varying DC bias that accounts for the zero point of the gyros. As seen in Section 2.2.3, the bias can be thought as being driven by a stochastic random walk process.

The bias (a 3-vector) and the attitude quaternion form a state vector of dimension 7.

The state model used in our analysis is defined as:

$$\mathbf{b}_{n+1} = \mathbf{b}_n + \mathbf{w}_{\mathbf{b}n}, \tag{3.45}$$

$$q_{n+1} = \begin{pmatrix} 1 \\ \frac{1}{2}\omega_n \Delta T \end{pmatrix} q_n + \begin{pmatrix} 0 \\ \frac{1}{2}\mathbf{b}_n \Delta T \end{pmatrix} q_n + \begin{pmatrix} 0 \\ \frac{1}{2}\mathbf{w}_{\omega n} \Delta T \end{pmatrix} q_n, \tag{3.46}$$

$$\mathbf{z} = C \begin{pmatrix} \mathbf{b} \\ q \end{pmatrix}. \tag{3.47}$$

- Equation 3.45 propagates the gyro biases assuming that any change is due to random process noise $\mathbf{w}_{\mathbf{b}n}$;

- Equation 3.45 propagates the attitude quaternion (eq. 3.14) and includes the noise $\mathbf{w}_{\omega n}$ on the gyroscope angular rates ω_n;

This non-linear model needs to be expressed as a first order liner Equations in order to apply the EKF machinery.

Defined below are the matrices used in our implementation of the filter (given here for reference).

$$C = \left(\begin{array}{ccc|cccc} 0 & 0 & 0 & 1 & 0 & 0 & 0 \\ 0 & 0 & 0 & 0 & 1 & 0 & 0 \\ 0 & 0 & 0 & 0 & 0 & 1 & 0 \\ 0 & 0 & 0 & 0 & 0 & 0 & 1 \end{array}\right) \qquad J_\Gamma = \frac{\partial}{\partial(\mathbf{w_b}, \mathbf{w}_\omega)} \begin{pmatrix} \mathbf{b} \\ q \end{pmatrix} = \left(\begin{array}{ccc|ccc} 1 & 0 & 0 & 0 & 0 & 0 \\ 0 & 1 & 0 & 0 & 0 & 0 \\ 0 & 0 & 1 & 0 & 0 & 0 \\ \hline 0 & 0 & 0 & -q_1 & -q_2 & -q_3 \\ 0 & 0 & 0 & q_0 & q_3 & -q_2 \\ 0 & 0 & 0 & -q_3 & q_0 & q_1 \\ 0 & 0 & 0 & q_2 & -q_1 & q_0 \end{array}\right)$$

$$Q = \left(\begin{array}{ccc|ccc} \sigma_{b_1}^2 & 0 & 0 & 0 & 0 & 0 \\ 0 & \sigma_{b_2}^2 & 0 & 0 & 0 & 0 \\ 0 & 0 & \sigma_{b_3}^2 & 0 & 0 & 0 \\ \hline 0 & 0 & 0 & \sigma_{\omega_1}^2 & 0 & 0 \\ 0 & 0 & 0 & 0 & \sigma_{\omega_2}^2 & 0 \\ 0 & 0 & 0 & 0 & 0 & \sigma_{\omega_3}^2 \end{array}\right) \qquad R = \begin{pmatrix} \sigma_{sc_0}^2 & 0 & 0 & 0 \\ 0 & \sigma_{sc_1}^2 & 0 & 0 \\ 0 & 0 & \sigma_{sc_2}^2 & 0 \\ 0 & 0 & 0 & \sigma_{sc_3}^2 \end{pmatrix}.$$

Finally, J_Φ is evaluated numerically in our implementation of the EKF.

Initialization

The time iteration of the EKF is initialized by setting the initial value of the state vector to have zero gyro bias. The initial state quaternion at time zero is pre-loaded with the first available star camera reading. Finally the covariance $P_{n=0}$ is set to $J_\Gamma Q J_\Gamma^T$. The resulting filter is stable and converges after few time steps.

3.5 Pointing Reconstruction

We have developed software that implements the described extended Kalman filter. It takes the orthogonalized gyroscopes and the star camera pointing solution as inputs. It then iterates in time to obtain a time-forward pointing solution. The filter is also run backwards in time over the same inputs. The two solutions could then be combined together in a MMSE way using a Kalman smoother (see [40]), but we chose not to. Instead, we weight-averaged the solutions, using the covariance matrices P^f and P^b as weights (here f and p refers to the forward and backward solutions, respectively). We found this method to be extremely well behaved.

The rationale behind this dual solution is shown in Figure 3.2. The error on the estimate of the q_n is minimum when a measurement z_n is available, and grows as $\sim \sqrt{t}$ until a new measurement is available. To reduce the error divergence, it is then possible to run the filter backward in time and average the two to obtain a smoother solution.

Using just one star camera and the digital gyros, the final averaged attitude is better than 3″ RMS; one example is shown in Figures 3.3 and 3.4.

Given the non-nominal beam sizes of the Sweden flight (see section 5.10), this accuracy is more than fine to analyze data collected in that campaign.

This result can be improved once the second set of gyroscopes and star camera are included in the solution. Improvement of $\sqrt{2}$ to 2[2] can be reasonably expected, and will be pursued for the analysis of the Antarctic data-set.

The pointing sensors and the pointing reconstruction pipe-line are therefore able to deliver a pointing accuracy very close or equal to 1.5" RMS, as required by the arguments

[2]A $\sqrt{2}$ improvement from using one more set of gyroscopes and one other $\sqrt{2}$from using the second star tracker.

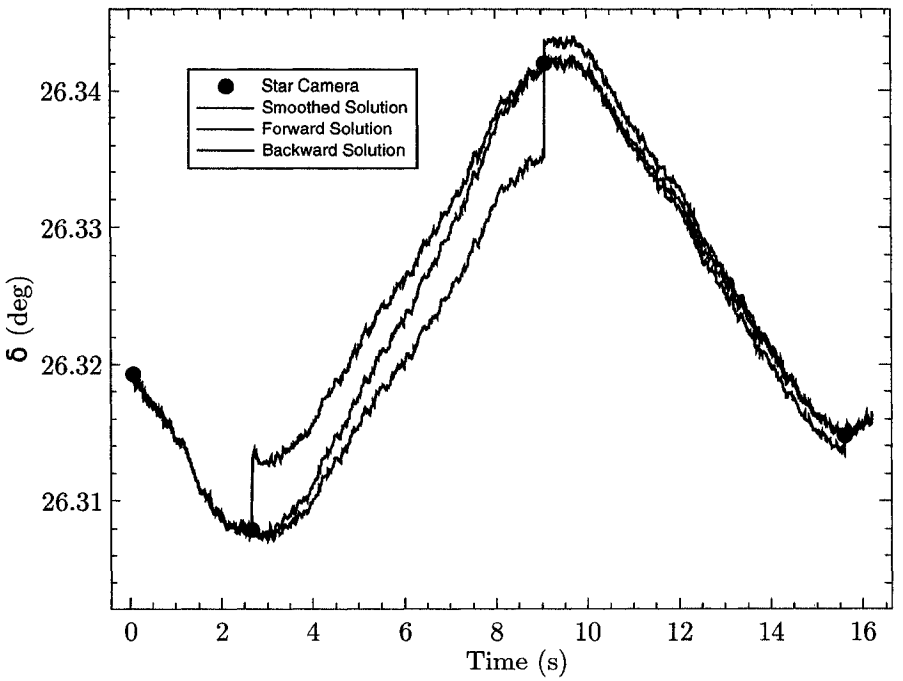

Figure 3.2: An example of the Kalman pointing solution. The filter is run forward and backward in time. The two solution are then weight-averaged together to reduce the random walk error induced by the gyroscopes.

given in Section 3.1.

3.6 Dual Axis Platform

While the star camera pointing solution accuracy has met the requirements in $[\alpha, \delta]$, the information about the rotation angle (rotation about the beam direction) is constrained to about 0.1°. It can been shown that this term enters in the pointing error budget with a cosine and it is a second order effect. On the other hand, a higher accuracy on the roll helps to smooth the behavior of the Kalman filter. Moreover, future CMB polarimetric experiment require a control on the roll at about the limit of the camera.

Roll determination can be improved using the GPS horizontal velocity [41], which is accurate to $\sim$ 0.1 m/s RMS, and the level sensors or clinometers (see [42] and [43] for

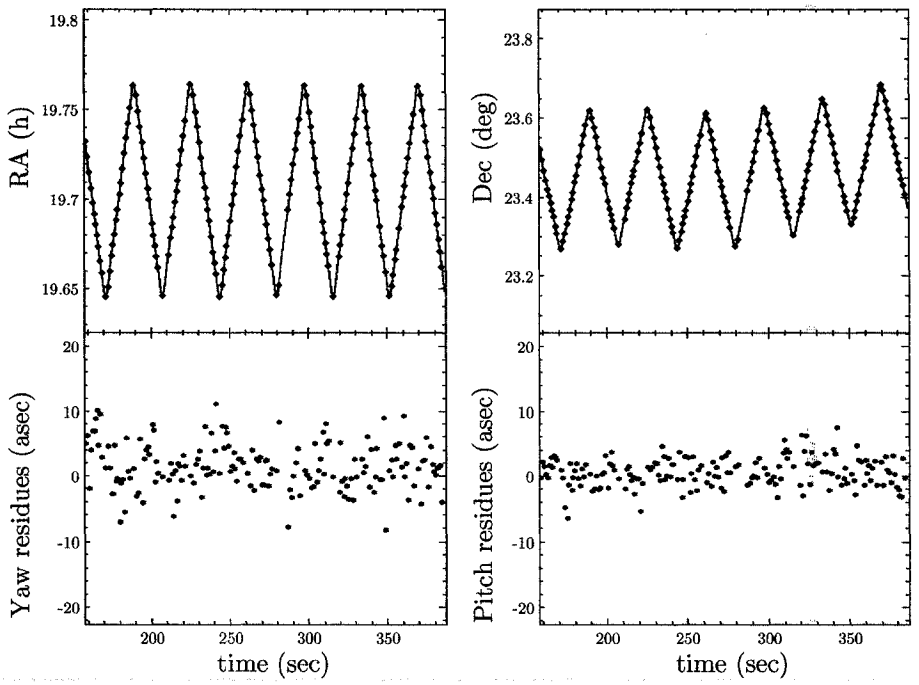

Figure 3.3: An example of pointing reconstruction from the Kiruna data. In the top plots, the solid blue lines represent the reconstructed pointing solution obtained integrating one set of gyroscopes onto one of the two star cameras. There, dots represent the positions reported by the other star camera, which is not used in the solution. The bottom plots show the residues as yaw ($\sim \Delta\mathrm{Ra} * \cos(\mathrm{Dec})$) and pitch (coincident with the declination in this particular case).

use of clinometers in attitude reconstruction where a Single Axis Platform is described). The gondola is a composite pendulum:

$$L_{\mathrm{eff}}\,\ddot{\alpha} = -g\,\alpha \tag{3.48}$$

where L_{eff} is the effective length of the pendulum and α is the angular amplitude of the oscillation.

An estimate of $\ddot{\alpha}$ is obtained differentiating the GPS horizontal velocity, low-pass filtered with a 4^{th} order Butterworth [44] at 1 Hz. This determines only variations and it does not include the absolute angle. While the clinometers cannot detect gondola oscillations, they are sensitive to static tilts of the payload. The low-pass filtered clinometer pitch

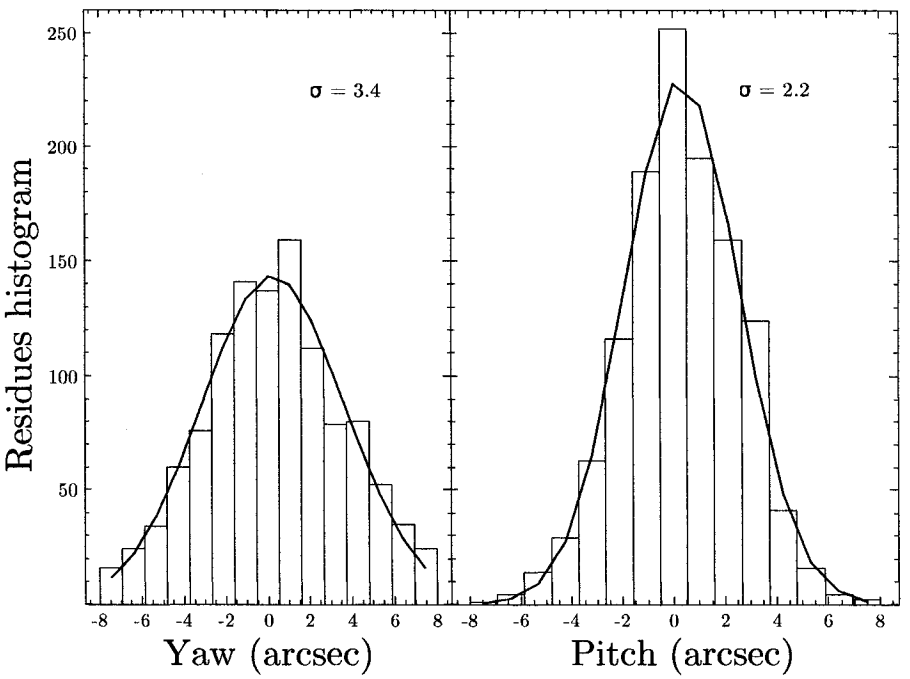

Figure 3.4: Histograms of the pitch and yaw residues from plot 3.3. The solid lines are Gaussian fits whose standard deviations are shown in these panels. The overall error of the pointing solution can be obtained summing in quadrature the standard deviations divided by 2 (the errors are uncorrelated between the two cameras) : $\sigma_p \simeq 2.8''$ RMS. The yaw residuals histogram is slightly wider since the telescope scans in azimuth, close to RA at the BLAST latitudes. The projection of this angular velocity along the yaw axis is always larger than the pitch axis for the elevation range of the telescope (25°–58°), and hence the star centroids in star camera images have larger measurement errors in that direction. This result can be improved as described in Section 3.5.

and roll signals (at 5 mHz with the same 4^{th} order Butterworth) are therefore used as an estimate of the absolute angle.

α is then rotated into pitch, cross-correlating the gondola pitch estimate (the elevation from the pointing solution subtracted from the elevation encoder) with α itself. Roll can be estimated as the orthogonal component to pitch in α. DC components from the low-passed clinometer are then added to these estimates. This procedure works very well as shown in Figure 3.5, and can provide accuracies of $\sim 18''$ RMS. It is worth noting that this is the accuracy of the elevation encoder, used in this estimate of the error.

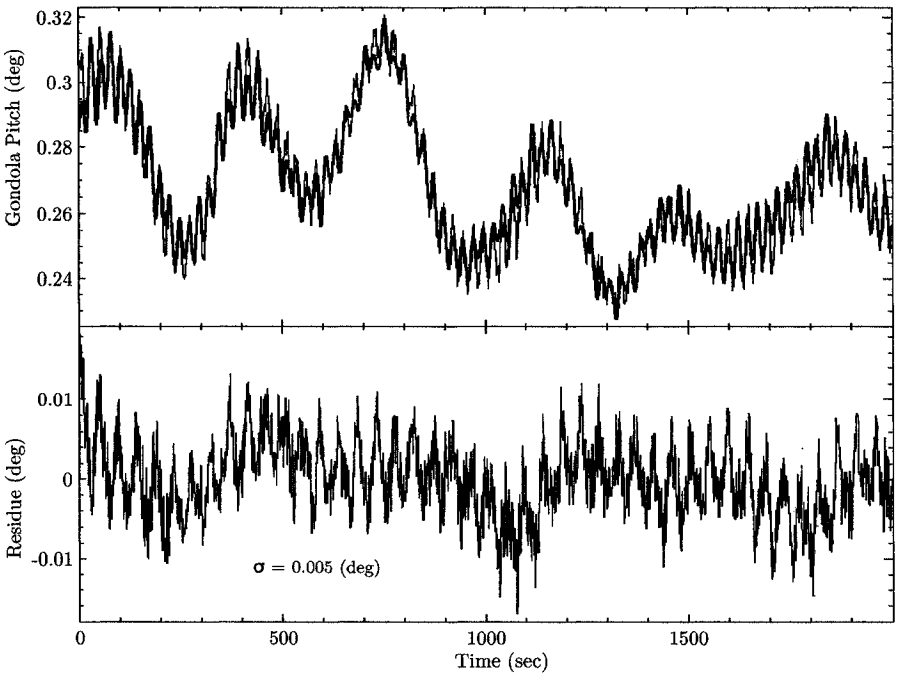

Figure 3.5: Top panel: comparison of the pitch derived from the GPS velocity (red) and from the Star Camera (black). Bottom panel: the residual of these two quantities shows an RMS of 0.005 deg (18").

3.7 Gondola motions

The gondola fundamental motions are shown in Figure 3.6. Azimuth is from the Kalman pointing solution; pitch and roll are calculated using the GPS velocity method discussed in the previous section.

The azimuth triangular scan appears in the spectrum as its fundamental and odd harmonics. This motion couples to pitch and roll where it is detected at a lower level (few arc seconds).

The pendulum fundamental harmonic is visible in the pitch and roll spectra with a period of 0.4 min. This translates to an effective length (Equation 3.48) of the flight chain of $L_{eff} \sim 143$ m.

This shows that the scan was poorly coupled to pitch and roll. Motion of the payload in

these two Euler angles are dominated by the balloon natural oscillations.

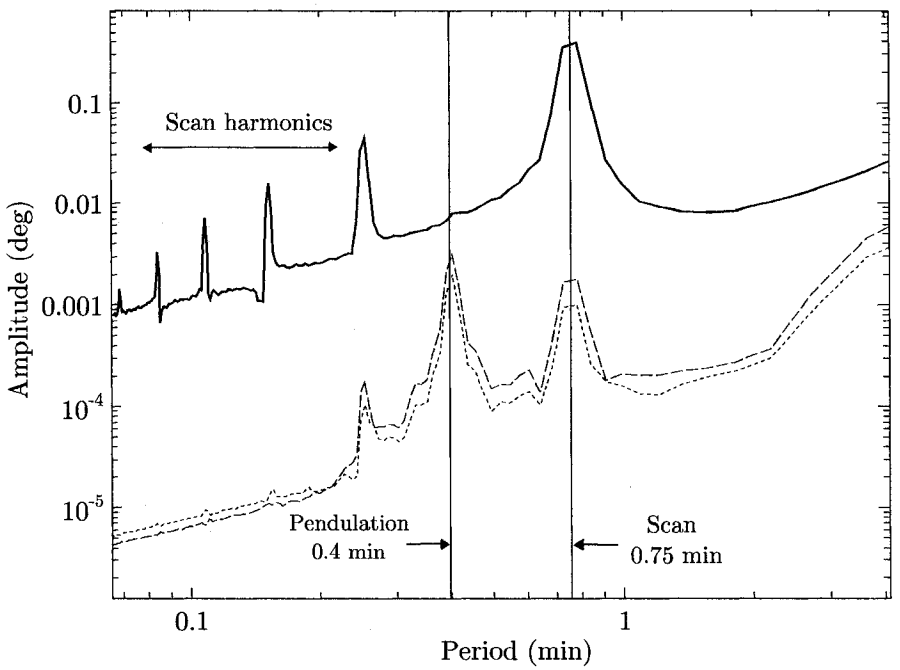

Figure 3.6: Fundamental oscillatory modes for the gondola scanning at float: azimuth (solid), pitch (short dash) and roll (long dash). The vertical lines show the pendulum fundamental at a period of 0.4 min and the triangular scan first harmonic at 0.75 min. Note the odd harmonics of the triangular scan wave.

Chapter 4

Blast Optical Bands

4.1 Array Band Definition

BLAST bands at 250 μm, 350 μm, and 500 μm are defined by a combination of dichroic low-pass edge beam splitters, metal mesh reflective filters, and feed-horn wave guide cutoffs. Filter technology is reviewed in [45].

Low-pass edge dichroic filters split the incoming radiation from M5 (see Figure 2.2). The first dichroic reflects wavelengths shorter than 300 μm and transmits longer wavelengths. The bandpass for the 250 μm array is further defined by a filter directly in front of the array, which reflects wavelengths shorter than 215 μm, and by the waveguide cutoff at the exit of each of the feedhorns. For the 350 μm array, the band is defined at the short wavelength end by what is transmitted by the first dichroic, and at the long wavelength end by the waveguide cutoff. The 500 μm band is defined on the short wavelength end by the transmitted radiation from the second dichroic and on the long wavelength end by the feedhorn cutoff. Each band has a 30% width. The filter stack frequency performance is evaluated with Fourier transform spectroscopy (next Section) and is plotted in Figure 4.2.

4.2 Fourier Transform Spectroscopy of Bandpasses

The optical spectral response of the receiver is measured before flight.

A Fourier transform spectrometer (FTS) was custom built, based on the polarizing version of the Michelson interferometer, which was first implemented by Martin and Puplett [46] and Martin [47].

The FTS is used in transmission, and the BLAST receiver was placed at the output of the instrument. A Martin-Puplett measures the difference of two input loads that were liquid nitrogen 77 K, and 300 K black bodies. Making use of polirizing beam splitters ensure that no spectral arctifacts are induced in the output signal, and erroneusly interpreted as real bandpasses features.

Saturated water absorption lines are present at BLAST frequencies. Absorption is so strong that submillimeter targets cannot be observed even when placed at moderate distance from the telescope. Similarly, doing FTS measurements in open air affects the ability to properly identify features in the bandpasses. For this reason, the FTS was contained in a vacuum-tight shell, connected to the cryostat front window with a hermetic seal. The system was then evacuated and the measurement performed.

Several interferograms were acquired (Figure 4.1), and Fourier-transformed as explained in Appendix A. Each spectum was phase-corrected to account for a linear phase-error (as it arises when the readout electronics does not sample the interferogram at Zero Path Difference). Several spectra were co-added togather, and the black body spectral response removed as discussed in Section A.2 and Equation A.13.

The final, black body corrected spectral responses of representative 250 μm, 350 μm, and 500 μm detectors are shown in Figure 4.2. The residual water lines indicated in this Figure are identified using Hitran. The measured transmission spectra are consistent

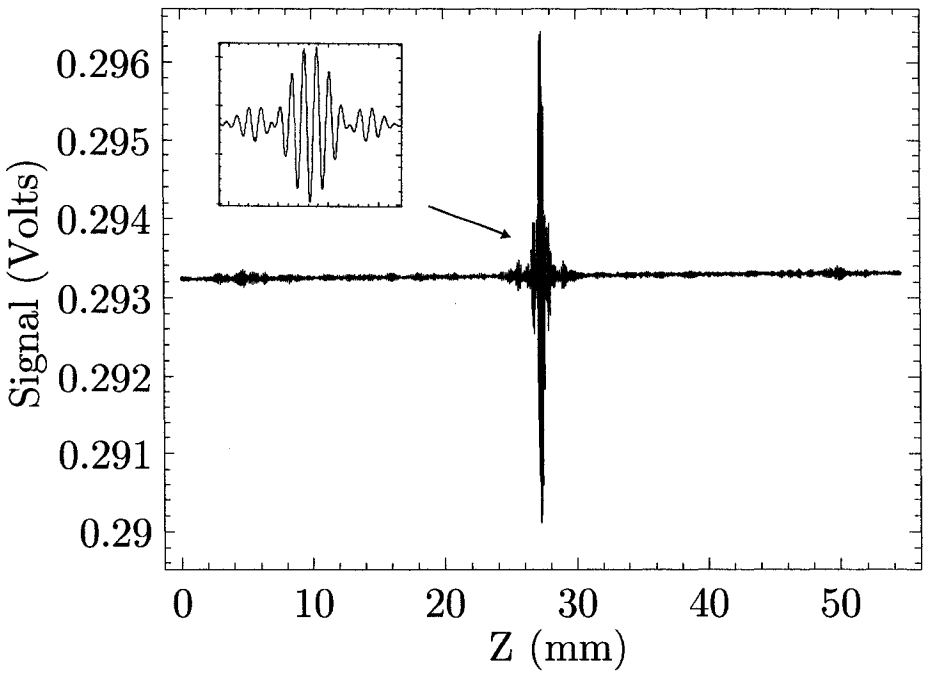

Figure 4.1: Interferogram of a representative 250 μm channel.

with the expected positions and widths of each bandpass. The spectroscopy also shows that standing waves are present in all the channels, and the strengths of these resonances vary somewhat for adjacent horns.

The spectra are clearly affected by an uncorrected phase error[1] which appears as a leak in the bandpass. Analysis of the phases (also shown in Figure 4.2) shows a null component in-band. The phase has a not-null, not-random behavior at the edge of the bands. This suggests that the signal which is inducing this phase error is not the main signal from the interferometer. Therefore, the problem is likely to lie in the FTS itself, more than being caused by the filter stack.

[1]This is a different phase error from the one induced by not sampling the interferogram at ZPD.

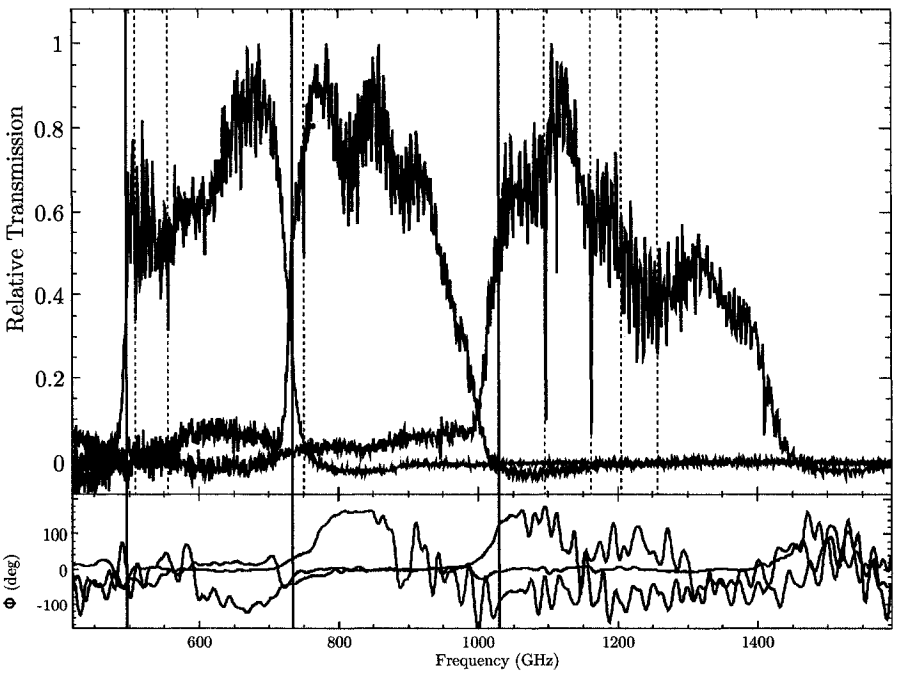

Figure 4.2: BLAST bandpass responses. Top panel: the bandpass for representative 250 μm, 350 μm, and 500 μm channels. The vertical, dashed lines indicate the frequency of the residual water lines visible in the spectra. The vertical solid lines show the frequency waveguide cutoffs. An uncorrected phase (plotted in the bottom panel) error is visible in all the channels. This is consistent with a problem that is likely to be found in the FTS used.

Chapter 5

Data Reduction

BLAST measures temperatures in the sky and generates time streams. The object of the data reduction is to clean these time streams of all the pathologies they might suffer, and turn them into calibrated maps by making use of the pointing solution derived in Section 3.5,

During the 4.5 day Kiruna flight in June of 2005, the instrument performed well, except for degraded optical performance. This was possibly due to a failure of structural elements in the carbon fiber mirror, and resulted in decreased resolution, which had a significant impact on our ability to achieve our extragalactic science goals. BLAST acquired 100 hours of data on Galactic targets, providing some of the first arcminute resolution images at these wavelengths. In this flight, surveys were conducted of five star forming regions, including the well-studied Cygnus-X field, three regions of intermediate/high-velocity cirrus, the Cas-A supernova remnant, several individual bright targets, and the ELAIS-N1 extragalactic field.

In the following sections I will review the processes involved in the reduction of the data into calibrated maps, and I will conclude by discussing the performance of BLAST in the

Kiruna flight.

5.1 Despiking

Glitches in the time streams have multiple origins. They need to be identified and flagged so that they will not be used in the analysis. Here I discuss a method I have implemented to de-glitch the time streams. An independent method is described in [48]. These two approaches have been compared on a statistical basis. A histogram of the deglitched dataset was evaluated for both methods. The two histograms were found to be the same, within the noise, showing the equivalence of both approaches.

Calibration Lamp Pulses

The calibration lamp in the Lyot stop is lit at time regular intervals to monitor responsivity drifts. It generates an optical signal that needs to be removed. The data acquisition system of the telescope records these events making it easy to find and flag the pulses.

Data Acquisition Glitches

These are single samples in a time stream that appear as spikes. They are generated by timing errors in the data acquisition electronics. These events are identified in the time stream by looking at isolated and sudden changes in the numerical value of samples.

Cosmic Ray Spikes

Cosmic Rays (CR) are energetic particles originating beyond the Earth. When a CR hits a bolometer, it transfers some of its energy, causing the detector to warm up. Similarly,

when a CR hits a metal block, it generates a shower of γ-rays by bremsstrahlung. If this happens in the proximity of the detectors, the γ-rays can hit several bolometers at once, warming them up simultaneously. The time scales at which these events occur is much shorter than the detector and acquisition time constants. The resulting signal is close to a delta function, convolved with the bolometer and electronic impulse responses.

It is difficult to identify and remove CR events from time streams where bright sources are present, since a source could be confused for a CR, and vice versa.

I addressed this issue by developing a wavelet-based method to identify CR events. The technique is discussed in detail in [49]. It is based upon the principle that a delta function has power at all frequencies in the Fourier domain. On the contrary, astronomical sources appear to be band limited, with the highest frequency depending on the angular rate at which the finite resolution telescope is scanning the source. Therefore, it is possible to high-pass the time streams so that the astronomical sources are filtered out, with only the CR left after this operation. The wavelet used (a Morlet wavelet) is a matched filter for the detection of CR spikes.

γ-ray showers could strike the detectors at a level fainter than the noise in the time stream, but they hit several bolometers at the same time. To detect and flag these events, several channels are averaged together to have the spike emerge from the noise. The de-spiking code is run once more on this combined time stream, and the newly discovered events are flagged.

Other Glitches

These are events that do not belong to any of the categories discussed so far. While a CR always warms up the detector, some glitches look like a drift whose temporal duration is comparable to a CR event. They are different in shape and could be either positive or

negative. These events are flagged using the same wavelet method adopted to identify cosmic rays.

Gap Filling

Flagged data are not used in the reduction, but spikes need to be removed prior to any filtering of a time stream. Gaps are filled with a realization of the noise, based on a linear prediction algorithm [50]. Two independent noise realizations are generated, both forward and backward in time. These two sets are then weighted together and added to the gap left in the data, after the polluted section has been removed.

5.2 Transfer Function

The astronomical signal of interest is time-filtered before it is digitally stored. The filters have a non uniform gain as a function of frequency. BLAST calibrates using point sources, and this calibration is not constant for targets with a different spatial spectral signature, if the effect of the filters is ignored.

Therefore it is important to be able to characterize and measure the various filters to ultimately deconvolve their response from the data. The "Transfer Functions" of the system are:

- the analog electronics response;
- the digital lock-in;
- the bolometer optical response.

5.2.1 Electronics Transfer Function

The analog signal, read at the detector end, is pre-amplified with a JFET and an analog amplifier. A single pole band pass is centered at the bias frequency and it is implemented on the preamplifier side. The main function of this filter is to remove the DC level. The frequency response, $T_e(\omega)$, of this section of the electronics is measured in the lab with a spectrum analyzer. The signal from the sky, $S(t)$, is slow compared to the bias frequency, ω_b, that modulates the bolometric detector. The effect of artificially modulating $S(t)$ with the bias is

$$F(t) = S(t)\cos(\omega_b t) \xrightarrow{FT} F(\omega) = \frac{1}{2}\left[S(\omega - \omega_b) + S(\omega + \omega_b)\right]. \tag{5.1}$$

$F(\omega)$ is filtered by $T_e(\omega)$ and convolved with the reference. Hence the locked-in signal is

$$\frac{1}{2}\left[T_e(\omega + \omega_b) + T_e(\omega - \omega_b)\right] S(\omega). \tag{5.2}$$

Here, the quantity multiplying $S(\omega)$ is the analog electronic transfer function (see Figure 5.1).

The signal is then digitized and locked-in. The digital lock-in anti-aliasing filter is a low-pass 4-pole filter that is implemented in the time domain as a 4-stage boxcar, where the output of one stage is fed into to the next one. The support[1] of each stage is $\Delta t_1 = 19.968$, $\Delta t_2 = 16.800$, $\Delta t_3 = 14.112$, $\Delta t_4 = 11.808$ ms, respectively. In the frequency domain, this is just the product of 4 sync functions

$$\prod_{i=1\ldots4} sync(\pi f \Delta t_i). \tag{5.3}$$

[1]The support of a function f (or of a generalized function, or distribution) is the closure of that subset of the domain of definition on which the function assumes a nonzero value.

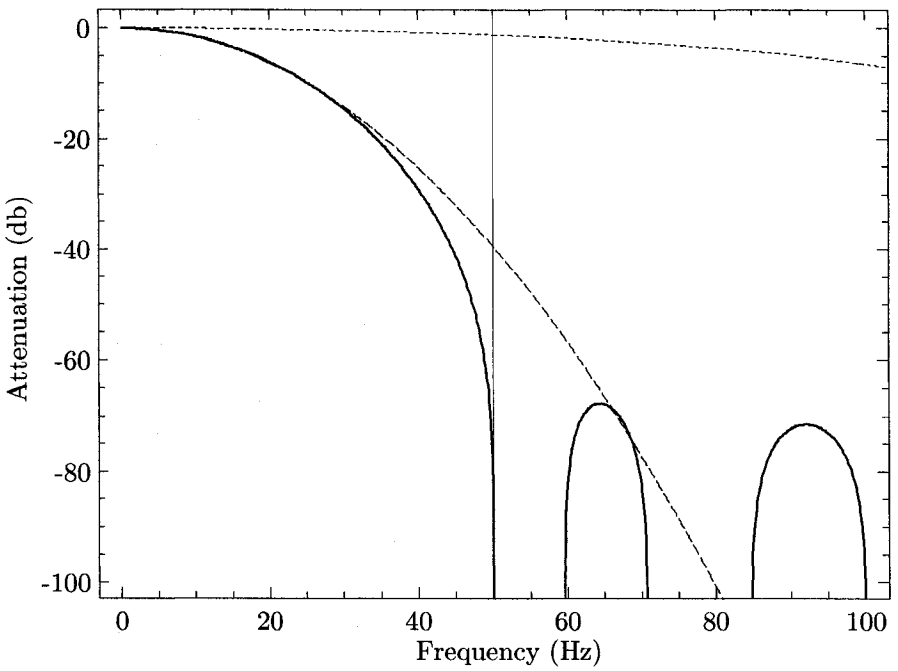

Figure 5.1: The electronics transfer functions. The anti-aliasing filter is plotted as a solid line. This filter is a good approximation of a Gaussian (long dashed line). The dot-dashed line is the analog electronics transfer function of Equation 5.2 and the vertical line marks the Nyquist frequency of 50 Hz.

This filter is the lock-in transfer function and is a good approximation of a Gaussian, but its implementation is both arithmetically and computationally more efficient than a Fourier domain filter. The anti-aliasing filter has a first null at the Nyquist frequency of the system which is 1/4 of the bias frequency (Figure 5.1).

5.2.2 Detector Transfer Function

The single bolometric channel impulse response is well described by

$$\frac{1}{\tau_1} e^{-2\pi t/\tau_1} + \frac{\epsilon}{\tau_2} e^{-2\pi t/\tau_2} \tag{5.4}$$

This is a straightforward result obtained by solving the bolometer equation (see [51, 52]), for the case of two thermal conductances, as done in [49].

When a charged particle hits a bolometer, some amount of energy is transferred to the detector on a typical time scale which is much shorter than the time constants. Therefore, CR are ideal impulses that can be used to estimate the transfer function. For this purpose, a collection of several high signal-to-noise events are stacked together on a time grid with a resolution 8 times larger than the fundamental. This is achieved by oversampling each of the CR by using the sampling theorem [50]. This method guarantees that the information content of the data being used is not changed. The CR are then matched in phase (by cross-correlating them) and in amplitude (by least-square minimization), and co-added to give a high-resolution, low-noise estimate of the impulse response in the time domain as shown in Figure 5.2.

Each bin in the template of Figure 5.2 is averaged. The Fourier transform of the "average" cosmic ray built in this way is the experiment's transfer function.

The use of an oversampled time grid also minimizes the aliasing of frequencies above the Nyquist frequency. This reduces the error one would introduce in the estimation of the transfer function at the high frequency end of the spectrum.

Figure 5.3 shows the transfer function calculated with this method, as well as the known electronic transfer function. The ratio of the two is the Fourier transform of Equation 5.4:

$$T(f) = \left| \frac{1}{1 + jf\tau_1} + \frac{\epsilon}{1 + jf\tau_2} \right|. \tag{5.5}$$

Fitting this function to the data we get:

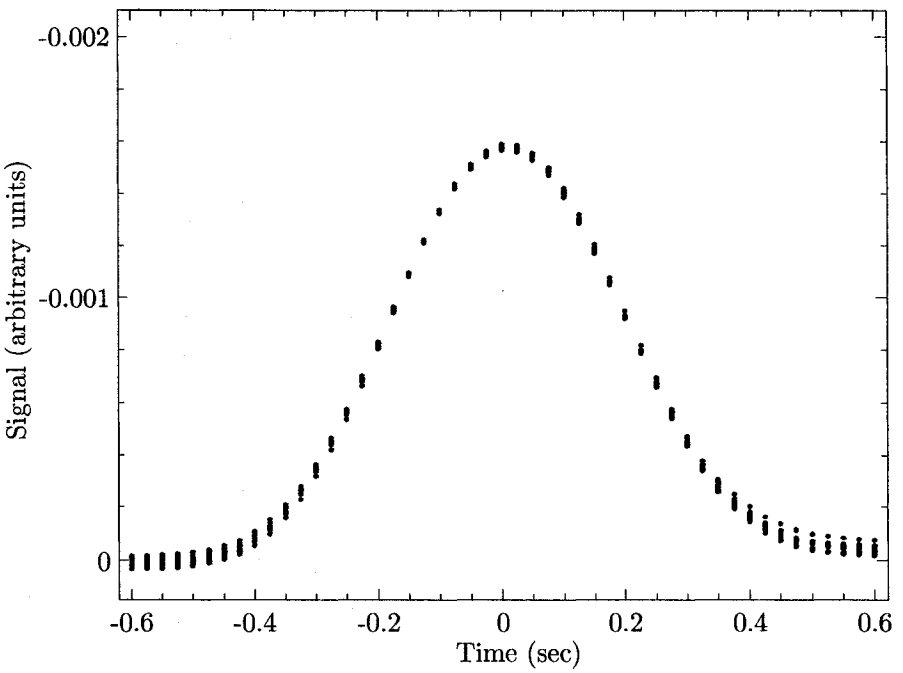

Figure 5.2: A set of 10 high signal-to-noise cosmic rays phase shifted and amplitude normalized. Each sample in a bin is co-added into an low-noise, time-oversampled estimate of the system impulse response. The Fourier transform is the transfer function shown in Figure 5.3

τ_1 (ms)	11.6	$\pm$	0.4
τ_2 (ms)	296	$\pm$	39
ϵ	0.086	$\pm$	0.005

If the second time constant is ignored in the deconvolution, an error is introduced at low frequencies, typically for diffuse targets. This is quantified in Figure 5.4, and can be as large as 5%.

5.3 Map Making

Each time stream measures

$$d_i(t) = S(t) + n_i(t) \tag{5.6}$$

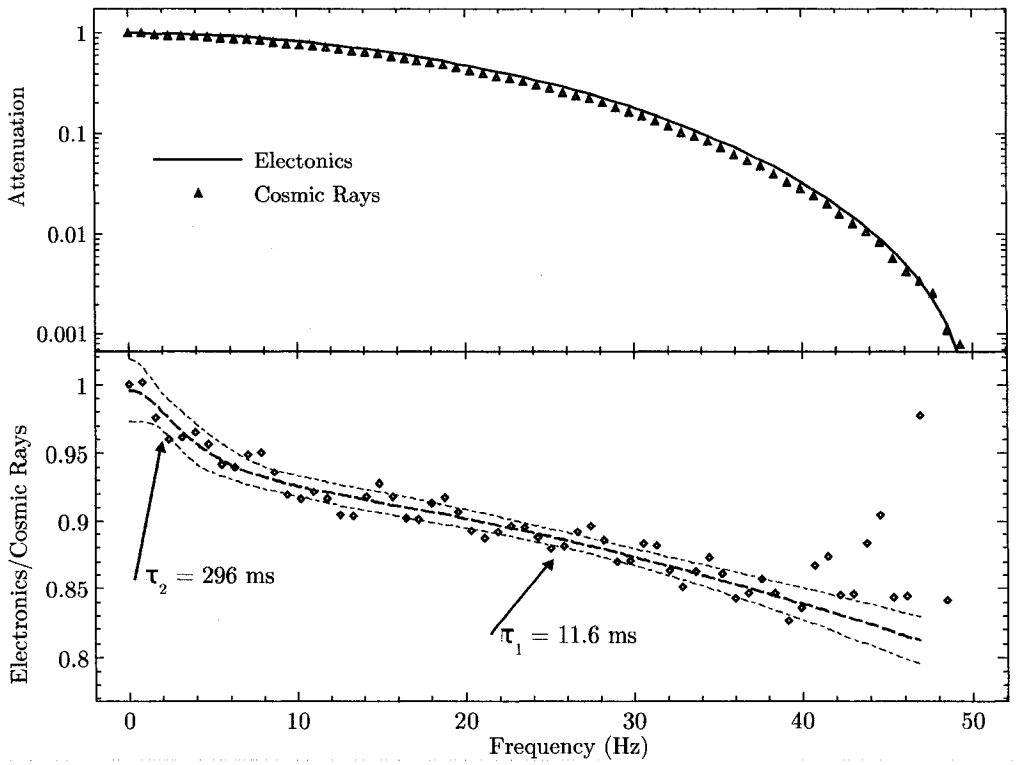

Figure 5.3: The BLAST transfer function generated with the cosmic rays method is shown as triangles in the top panel along with the electronic transfer function (solid line) as a function of frequency. The ratio of the two is plotted in the bottom panel (diamonds). Two time constants are clearly visible. The fit of Equation 5.5 is shown by the dashed line and the 3σ confidence levels by the dash-dotted lines. The short time constant (11.6 ms) is the optical time constant while the long one (296 ms) is related to the system thermalization after the shock of being hit by energetic, charged particles. Its effect, if ignored in the deconvolution, is to alter the low-frequency gain as shown in Figure 5.4.

where $d_i(t)$ is the i-th bolometer time stream as a function of the time t, $S(t)$ is the astronomical signal and $n_i(t)$ the noise. These time streams need to be processed into a map, making use of the pointing solution:

$$d_i(t) = A_{i\alpha}(t)M_\alpha + n_i(t). \tag{5.7}$$

Here M_α is the map and α is the pixel index; $A_{i\alpha}(t)$ is the pointing matrix that maps the pixel α to the time stream sample $d_i(t)$. Summation over repeated indices is assumed.

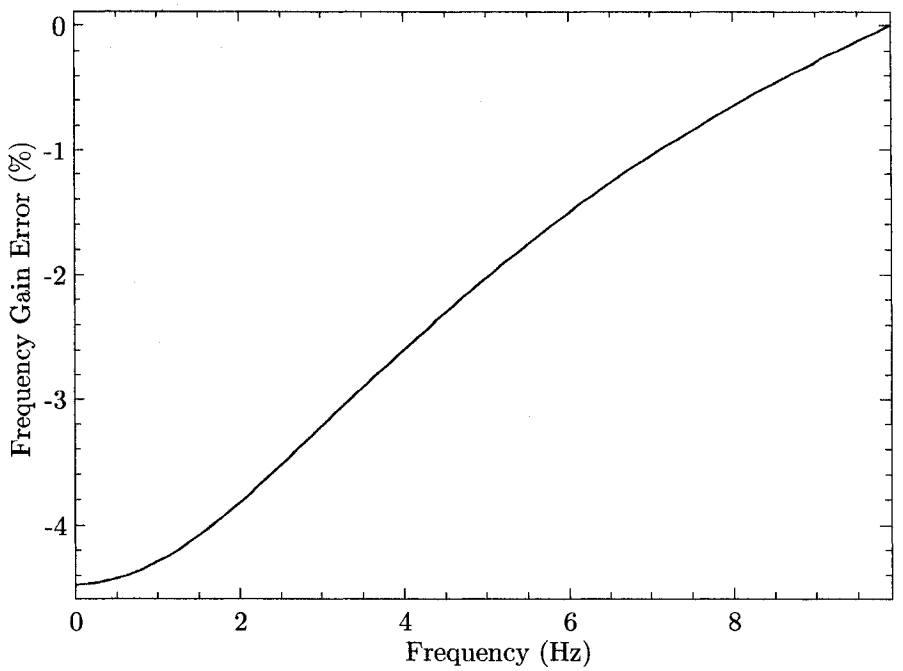

Figure 5.4: Low frequency gain error introduced if the second, long time constant discussed in Section 5.2 is ignored. A negative error means that the scale at the given frequency will be underestimated.

The map maker provides an estimate of the map given the time stream. In the assumption of Gaussian, stationary noise, the likelihood of the data is (suppressing the pixel indices here for convenience)

$$\log L(d|s) = -\frac{1}{2}(Wd - AM)^t N^{-1}(Wd - AM), \tag{5.8}$$

where $N \equiv \langle n \cdot n^t \rangle$ is the noise covariance matrix in the time domain, W is a filter applied to the time streams, and ^{t} denotes transpose. In this notation, W is an n-samples $\times$ n-samples matrix, so the operation of filtering (Wd) is as written, an impossibly slow operation. However, if W is a circulant matrix (i.e., every row is the same as the previous one, except shifted to the right by one) then the operation can be done in the Fourier domain: $Wd = F^{-1}(\omega F(d))$, where ω is the filter W in Fourier space and F is the Fourier transform operator. Maximizing the likelihood with respect to the map parameters M

leads to the following well known estimator:

$$\hat{M} = (A^t N^{-1} A)^{-1} A^t N^{-1} W d. \tag{5.9}$$

Two independent map makers have been implemented to solve Equation 5.9. One, (SANEPIC), described in [48], computes the noise covariance matrix and solves this equation directly by calculating the terms $A^t N^{-1} A$ and $A^t N^{-1} W d$. The second (ALMAGEST) uses an iterative solver similar to the one described in [53].

In the case where the noise covariance is replaced by the identity matrix, Equation 5.9 becomes a naive map. The naive map would clearly be the correct answer if d is described by white noise, and W is the identity matrix. In the case of real data, there are multiple problems with colored and correlated noise. If W is not the identity matrix (e.g., it filters out brown noise), it will modify $\hat{M}$. For example, the map will be filtered along the scan direction. W can also introduce stripe-like artifacts when the scan goes over a very bright source: the rest of the scan will be depressed by the high pass filter. In general, such an approach cannot be used whenever large angular scales are of interest.

Nonetheless, this map maker has the advantage that it is fast with respect to ALMAGEST and SANEPIC, making it suitable for use in Monte Carlo simulations. Moreover, for those extragalactic fields for which we are interested in faint point sources, the naive map maker generated maps are practically indistinguishable from the optimal.

Naive map making

A naive map maker is optimal when: i) data only has white noise, and ii) samples are weighted by the noise variance and binned into pixels (given the pointing solution).

In practice the time streams need to be high-pass filtered to remove the colored, low-

frequency noise (see Section 5.4).

First, a fifth-order polynomial is fit to the data and removed from each data segment in order to reduce fluctuations on time-scales larger than the length of the considered segment which, depending on the specific case, varies from 30 minutes to a few hours. These fluctuations are poorly described because of the limited number of Fourier modes, and would cause leakage at all time-scales (for instance a gradient in the timeline is described by a wide range of Fourier modes), degrading the efficiency of map-making. We experimented with various polynomials and other effective high-pass filters, but we found that the results were not very sensitive to precisely how this is done, although some such filtering is certainly required. The degree of the polynomial was chosen empirically such that the procedure gives better results without affecting the signal too much in final maps.

A simple cosine high-pass filter is then applied to each data segment to remove the low-frequency colored noise component; the filter support in the frequency domain is

$$\begin{cases} 0 & f < f_0 \\ 0.5 - 0.5\cos\left(\pi \frac{f-f0}{f1-f0}\right) & f_0 < f < f_1 \\ 1 & f > f_1 \end{cases} \tag{5.10}$$

where the frequency f_1 is empirically chosen (between 0.1 Hz and 0.2 Hz), and f_0 is set to 50% of the available band at f_1 (i.e. $f_1/2$).

The filtered time stream is binned into pixels rejecting flagged samples in both the data and pointing solution.

The naive map maker can be considered optimal in reconstructing angular scales affected by white noise only. Conversely, this map maker is far from optimal in reconstructing angular scales that are affected by low-frequency colored noise.

In particular for point sources, the naive maps are hardly distinguishable from the optimal. The spectral signature of a point source is, for the largest beam, more than 95% in the white noise regime. Therefore, filtering to remove colored noise attenuates very little of the astronomical signal. Moreover, being from 10 to 20 times faster than SANEPIC and ALMAGEST, the naive map maker is suitable for use in large Monte Carlo simulations.

5.4 Noise

The physical origin of noise in the measurement (see Equation 5.6), has roughly three origins: the photon noise induced by the incoming radiation, the detector noise (a complex mix of physical effects, see [51] and [52]), and amplifier electronic noise. In an ideal case, the noise is white and un-correlated among different detectors. In reality, this is not the case, as the noise is colored with a low frequency "brown" component described by a $1/f$ PSD ($1/f^2$ in power per unit bandwidth), and it is correlated among different channels. As shown in Figure 5.5, the noise PSD is white for frequencies above $\sim 0.2\,\mathrm{Hz}$, with a roll off at high frequency induced by the low-pass used in the deconvolution process. At lower frequency the spectrum has a $1/f$ shape with a knee at $\sim 0.15\,\mathrm{Hz}$. The cross power spectrum between two different channels is also shown in the figure, and indicates that correlations play an important role at frequencies below $0.2\,\mathrm{Hz}$.

Noise, thought of as a stochastic process affecting the measurement, can be correlated as a result of cross talking between detectors. This can arise in different stages of the detection process (light leakage between adjacent detectors, cross talk between wires, amplifiers, etc.). Correlations also arise from spurious signals that do not have an astrophysical origin: temperature drifts in the detector base plate, radiation from the telescope structure reaching the detectors, atmospheric residual emission, cosmic ray induced $\gamma-$ray

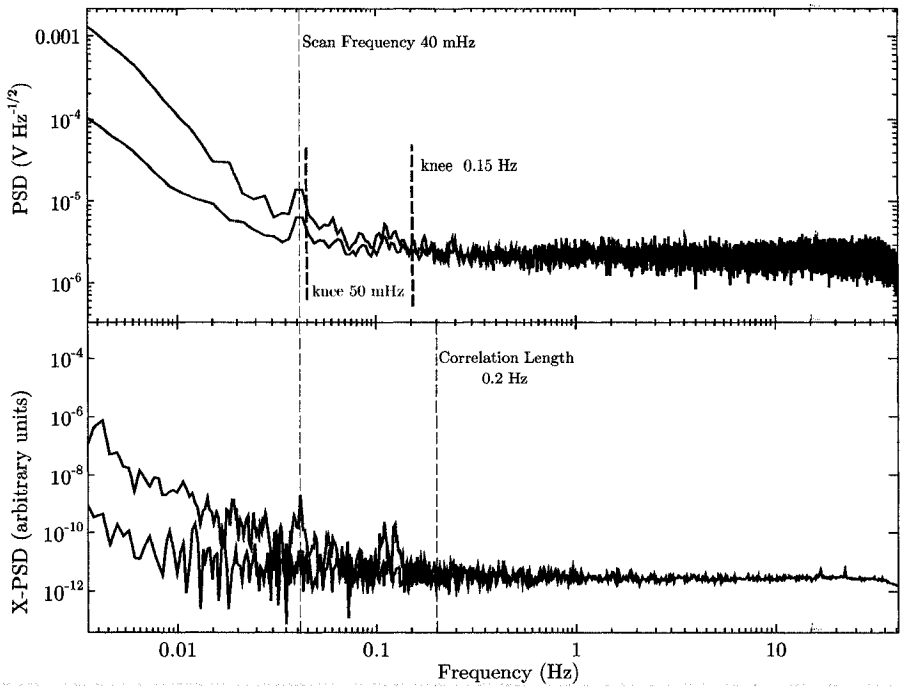

Figure 5.5: Noise in a deconvolved 250 μm channel. In the top panel the PSD acquired in the Kiruna flight is shown (black). The low frequency has a $1/f$ spectrum with a knee at ~ 0.15 Hz. Scan synchronous noise is also present as a feature at 40 mHz. In the bottom panel the cross-power spectum between this channel and one other 250 μm detector is plotted in black, and shows correlations up to a frequency of 0.2 to 0.3 Hz. The red curves show the same information after the common mode signal has been subtracted from the time streams. The noise PSD frequency knee is now moved to 50 mHz. The roll off at high frequency is introduced by the low-pass filter used in the deconvolution.

showers, etc. I will call these effects "correlated signals", to distinguish them from the correlated (stochastic) noise.

All these effects are also a source of $1/f$ noise. In particular, all the correlated signals are $1/f$ in nature and dominate the noise at low frequencies.

Correlated signals and correlated noise

To investigate the nature and the number of correlated signals, we have implemented a spectral decomposition analysis similar to the one described in [54]. The main assumption

is that the signal $d_i(t)$ measured by the i^{th} detector at a time t, can be written as

$$d_i(t) = S(t) + a_{ic} m_c(t) + n_i(t) \tag{5.11}$$

where $S(t)$ is the sky signal, as in Equation 5.6, $m_c(t)$ are correlated signals (the index c identifies the component), a_{ic} is a coefficient that expresses the amplitude of the component c on the detector i, and $n_i(t)$ is the noise. Summation over the repeated index c is assumed.

Performing this analysis on a extragalactic region, where the signal is negligible, the term $S(t)$ can be omitted, and, using a matrix notation

$$d(t) = Am(t) + n(t) \tag{5.12}$$

Fourier transforming this equation, and assuming that $m(t)$ is uncorrelated with $n(t)$, it is possible to work out the expression for the covariance matrices in the frequency domain (<> is the ensemble average operator):

$$< d(f)d^t(f) >= A < m(f)m^t(f) > A^t + < n(f)n^t(f) > \tag{5.13}$$

The method assumes that both $n(t)$ and $m(t)$ are uncorrelated, so that $< m(f)m^t(f) >$ and $< n(f)n^t(f) >$ are diagonal. It is then possible, given the data covariance matrix, to solve for the noise and the correlated signal power spectra, and the mixing matrix A.

This analysis has shown that, effectively, there is only one signal responsible for the correlations among detectors. Other components (if present) would give a second order effect and they cannot be reliably identified. Therefore, a simpler approach was used in which an estimate of the correlated signal is built averaging all the available detectors at a given time t. The amplitudes a_i are subsequentally evaluated correlating the cor-

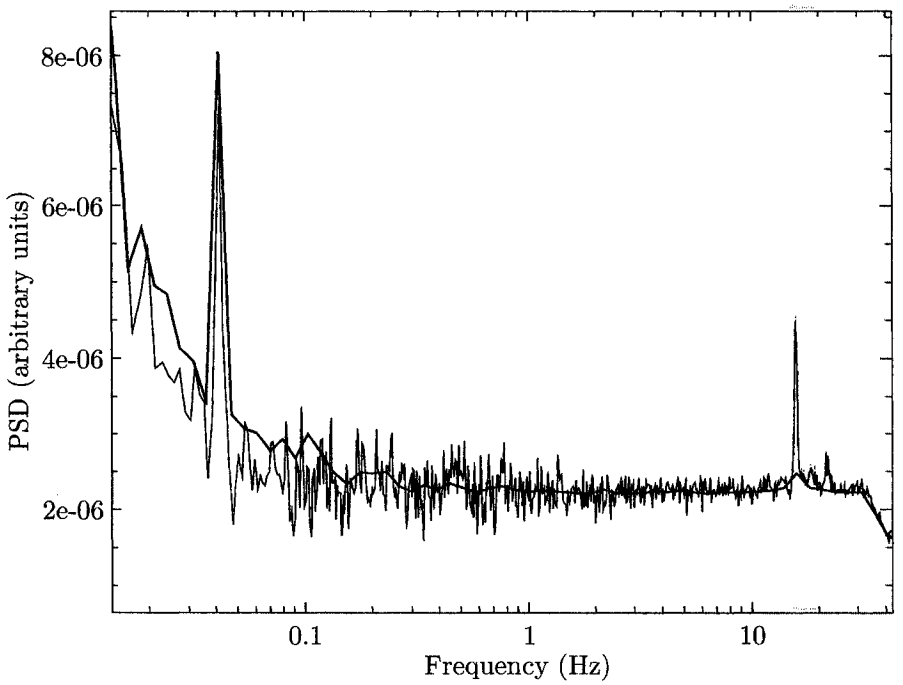

Figure 5.6: PSD of a 250 μm time stream, corrected for a correlated signal component. The red PSD is obtained with the spectral decomposition method of [54]. One estimate of the correlated signal can be obtained by averaging several detectors at a given color. This estimate can be subtracted from the time stream. The PSD of this corrected stream is shown in black. The agreement between the two curves indicates the equivalence of the two methods in evaluating the statistical properties of the signal.

related signal estimate with the detector i. This process is iterated until convergence is achieved. This simpler method provides one estimate of the power spectral densities that is equivalent to the ones obtained with the spectral decomposition method. An example is shown in Figure 5.6.

As shown in Figure 5.5, the correction in the time stream of this correlated signal, reduces the knee frequency of the detectors to about 50 mHz (but does not change the spectral signature that remains brown at lower frequencies).

Origin of the Correlated Signal

The single-component correlated signal is found to be correlated with many parameters (altitude and temperatures), and in particular with the temperature of the telescope's chin: the foremost scoop baffling the telescope, used here as a proxy for the temperature of the secondary mirror, which did not have a temperature sensor. We believe that this signal is loading from the supporting structure of the secondary mirror seen by the detector arrays.

We also investigated a possible contribution from the atmosphere. Such a component is expected to be proportional to both the residual atmospheric pressure (given in Equation 2.17) and to the airmass [20].

$$S_{\mathrm{atm}}(t) = A\,\mathrm{p}\,\chi(e) \tag{5.14}$$

where p is the atmospheric pressure, and $\chi(e)$ is the air mass at an elevation e. A is a constant.

To investigate the issue, a detector signal have been locked-in using the GPS altitude as the reference. Base lines are estimated with a fifth order polynomial fit, and subtracted. Data are subsequently high-passed with a 4^{th} order Butterworth at 40 mHz.

Let $\tilde{d}(t)$ and $\tilde{H}(t)$ be the base-line corrected, high-passed detector and altitude time streams, respectively, and write:

$$\tilde{d}^2(t) = K\,\tilde{d}(t)\,\tilde{H}(t). \tag{5.15}$$

Both sides of this equation are then low-passed with a 4^{th} order Butterworth at 1 Hz, and the constant K evaluated with a linear fit to the data. Figure 5.7 shows $\tilde{d}^2(t)$ and

$K\tilde{d}(t) * \tilde{H}(t)$ plotted versus time.

The analisis done fore the three colors finds K to be:

λ	K
	$(\mathrm{MJy\,sr^{-1}\,m^{-1}})$
$250\,\mu\mathrm{m}$	8.3
$350\,\mu\mathrm{m}$	3.8
$500\,\mu\mathrm{m}$	5.3

In the hypothesis of an atmospheric origin, the value K is

$$K = A\chi(\mathrm{e})\,\partial_H \mathrm{p}, \tag{5.16}$$

and a similar expression has to exist for the telescope elevation angle. The ratio of the two is

$$\frac{\chi(\mathrm{e})}{p}\,\frac{\partial_H \mathrm{p}}{\partial_e \chi(\mathrm{e})}\bigg|_{e=35^o, H=39\,\mathrm{km}} = \frac{1}{200} \tag{5.17}$$

Therefore, a change in elevation by 1 degree, would induce a signal 200 times larger than the one estimated from altitude alone. On the contrary, we don't see any reliable correlation between detectors at any color, and the elevation angle of the telescope, suggesting that an atmospheric residual must be sub-dominant to the main correlated signal.

5.5 Calibration Drifts

Variations in bolometer loading (due to changing sky emission, for example) and bolometer base plate temperature cause changes in bolometer responsivities. To characterize and correct for these changes, a calibration lamp (cal-lamp) is located in the optics box at

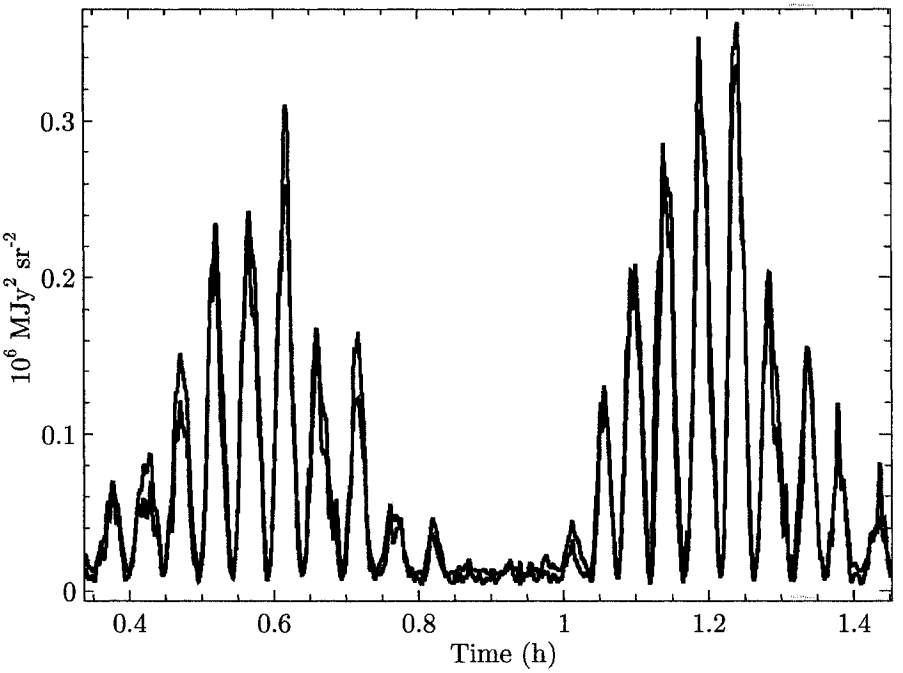

Figure 5.7: Plot of $\tilde{d}^2(t)$ (red) and $K\ \tilde{d}(t)\,\tilde{H}(t)$ (blue) from Equation 5.15, showing the tight correlation between the detectors (a 250 μm color in this case) and the telescope altitude in a band from 40 mHz to 1 Hz.

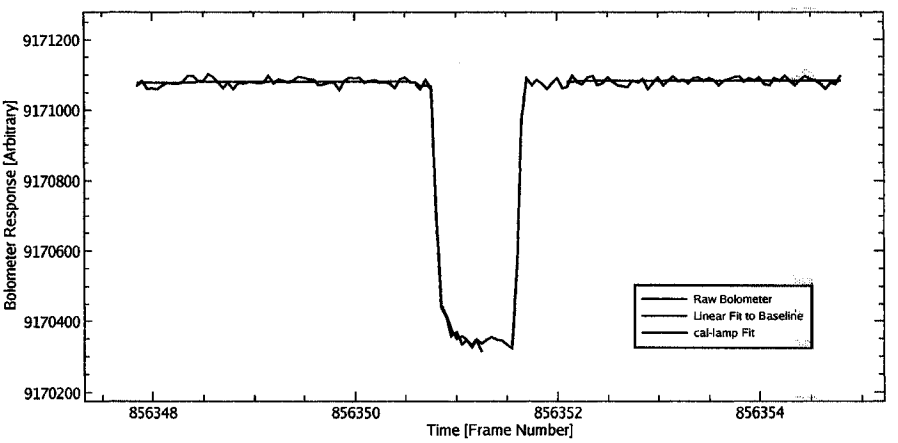

Figure 5.8: An example of a single cal-lamp pulse on a bolometer time stream. The linear fit is to data 550 ms before and after the pulse, to remove the baseline. The cal-lamp is fit to a template of a pulse from an arbitrarily chosen cal-lamp bolometer pulse..

the center of the reflective Lyot stop allowing for the measurement of these changes. The cal-lamp is pulsed once every 10–15 minutes during flight (see Figure 5.8). The cal-lamp is designed to provide a stable signal over the flight, so any change in cal-lamp ampli-

tude as measured in a bolometer is directly proportional to a change in that bolometer's responsivity. The signal baseline is removed by fitting a line to a 550 ms chunk of data before and after the cal-lamp pulse. A template cal-lamp profile from a raw bolometer time stream is fit to every cal-lamp pulse in every bolometer. The amplitude of the fit is interpolated over time and inverted to generate a multiplicative scaling cal-lamp time stream for each bolometer. Fluctuations in the responsivity are less than 8% RMS, dominated by diurnal variations due to differences in atmospheric loading and thermal emission from the telescope changing temperatures. On time scales of a typical source map, the fluctuations are less than 2% RMS. A constant responsivity time stream for each bolometer is generated by applying the multiplicative scaling cal-lamp time stream. The large scale fluctuations are suppressed and the final responsivity variations are less than 2% RMS.

5.6 Point Source Flux Extraction

To calculate the flux from a point source, we adopted a matched-filtering technique similar to that used to extract point sources from several recent extra-galactic submillimeter surveys (e.g. [55, 56]). A point spread function (PSF) is generated by stacking and averaging several point sources from various maps in telescope coordinates. We area normalize the PSF, P, such that

$$\sum_{x,y} P(x,y)\delta x \delta y = 1, \tag{5.18}$$

where the double sum is over all pixels in the PSF map, and δx and δy are the angular dimensions of a pixel. The units of P are therefore sr^{-1}. In all BLAST maps, square pixels are used so that $\delta x = \delta y$. BLAST maps are calibrated in surface brightness units [Jy sr^{-1}]. A map of a point source, $M(x,y)$, can be modeled by the normalized PSF

centered over the source, scaled by its flux density, S, or $SP(x,y) \approx M(x,y)$. If each pixel in M has an uncertainty σ, then we can write χ^2 for the model:

$$\chi^2 = \sum_{x,y} \frac{(SP(x,y) - M(x,y))^2}{\sigma^2(x,y)}. \tag{5.19}$$

Minimizing this χ^2 results in the maximum likelihood flux,

$$S = \frac{\sum_{x,y}(M(x,y)P(x,y)/\sigma^2(x,y))}{\sum_{x,y}(P(x,y)/\sigma(x,y))^2}. \tag{5.20}$$

This technique gives a low statistical uncertainty because we have intrinsically high signal-to-noise data and also because knowledge of the beam shape is used to weigh the uncertainties; however, errors in the PSF will bias the result. To check for a bias we used simple aperture photometry as a second measure of flux densities for some of the detected sources. The difference between the matched filter and aperture photometry fluxes was less than 3%. Since the matched filter provides significantly smaller statistical errors, it is used to extract fluxes from all point-like sources.

5.7 Flat Fielding

The bolometers in each array are flat-fielded so that meaningful multi-bolometer maps can be generated. The flat-field corrections are determined using individual maps made for each bolometer from a single point-source calibrator. The scans were designed such that a fully sampled map can be generated from each bolometer individually. For each bolometer, the total flux from the point source is measured and a flat-fielding coefficient for each bolometer is then calculated as the ratio of the flux from that bolometer and the flux from an arbitrarily chosen reference bolometer. All subsequent maps are generated from time streams that apply the flat-fielding coefficient appropriately to each bolometer.

5.7.1 Absolute Flux Calibration

BLAST calibrates using point sources. Arp 220 and CRL2688 were the two primary calibrators observed during the Kiruna flight. The Arp 220 Spectral Energy Distribution (SED) is better known than that of CRL2688. Therefore we have decided to use Arp 220 to calculate the responsivity in band. Details can be found in [57].

In order to predict the band-averaged flux in the BLAST bandpasses for Arp 220, a single temperature modified blackbody spectral energy density (SED) of the form $S_\nu = A\nu^\beta B_\nu(T)$ was first fit to existing submillimeter and FIR observations. Here, S_ν has units of Jansky[2], A is the amplitude, β is the emissivity, and $B_\nu(T)$ is the Planck function for a blackbody with temperature T. Submillimeter photometry was available from the single pixel bolometer UKT14 instrument on the JCMT at 350–1100 μm [58], SCUBA at both 450 μm [59] and 850 μm [60, 59, 61], and finally at 350 μm from SHARC-II[3]. The quoted errors for these measurements are typically $\sim 10\%$, excluding absolute calibration uncertainties. Two groups published ISOPHOT, measurements, at 60–200 μm [62] and at 120–200 μm [63]. In each case the dominant uncertainty is the absolute calibration of ISOPHOT which is estimated to be $\sim$30%. However, more precise photometry at 60 and 100 μm is available from the RBGS. Since the quoted errors are extremely small ($\sim 0.1\%$), we adopt an additional 10% error to account for other calibration uncertainties. For reference, the difference between the RBGS and the original Bright Galaxy Samples ranges from 5–25%. Finally, in addition to the measurement errors quoted by all of these groups, we have assumed an additional *correlated* 5% error for all of the photometry, since the bulk of these instruments were calibrated using the same Uranus SED which is known to have an uncertainty of $\sim$5% [64].

The smooth SED is fit to the data using χ^2 minimization. In this procedure the correlated

[2]A Jansky (symbol Jy) is a non-SI unit of electromagnetic flux equivalent to $10^{-26}\,\mathrm{W\,m^{-2}Hz^{-1}}$

[3]http://www.submm.caltech.edu/ sharc/analysis/calibration.htm

5% error is ignored, since it does not affect the position of the minimum in the parameter space. For all of the ISOPHOT measurements given by a single group, the 30% calibration uncertainty is considered to be 100% correlated and down-weighs the measurements in the calculation of χ^2. Similarly, 10% correlated errors are adopted for all measurements reported by a single group for the other instruments. To characterize the range of models that are consistent with the data, 1000 Monte Carlo simulations of the photometry are performed in which both the independent and correlated errors are considered. The SED is re-fit to each of these simulated data sets. The data and envelope of model fits are shown in Figure 5.9. The band-averaged flux densities for each BLAST wavelength are obtained for each SED model fit as

$$S_{\rm B} = \int T(\nu)S(\nu)d\nu, \tag{5.21}$$

where the normalized filter transmission profiles $T(\nu)$ are measured using a Fourier transform spectrometry (see Section 4.2). From these 1000 sets of band-averaged fluxes, we obtain estimates of variances of the calibrator brightnesses in each band, $\langle\sigma_i^2\rangle$, as well as the correlated error between the fluxes in each band, $\langle\sigma_i\sigma_j\rangle$.

Maximum-likelihood estimates for the fluxes of sources are obtained from Equation 5.20 using un-calibrated maps of Arp 220 in units of Volts. Multiple visits throughout the flight allow us to estimate systematic gain variations not traced by the internal cal-lamp pulses at the 3% level. Since this uncertainty is significantly lower than the calibrator flux uncertainty as estimated above, we calculate single calibration coefficients c_i in each band for the entire flight, as the ratio of the band-averaged fluxes to the raw fluxes from our maps. Including all of these sources of uncertainty, the final absolute percentage errors and a Pearson correlation matrix showing the relationship between errors in the different bands are given in Table 5.1.

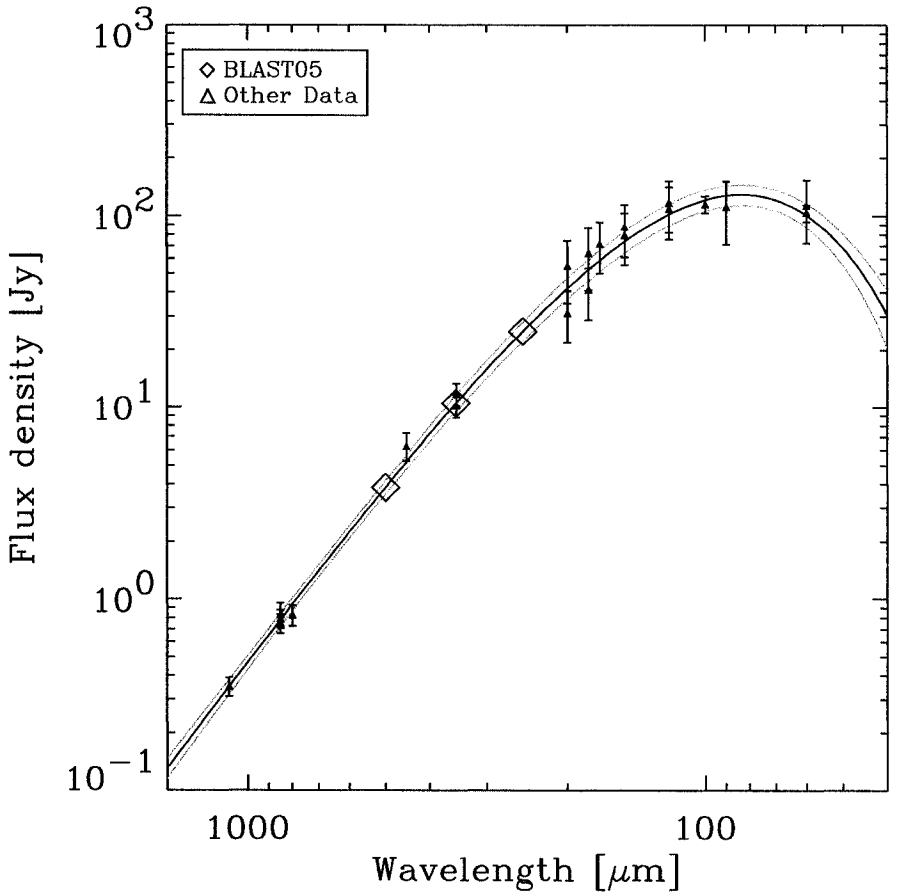

Figure 5.9: Spectral Energy Distribution (SED) plot of Arp 220, the absolute flux calibrator for BLAST05. The model was fit to data from a range of telescopes (blue triangles). Black diamonds indicate the model predictions at 250, 350 and 500 μm. The uncertainties associated with these predictions are 12%, 10%, and 8% in each band respectively.

Band	calib. coeff.	uncertainty	Pearson correlation matrix		
μm	[$\times 10^{12}$ Jy V^{-1}]	[%]	250 μm	350 μm	500 μm
250	7.61	12	1	0.97	0.87
350	3.16	10		1	0.96
500	1.56	8			1

Table 5.1: Calibration coefficients, calibration uncertainty, and Pearson correlation matrix showing the relationship between errors in different bands for BLAST05.

5.8 BLAST Simulator

In a Monte Carlo approach to the description of the data, several simulated realizations of a measurement have to be generated. One, or more than one, part of the flight has to be simulated. We wrote code that generates simulated time streams that mimic the noise and the signal of the real measurement.

An input signal map is used as a realization of the observed sky. To simulate the blurring effect of the telescope beam , the map can be convolved with a Gaussian of a given FWHM. The map can also be convolved with the real, measured beam that can be different for each detector. Rotational asymmetries of the beams are taken into account rotating the beam maps by the rotation angle given in the pointing solution. The convolved map is then scanned with the pointing solution to generate a signal-only time stream.

A random realization of noise is generated for each detector from the noise PSD, corrected for the correlated signal, as described in Section 5.4.

A random realization of the main component of the correlated signal is also generated and added to the noise time stream after being multiplied by an appropriate amplitude coefficient also described in Section 5.4.

This noise and the signal time streams are saved. They can later be added together to generate a signal plus noise time stream.

One obvious missing feature in the current implementation is the scan synchronous noise. This is of little relevance for extragalactic point sources, which were the driving reason for the simulator. It will be of relevance for observations of diffuse structures. We plan to add the feature as soon as the analysis will require it.

Simulator Performance

We used all the scans obtained on the ELAIS-N1 extragalactic field to validate the simulator. We will use the same field to quantify the instrument performances later in this chapter. This region has very low astrophysical signal, with a signal-to-noise less than unity in each time stream sample.

Fifty realizations of the telescope measurement have been generated and binned into naive maps. For each map, a pixel histogram have been generated after cropping the map with a mask to control edge effects. The mask is chosen to cut regions of uneven sampling, and, for the purpose of this test, it is chosen by eye.

The average pixel histogram, with error bars indicating the dispersion among the simulations, is shown in Figure 5.10. The same histogram is calculated for the map obtained from the flight data and it is also shown in the Figure.

The distributions are in very good statistical agreement, as indicated by reduced χ^2 close to unity.

Pixel-Pixel Covariance

A naive map maker whiten the noise, filtering away all the 1/f components. These are the major source of correlation in the time stream. In principle, there could be other sources of correlated noise that can project into the map correlations among pixels.

To address the problem we evaluated the pixel-pixel noise covariance matrix that might be of some relevance for point sources, i.e. a matrix of 8x8, 10" pixels. The matrix has been computed from the same simulated maps described in the previous section as the autocorrelation function.

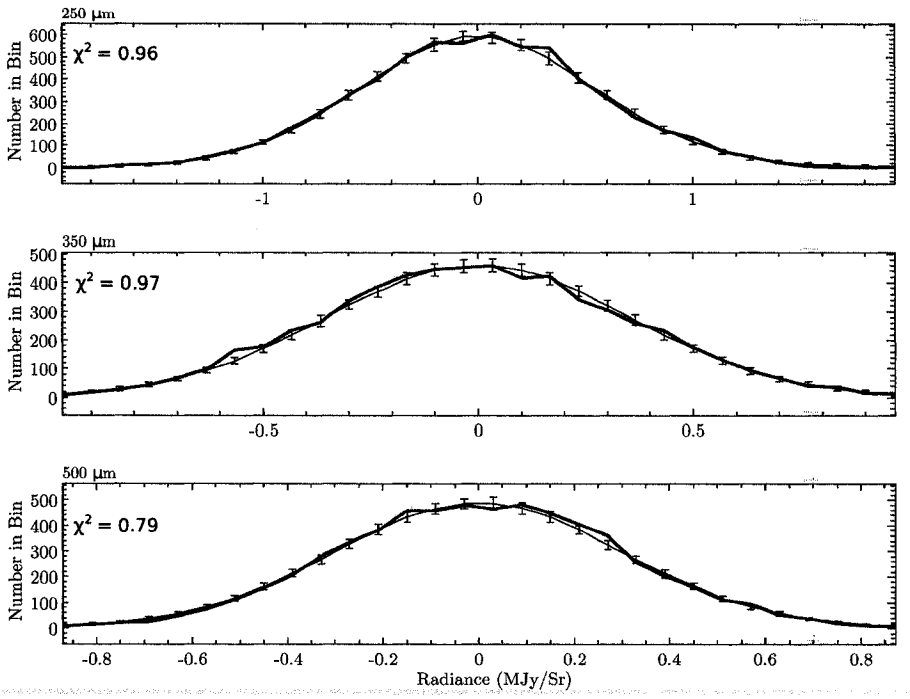

Figure 5.10: The Simulator is tested on one extragalactic field. The different panels refer to the three BLAST colors, from 250 μm to 500 μm. The pixel histograms are computed for i) 50 realization of the noise maps (blue histogram with error bars indicating the dispersion) and ii) for the the map acquired in flight (red histogram). The reduced χ^2 are computed, and are shown in the panels, indicating very good agreement between the model and the measurement.

The result in Figure5.11 shows negligible correlations of less that 1.5%.

5.9 Detector Performance

We use the same simulations to quantify the performance of the detectors achieved in flight. Calibrated naive maps are convolved with a matched filter: a two-dimensional Gaussian with nominal FWHM of 30″, 42″, and 60″ at 250 μm, 350 μm, and 500 μm, respectively.

$$S_{ij} = \frac{\sum_{lm} P_{lm} M_{i-l,j-m} \sigma^{-2}_{i-l,j-m}}{\sum_{lm} P^2_{lm} \sigma^{-2}_{i-l,j-m}} \tag{5.22}$$

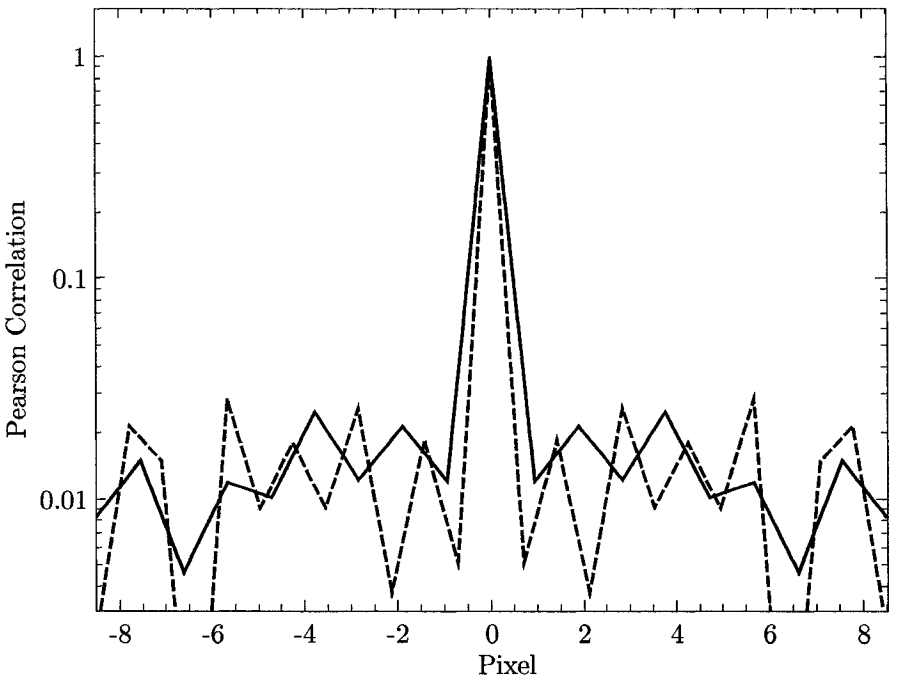

Figure 5.11: Pearson pixel-pixel covariance matrix of the naive map maker. The solid and dashed lines are the X and Y cross-sections of the matrix, respectively. Correlations are negligible at about 1%. 10" pixels were used in the map.

Here P_{lm} is the beam model of Equation 5.18, M_{lm} is the map (calibrated in surface brightness), and σ_{lm} is the pixel noise. S_{ij} is the maximum likelihood flux in the pixel ij. Following Equation 5.20, each pixel of the convolved map has now units of flux per beam.

Assuming uncorrelated, white noise, the pixel variance can be written as $\sigma_{ij}^2 = \sigma^2/h_ij$, where h_{ij} is the number of samples in the pixel ij, and σ is the noise associated with each sample. Therefore

$$S_{ij} = \frac{\sum_{lm} P_{lm} M_{i-l,j-m}\, h_{i-l,j-m}}{\sum_{lm} P_{lm}^2\, h_{i-l,j-m}}. \tag{5.23}$$

The distribution of the pixels values S_{ij} is Gaussian (see Figure 5.12), with variance

$$Var(S_{ij}) = \frac{\sigma^2}{\sum_{lm} P_{lm}^2 h_{i-l,j-m}} = \sigma^2 f_{ij}. \tag{5.24}$$

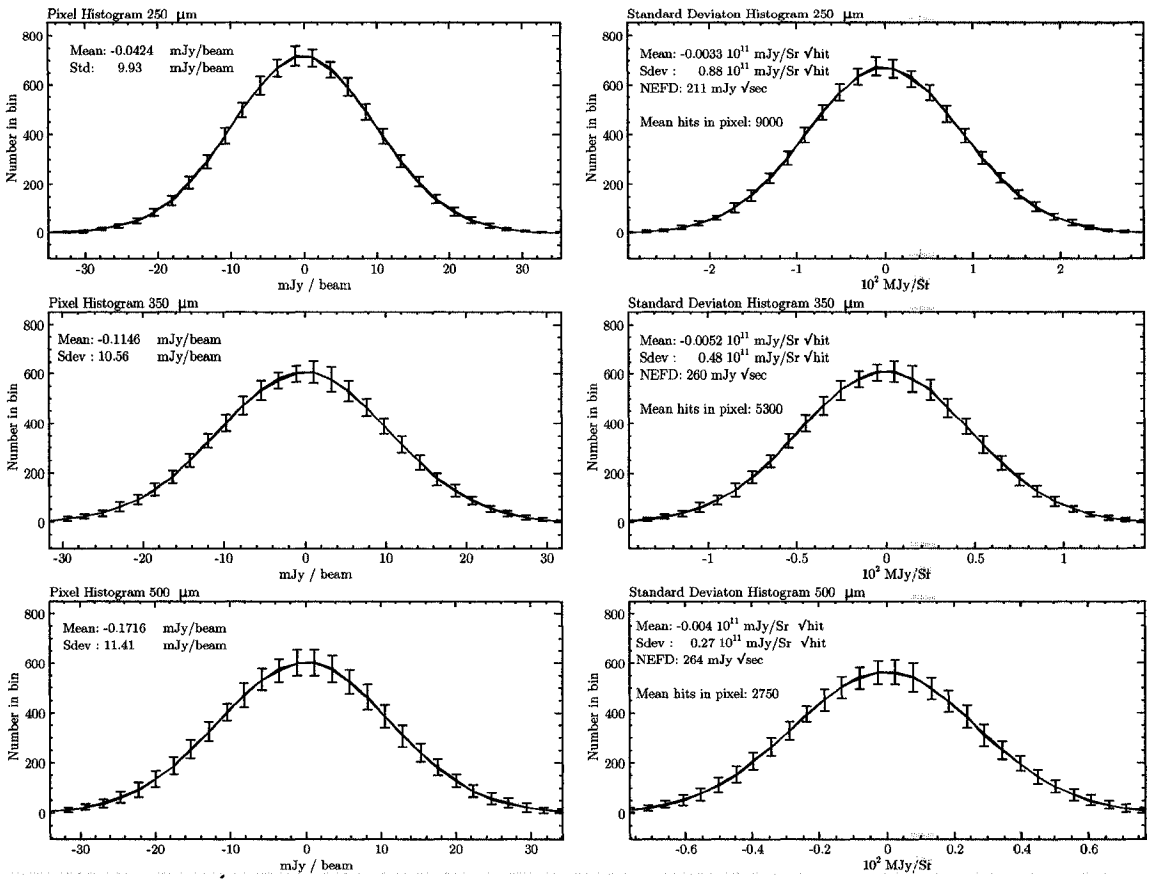

Figure 5.12: Pixel histograms from simulated maps at the three BLAST colors are used to measure the noise performances of the Kiruna flight. Left panels: pixel histograms of convolved maps (Equation 5.22); the width of the distribution is a measure of the depth reached in this field. Right panels: pixel histograms of the map after being divided by the f_{ij} described in Section 5.9. The width of the distribution is the noise in each detector sample. An equivalent NEFD is calculated assuming nominal beams of 60″ at 500 μm.

To evaluate the sample noise σ, note that the new quantity S_{ij}/f_{ij} is Gaussian distributed with variance σ^2. Therefore σ can be estimated from an histogram of the match filtered map, where each pixel has been divided by f_{ij}.

Figure 5.12 shows values of σ, expressed as Noise Equivalent Flux Density (NEFD) in mJy $\sqrt{\text{s}}$, of about 250 mJy $\sqrt{\text{s}}$.

These NEFD values are the same to the one proposed, and show that BLAST, with nominal beam sizes, does have the sensitivity to perform as advertised.

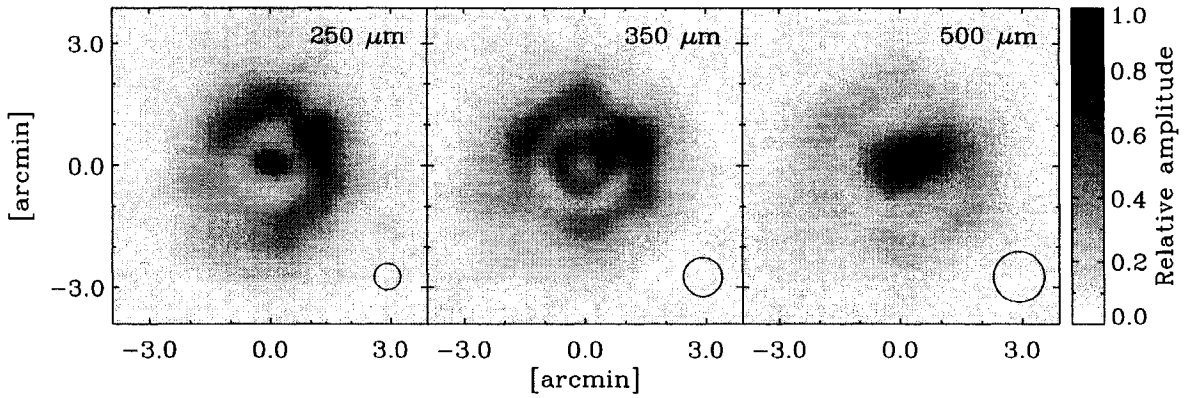

Figure 5.13: Point Spread Functions (PSFs) for each of the three BLAST wavebands from BLAST05, generated by stacking several point source maps in telescope coordinates. The little circle (bottom-left of each panel) has the size of the nominal PSF. The PSFs are significantly more extended than expected, reducing sensitivity to point sources and the ability to distinguish crowded sources amidst fluctuating cirrus.

5.10 BLAST05 Warm Optics Performance and Overall Sensitivities

During the 2005 Sweden flight, the warm optics (primary and secondary mirrors) did not perform within the specifications. The telescope beams at the three colors are shown in Figure 5.13. They were obtained from maps of several point sources that were observed during the flight. These single maps have then been stacked together after being renormalized to the same amplitude, and weighed with the renormalized noise.

Noting that the central structure in each is on a scale comparable to the diffraction limit, the beams are clearly far from ideal, distributing considerable power into an outer ring (hexagon) of diameter $\sim 200''$. Since these shapes are not well described by a FWHM value, we use the projected solid angle expressed as $\Omega = \alpha^2$ with $\alpha = 180''$, $183''$ and $155''$, from $250\,\mu$m to $500\,\mu$m, to be compared to the designed values of $30''$, $43''$ and $60''$. Clearly some sort of mechanical failure is present. We have analyzed the problem using optical design software. We investigated the effect of out-of-focus, out-of-

alignment optics, where we allowed all the optical elements to be shifted and tilted from their nominal position, but we were not able to re-produce the effect at a satisfactory level in all the colors. Structural damages are among other possibilities considered. The light rain the payload suffered before take-off, could have damaged the carbon fiber primary causing the panels to delaminate (carbon-fiber gets particularly weak in high humidity environment). The launch itself has been particularly violent, causing the failure of the inner frame locking mechanism that broke loose. The Inner Frame violently ran into both hardware stops. This event could have damaged the telescope, including the secondary support mechanism and the primary itself.

The effect of these larger beams has been a reduced sensitivity to point sources. As shown in the previous section, and in Figure 5.12, the in-flight measured noise is 8.8, 4.8 and $2.7\,\mathrm{MJy\,sr^{-1}}\sqrt{s}$, at $250\,\mu$m, $350\,\mu$m, and $500\,\mu$m, respectively. This translate into NEFD's of about $200{\sim}260\,\mathrm{mJy}\sqrt{s}$ if a nominal beam is assumed. Since these values of NEFD are the one BLAST was designed for, sensitivity to resolved structures was unaffected by the size of the beams, and suffered only from a reduced overall resolution.

The actual NEFD is calculated using the projected solid angles, measured from the beam maps in Figure 5.13. These are 6.3, 3.8 and $1.5\,\mathrm{Jy}\sqrt{s}$ at $250\,\mu$m, $350\,\mu$m, and $500\,\mu$m, respectively: a reduced sensitivity toward point sources as big as 25 times, at $250\,\mu$m.

5.11 BLAST06 Warm Optics Performance

The in-flight failure of the warm optics during the Kiruna campaign led us to design a mirror refocusing mechanism. The hardware implementation is mentioned in Section 2.1.1, and it is reviewed in detail in Appendix B. It allows for axial displacements of the secondary, relative to the primary.

The reasons that drove us to develop the system were:

- due to water absorption, it is impossible to observe in the far-field of the telescope from the ground, therefore it is difficult to ensure the telescope is in-focus at launch;
- the focus of the telescope is sensitive to the position of the secondary mirror relative to the primary within $\sim \lambda/2$. It is very hard to reach this accuracy without an optical test, and in-flight temperature variations of the mirror surfaces are large enough to bring the system out of focus.

During the McMurdo flight we scanned the telescope over point sources to correct the position of the mirror. We had to adjust our estimated location of the secondary by $350\,\mu$m. Had we not had this device would have resulted in serious optical degradation of our $350\,\mu$m and $250\,\mu$m beams.

At the time of writing, the analysis of the BLAST06 data set has just begun. Nonetheless, a very preliminary pointing solution was attempted, with an estimated accuracy of about $20''$. A naive map of a point source at $500\,\mu$m revealed a beam of nominal shape and size: Gaussian with $60''$ FWHM.

The cross section of the $500\,\mu$m beam is shown in Figure 5.14. We have no reason to expect that the detector noise would be any different from the Kiruna campaign. In fact, a preliminary analysis has shown the same levels of 1/f and white noise, or better. Therefore, we expect BLAST to have nominal sensitivity to point sources and to diffuse structures, as well as nominal angular resolution, allowing for the science goals outlined in this thesis and in the proposal to be achieved.

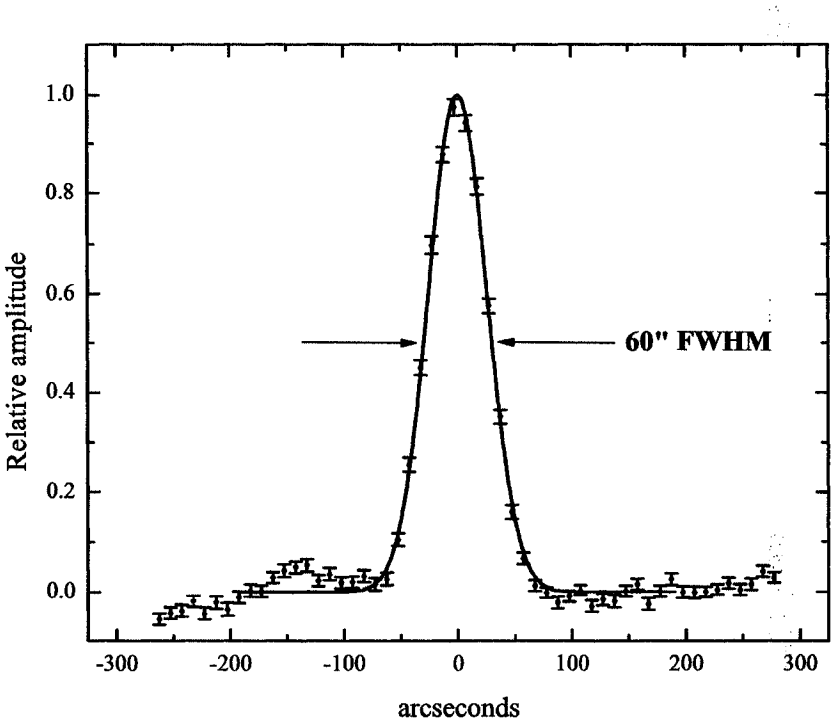

Figure 5.14: Point spread function cross section for the 500 μm beam from BLAST06. the points are the pixel values in the map from which the cross section has been extracted. Error bars are the 1σ pixel noise. A Gaussian fit to the pixels is shown in red. The FWHM of the fit indicates a nominal beam size at this wavelength.

Chapter 6

Conclusions and Future Work

We have built and flown a balloon-borne submillimeter observatory, designed to study the star-formation in our Galaxy and in high redshift starburst galaxies by exploiting a window at several hundred microns which is not useable from the ground.

Over the course of two successful science flights, BLAST has addressed a broad range of Galactic and extragalactic topics.

The small beams, the large-format detector arrays, and the wavebands exploited make BLAST one of the most challenging experiments for which new technologies and experimental techniques have been developed.

In this work I have reviewed the whole experiment, and discussed each section in some detail. Some sub-sections have been explained in depth, as for the discussion about the optical system. I have shown how critical the alignment of the primary telescope is for point source sensitivity. The implementation of a refocussing system has allowed us to achieve this goal.

I have shown how to design and operate a day-time star tracker, and how to use fiber

optic gyroscopes to achieve pointing reconstruction of the line-of-sight to better than 5" RMS. I also have outlined a way to increase such accuracy to better than 3" RMS by combining the redundant sensors available on BLAST.

A new data reduction pipe-line has been implemented to convert the raw time streams into calibrated maps. The pipe-line deals with all sorts of pathologies in the data, and in particular with the highly correlated channels in each detector array.

Finally the performance of the instrument in the two science campaigns of Kiruna, Sweden (2005), and McMurdo, Antarctica (2006) was discussed. BLAST performed as proposed in the first science flight, but a problem in the warm optics resulted in a loss of sensitivity toward point sources. The issue was addressed and fixed for the second campaign where the payload met all the design goals.

Both flights have been scientific successes. As a result of the Kiruna data-set, three papers are currently in preparation, and four more have already been submitted to journals: Pascale et al. (2007) describes the instrument; Patanchon et al. (2007) reviews one of the map makers written for BLAST; Chapin et al. (2007) discusses the Vulpecula star forming region; Truch et al. (2007) makes available the measured flux of several Galactic and extragalactic compact sources.

The analysis of the McMurdo data-set has just started at the time of writing, and it is my intention to continue to be involved in the analysis of both data-sets.

The success of BLAST has been large enough that other payloads are implementing some of the subsystems we have developed, and part of my experimental work will be in following these efforts.

Appendix A

Analysis of the Interferogram

I would like to review here a method to analyze the interferometric measurements obtained in Section 4.2. There has been some confusion about this topic, and I am writing these notes with the hope they can be useful to the future operators of our FTS.

A Michelson Interferometer measures an *interferogram* that is related to the intensity spectral distribution through

$$I(z) = \int_{-\infty}^{\infty} S(\sigma) \cos(2\pi\sigma z) d\sigma \tag{A.1}$$

where z is the position of the moving mirror and $S(\sigma)$ is the spectral distribution of the radiation intensity as a function of the wavenumber σ. For an ideal instrument, the interferogram is symmetric ($I(z) = I(-z)$) and z ranges from $-\infty$ to $+\infty$. The center of symmetry at $z = 0$ is where all the frequencies add in phase in the FTS: this happens when the optical paths are the same in both arms of the FTS and it is called the Zero Path Difference (ZPD) position. The object of the measurement is to estimate the $S(\sigma)$

through the Fourier transform of the interferogram

$$S(\sigma) = F[I(z)] = \int_{-\infty}^{\infty} I(z) e^{-2\pi i \sigma z} dz. \tag{A.2}$$

Here, in the ideal case of a perfectly symmetry interferogram, $S(\sigma)$ is purely real.

In a real FTS, $I(z)$ is sampled at equally spaced intervals from $-z_1 < 0 < z_{\max}$. This is equivalent to multiplying $I(z)$ by the window function $A(z)$ that is 1 for z inside the interval $-z_1 < 0 < z_{\max}$ and 0 every where else. It is useful to express $A(z)$ as the sum of symmetric and antisymmetric function

$$A(z) = A^+(z) + A^-(z) \tag{A.3}$$

$$A^+(z) = \frac{1}{2}[A(z) + A(-z)] \tag{A.4}$$

$$A^-(z) = \frac{1}{2}[A(z) - A(-z)] \tag{A.5}$$

Therefore the transform of the sampled interferogram is

$$\begin{aligned} \hat{S}(\sigma) &= F[A(z)\, I(z)] \\ &= F[A^+(z)\, I(z)] + F[A^-(z)\, I(z)] \\ &= a^+(\sigma) \star S(\sigma) + a^-(\sigma) \star S(\sigma) \end{aligned} \tag{A.6}$$

where the $a^{\pm}(\sigma)$ are the Fourier transform of the $A^{\pm}(\sigma)$. a^+ is called the "instrumental transfer function" and contributes to the real part of $\hat{S}(\sigma)$; $a^-(\sigma)$ contributes to the imaginary part of $\hat{S}(\sigma)$ only. Figure A.1 plots these functions where it is clear that $A^+(z)$ weighs the part of the interferogram between $-z_1$ and z_1 twice with respect to the other portions outside this interval. Therefore it is necessary to properly deweight $I(z)$

apodizing it with the function

$$\begin{aligned} A_1(z) &= 0 \quad &\rightarrow \quad z < -z_1 \\ A_1(z) &= \frac{1}{2}\frac{z+z_1}{z_1} \quad &\rightarrow \quad -z_1 < z < z_1 \\ A_1(z) &= 1 \quad &\rightarrow \quad z > z_1 \end{aligned} \tag{A.7}$$

The respective symmetric and antisymmetric functions, $A_1^+(z)$ and $A_1^-(z)$, are plotted in figure A.1. The measured spectrum, whose interferogram is sampled on the asymmetric interval $z_1 < z < z_{\max}$, is

$$\tilde{S}(\sigma) = F[A_1^+(z)\, I(z)] = \Re\{F[A_1(z)\, I(z)]\}. \tag{A.8}$$

A.1 Phase Correction

Here we have assumed $I(z)$ is to be sampled on a grid so that $I(z = 0)$ is at the ZPD point. Usually the interferogram is not sampled at $z = 0$. This is referred to as a phase error and in its simplest case is due to the fact that the sampling electronics might miss the ZPD point. If β is the spatial distance between the ZPD pint and the closest sampled point, then

$$\int_{-\infty}^{\infty} I(z+\beta) e^{-2\pi i \sigma z} dz = e^{2\pi i \sigma \beta} S(\sigma). \tag{A.9}$$

This has the effect of rotating the real spectrum into the imaginary plane. In order to correct this phase error, the coefficient β can be evaluated from a small, symmetric portion of the interferogram around the ZPD point. The complex Fourier transform of this section, the low-resolution spectrum ($S^b(\sigma)$), gives an estimate of the linear phase as

$$2\pi\,\beta\,\sigma = \frac{\Im[S^b(\sigma)]}{\Re[S^b(\sigma)]}. \tag{A.10}$$

The coefficient β is then evaluated through a weighed least square fit of this equation with a line of null intercept. The weights to use are the amplitudes of the low resolution spectrum squared to make sure that only the points laying inside the optical filter band are used. Once β has been estimated, the interferogram needs to be apodized by Equation A.7 modified to take into account this phase error:

$$\begin{aligned} A_1(z) &= 0 && \rightarrow && z < -z_1 \\ A_1(z) &= \frac{1}{2}\frac{z+z_1}{z_1+\beta} && \rightarrow && -z_1 < z < z_1 + 2\beta \\ A_1(z) &= 1 && \rightarrow && z > z_1 + 2\beta \end{aligned} \tag{A.11}$$

The new expression for $A_1(z)$ now gives the correct weight to the symmetric part of the interferogram, taking care of the real ZPD position.

After transforming $A_1(z)\, I(z)$, the phase correction can be applied to get the measured spectrum. From Equations A.8 and A.9 we get

$$\tilde{S}(\sigma) = \Re\{e^{-2\pi i\sigma\beta} F[A_1(z)\, I(z)]\}. \tag{A.12}$$

The low-resolution phase obtained can, in principle, be interpolated and divided off from Equation A.8 directly. This can be done if there is a known reason for which the phase could be a function of σ more complicated than a line, but slow varying. In practice a non-linear phase suggests some systematic error in the measurements that need further investigation.

A.2 Calibration

A Martin-Puplett interferometer measures the difference of two input sources:

$$\tilde{S}(\sigma) = R(\sigma) \times [BB(T_1, \sigma) - BB(T_2, \sigma)] \tag{A.13}$$

where $BB(T, \sigma)$ is a black body at some temperature T.

The input black bodies in our case are liquid nitrogen at 77 K and Eccosorb[1] at 300 K. They both lie in the Raleigh-Jeans part of the spectrum at the BLAST frequencies. It is then sufficient to divide $\hat{S}(\sigma)$ by the σ^2 Rayleigh-Jeans law and normalize the resulting shape to 1 to get the filter responses $R(\sigma)$.

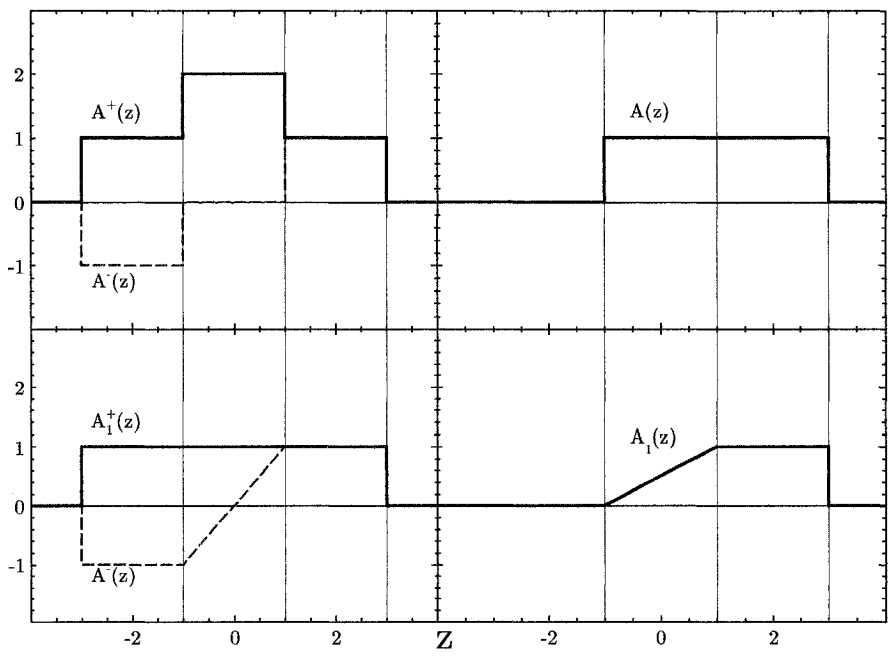

Figure A.1: Window functions for (top panel) the FTS sampling in the interval $-z_1 = 1$, $z_{\max} = 3$. The bottom panel shows the correction functions to apply to the interferogram.

[1] http://www.eccosorb.com/

Appendix B

The Balloon-borne Large Aperture Submillimeter Telescope: BLAST

E. Pascale,[1] P. A. R. Ade,[2] J. J. Bock,[3,4] E. L. Chapin,[5] J. Chung,[1,5] M. J. Devlin,[6] S Dicker,[6] M. Griffin,[2] J. O. Gundersen,[7] M. Halpern,[5] P. C. Hargrave,[2] D. H. Hughes,[12] J. Klein,[6] C. J. MacTavish,[1] G. Marsden,[5] P. G. Martin,[8,14] T. G. Martin,[1] P. Mauskopf,[2] C. B. Netterfield,[1,14] L. Olmi,[9,10] G. Patanchon,[5,13] M. Rex,[6] D. Scott,[5] C. Semisch,[6] N. Thomas,[7] M. D. P. Truch,[11] C. Tucker,[2] G. S. Tucker,[11] M. P. Viero,[14] D. V. Wiebe[1]

ABSTRACT

The Balloon-borne Large Aperture Submillimeter Telescope (BLAST) is a sub-orbital survey-experiment designed to study the evolutionary history and processes of star formation in local galaxies (including the Milky Way) and galaxies at cosmological distances. The BLAST continuum camera, which consists of 270 detectors distributed between 3 arrays, observes simultaneously in broad-band (30%) spectral-windows at 250 μm, 350 μm and 500 μm. The optical design is based on a 2 m diameter Cassegrain telescope, providing a diffraction-limited resolution of 30″ at 250 μm. The gondola pointing system enables raster-like maps of arbitrary geometry, with a repeatable positional accuracy of $\sim$ 30″; post-flight pointing reconstruction to $\lesssim$ 5″ rms is also achieved. The on-board telescope control software permits autonomous execution of a pre-selected set of maps, with the option of manual intervention. In this paper we describe the primary characteristics and measured in-flight performance of BLAST. Since a test-flight in 2003, BLAST has made two scientifically productive long-duration balloon flights: a 100-hour flight from ESRANGE (Kiruna), Sweden to Victoria Island, northern Canada in June 2005, and a 250-hour, circumpolar-flight from McMurdo Station, Antarctica, in December 2006.

Subject headings: submillimeter — galaxies: evolution — stars: formation — instrumentation: miscellaneous — balloons

[1]Department of Physics, University of Toronto, 60 St. George Street, Toronto, ON M5S 1A7, Canada; enzo@physics.utoronto.ca

[2]Department of Physics & Astronomy, Cardiff University, 5 The Parade, Cardiff, CF24 3AA, UK

[3]Jet Propulsion Laboratory, Pasadena, CA 91109-8099

[4]Observational Cosmology, MS 59-33, California Institute of Technology, Pasadena, CA 91125

[5]Department of Physics & Astronomy, University of British Columbia, 6224 Agricultural Road, Vancouver, BC V6T 1Z1, Canada

[6]Department of Physics and Astronomy, University of Pennsylvania, 209 South 33rd Street, Philadelphia, PA 19104

[7]Department of Physics, University of Miami, 1320 Campo Sano Drive, Carol Gables, FL 33146

[8]Canadian Institute for Theoretical Astrophysics, University of Toronto, 60 St. George Street, Toronto, ON M5S 3H8, Canada

[9]Istituto di Radioastronomia, Largo E. Fermi 5, I-50125, Firenze, Italy

[10]University of Puerto Rico, Rio Piedras Campus, Physics Dept., Box 23343, UPR station, San Juan, Puerto Rico

[11]Department of Physics, Brown University, 182 Hope Street, Providence, RI 02912

[12]Instituto Nacional de Astroffsica Óptica y Electrónica (INAOE), Aptdo. Postal 51 y 72000 Puebla, Mexico

[13]Laboratoire APC, 10, rue Alice Domon et Léonie Du-

1. Introduction

We have built and flown a balloon borne submillimeter observatory, designed to study the star formation in our Galaxy and in high redshift starburst galaxies by exploiting a window at several hundred microns which is not useable from the ground.

The Balloon-borne, Large Aperture, Submillimeter Telescope (BLAST) is a stratospheric balloon–borne 2 m telescope which observes the sky with bolometric detectors operating in three bands at 250 μm, 350 μm, and 500 μm. The diffraction-limited optics are designed to provide BLAST with a resolution of 30″, 42″, and 60″, respectively. The detectors and cold optics are adapted from those to be used on the SPIRE instrument on *Herschel* (Griffin et al. 2003). By providing the first sensitive large-area ($\sim 0.8-200$ deg^2) submillimeter surveys at these wavelengths, BLAST addresses important Galactic and cosmological questions regarding the formation and evolution of stars, galaxies and clusters (Devlin et al. 2004).

Taking advantage of the unique spectral-coverage, resolution and sensitivity, the primary scientific goals of BLAST are to i) conduct confusion-limited and shallower wide-area extragalactic surveys to constrain the redshift-distribution, star formation history and evolution of optically-obscured luminous galaxies, by measuring robust photometric-redshifts (derived from the BLAST colors, and complementary data, Hughes et al. 2002), and the spatial clustering of this population; ii) to improve our understanding of the earliest stages of star formation by determining the physical properties and mass-function of cold pre-stellar cores, and the efficiency of star formation within different Galactic environments; and iii) to investigate the nature and structure of the interstellar medium by making high resolution maps of diffuse Galactic emission.

BLAST had a 24 hours test flight (BLAST03) from Fort Sumner, NM, in September 2003, which demonstrated the performance of the instrument sub-systems.

BLAST made its first science flight (BLAST05) in June of 2005, flying on a 1.1×10^6 m^3 balloon from the Swedish Space Corporation base of ESRANGE, near Kiruna, Sweden to Victoria Island in northern Canada. During this 4.5 day flight at an average altitude of 38 km, the instrument performed well, except for degraded optical performance. This was possibly due to a failure of structural elements in the carbon fiber mirror, and resulted in decreased resolution, which had a significant impact on our ability to achieve our extragalactic science goals. BLAST acquired 100 hours of data on Galactic targets, providing some of the first arcminute resolution images at these wavelengths. In this flight, surveys were conducted of five star forming regions, including the well-studied Cygnus-X field, three regions of intermediate/high-velocity cirrus, the Cas-A supernova remnant, and several individual bright targets.

BLAST made its second science flight (BLAST06) in December, 2006, flying from the Williams Field Long Duration Balloon (LDB) facility near McMurdo Station in Antarctica. In this flight the instrument met its performance goals in resolution, sensitivity, and pointing. The flight was terminated after 250 hours of data were acquired. Unfortunately, an anomaly with the parachute separation system prevented the parachute from being released from the gondola after landing. The parachute dragged BLAST for 250 km before it came to rest in a crevasse field on the Antarctic Plateau. While most of the instrument was destroyed, the hard drives containing the data were found nearby, and the complete dataset recovered. In this flight, BLAST conducted shallow (10 deg^2) and deep, confusion-limited (0.8 deg^2) extragalactic surveys of the CDF-S as well as a 10 deg^2 region near the south ecliptic pole. A Galactic survey in Vela mapped 52 deg^2 and 200 deg^2 of sky in deep and shallow observations, respectively. Surveys of several Galactic and extragalactic selected targets were also conducted.

A brief overview of BLAST science, in the context of current and future Far Infrared (FIR) and submillimetric experiments, is given in Section 2. The telescope and optics are described in Section 3, while Sections 4 and 5 focus on detector arrays and cryogenics. Sections 6 to 8 provide detailed information regarding the gondola, com-

quet 75205 Paris, France

[14]Department of Astronomy & Astrophysics, University of Toronto, 50 St. George Street, Toronto, ON M5S 3H4, Canada

mand and control, and pointing systems. Sections 9 to 12 provide overviews of the unique thermal and power requirements, and a description of the pointing performance.

2. BLAST in the context of other FIR-submillimetre experiments

The BLAST bands bracket the peak of the thermal radiation emitted by dust at temperatures of around 10 K. Assuming that the temperature range of dust in submillimeter galaxies is $\sim$ 30 – 60 K, BLAST can explore redshifts from 1 to 5 (Hughes et al. 2002). The primary advantage of BLAST over existing submillimeter bolometer arrays such as SCUBA and SHARC is its greatly enhanced sensitivity at wavelengths $\leq 500\,\mu$m, due to the dramatically increased atmospheric transmission at balloon altitudes. With proposed sensitivities of 250 mJy s$^{1/2}$, the BLAST mapping speed is 10 times faster than the design goal for SCUBA 2 at 500 μm (Holland et al. 2006), and more than 100 times the mapping speed of the pioneering flights of the FIR balloon-borne telescope PRONAOS (Lamarre et al. 1998). BLAST is complemented at shorter wavelengths by surveys from *IRAS*, *ISO*, *Spitzer*, *Akari*, and at longer wavelengths by SCUBA 2, LMT, and ALMA, to constrain spectral energy distributions. *Spitzer*'s higher resolution also provides accurate astrometry for many of the BLAST sources. BLAST complements the *Herschel* satellite by testing detectors and filters which are similar to those to be used in the SPIRE instrument (Griffin et al. 2003). Furthermore, the results from BLAST will be available early enough to influence the design (depth and area) of future SPIRE surveys. In addition, BLAST will complement the large-area spectroscopic Galactic surveys of *SWAS*, provide submillimeter targets for the Fabry-Perot spectrograph SAFIRE on *SOFIA*, and impact the design of the scientific case for the next generation of submillimeter surveys from space (e.g. *SPICA* and *SAFIR*, and later *SPIRIT* and *SPECS*).

3. Telescope

The basic BLAST optical configuration is shown in Figure 1. Incoming radiation is collected by a Cassegrain telescope (M1 and M2 in the figure) which is located on the inner frame of the gondola (described in Section 6), along with the cryogenic receiver (Section 5). The Cassegrain focus is located about 20 cm behind the optical surface of the primary. Cold (1.5 K) re-imaging optics (M3, M4, and M5) in the receiver relay the sky image to the detector focal planes. A baffled Lyot stop (M4) is located at the position of an image of the primary mirror. This blocks stray radiation due to scattering and diffraction. After M5 the radiation is divided into three spectral bands through the use of two low-pass edge dichroic filters (Ade et al. 2006). An aperture at the center of the Lyot stop is made to match the one at the center of the primary mirror to reduce loading. This same hole accommodates a commandable thermal source, which provides a stable and repeatable optical signal (calibration lamp) to monitor detector responsivity drifts (Hargrave et al. 2006). The optical design is optimized to deliver a diffraction-limited image of the sky at the detector focal planes, with 60″ and 30″ beams at 500 μm and 250 μm, respectively. The telescope design of BLAST05 and BLAST06 is discussed later in this section and the relevant parameters can be found in Table 1.

3.1. Focal Plane

The illumination of the Lyot stop and the main reflector depends primarily on the properties of the feed-horns in the detector array. BLAST uses $2f\lambda$ spaced, smooth-walled conical feeds which are similar to SPIRE feeds. Their design and measured characteristics have been described by Chattopadhyay et al. (2003), Rownd et al. (2003), and Griffin et al. (2002). The optical system design is based upon the feed-horn nominal $f/5$ focal ratio and requires the chief-rays to be perpendicular to the aperture of the horn, with all the beams overlapping at the Lyot stop. Knowledge of the fundamental propagated electromagnetic mode (TE_{11}) is used in a Zemax[1] Physical Optics module to verify the final design.

3.2. BLAST05 Optical Design

For the 2005 flight, the design incorporated a 2 m carbon-fiber spherical primary mirror with a mass of 32 kg and a surface rms of 2.4 μm. It was

[1] http://www.zemax.com/

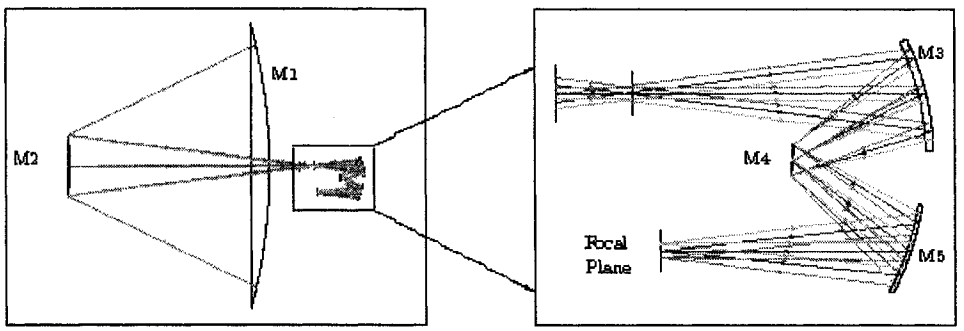

Fig. 1.— The optical layout of the BLAST05 telescope and receiver is shown on the left and the 1.5K optics which are located within a cryostat are shown expanded on the right. The image of the sky formed at the input aperture is re-imaged onto the bolometer detector array at the focal plane. The mirror M4 serves as a Lyot stop defining the illumination of the primary mirror for each element of the bolometer array. The three wavelength bands are defined by a pair of dichroic beamsplitters (not shown) which are located between M5 and the focal plane.

designed and built by Composite Optics Incorporated[2] as a technology prototype for the 3.5 m *Herschel* telescope. An aluminum correcting secondary mirror, with a diameter of 50 cm, gave diffraction-limited performance over a $14' \times 7'$ field of view (FOV) at the Cassegrain focus. The estimated antenna efficiency was $\geq 80\%$; losses came from a combination of the rms surface roughness of the primary and the quality of the re-imaging optics. Two of the re-imaging cold elements, M3 and M5, are ellipsoidal mirrors; M2 and the other cold element, M4, compensate for most of the spherical aberration of the primary, whereas M3 and M5 contribute to achieve the correct focal ratio. The perimeter of the primary mirror was structurally weak, forcing M2 to be suspended by a carbon-fiber structure, attached through the hole in the primary mirror. This geometry resulted in $\sim$ 12% blockage of the beam, leading to significant projected loading on the detectors for all three bands. Although various optical solutions for ground visible/IR telescopes using a spherical primary are discussed in the literature, in our case, peculiar design constraints had to be respected (mainly weight and size). A full discussion can be found in Olmi (2001, 2002), where the optimization procedure and the basic optical configuration are also discussed. The 2 m primary mirror was under-illuminated by setting the entrance pupil diameter to 188 cm, and the reflector was strongly tapered, resulting in a field taper of about -15 dB. A Strehl ratio > 0.96 was achieved over the whole focal plane, and far field beams had a first sidelobe at -10 dB. A detailed analysis of the relation between Strehl ratio and aperture efficiency, which is more commonly quoted for filled-aperture antennas, can be found in Olmi (2007).

3.3. BLAST06 Optical Design

In the 2006 Antarctic flight, BLAST flew a Ritchey-Chrétien telescope, with a 1.8 m diameter, aluminum primary mirror with a mass of 114 kg. Originally, the mirror was intended to be used only for the test flight in 2003. However, after the destruction of the carbon fiber mirror on landing of BLAST05, the aluminum mirror was re-machined to improve the quality of the surface from 8 μm to better than 4 μm rms. This machining was performed by the Precision Engineering Group at Lawrence Livermore National Laboratory. A 40 cm diameter aluminum secondary was suspended by four carbon fiber struts[3] (with a zero linear thermal expansion coefficient) attached to the perimeter of the primary mirror, which reduced the obscuration to $\sim$ 7%. The loading on the detectors was reduced further with the instal-

[2]Composite Optics Incorporated (COI), 9617 Distribution Avenue, San Diego, CA 92121.

[3]Innovative Composite Engineering, 139 E. Columbia River Way, Bingen, WA 98605.

lation of angled reflecting baffles under each strut to deflect most of the obscured beam to the relatively cold sky. The cold re-imaging optics form an ideal Offner relay. In this configuration, M3, M4, and M5 are all spherical and share a common center of curvature; M3 and M5 are concave while M4 is convex. In order to achieve a diffraction-limited beam of 60″ at 500 μm and 30″ at 250 μm with a smaller diameter primary compared to BLAST05, M1 was more aggressively illuminated. This was made possible by reducing the diameter of the Lyot stop by about 12%, leading to a field taper of -7.5 dB on M1 and -17 dB sidelobes in the far field beams.

3.4. BLAST06 Focussing System

The relative distance between the primary and the secondary mirrors has a tolerance of one λ before significant image degradation is introduced. Thermal modeling indicated that diurnal temperature fluctuations at balloon altitudes of the aluminum M1 and M2 mirrors could have been as large as 10°C. The required correction in the relative distance between M1 and M2 was calculated to be 50 μm/°C.

To correct for this, we implemented a motorized system for in-flight refocussing of the secondary. M2 was coupled to its mounting structure via 17-7PH stainless steel leaf springs. Three stepper motor actuators[4] (2.12 mm rev^{-1} lead screw) drive the mirror back and forth to correct for the focus position, as well as adding tip/tilt capability to initially align M2 to M1. Accurate positioning was achieved with differential optical encoders ($\simeq$1 count μm^{-1} resolution) factory mounted to the motors, and three DC Linear Variable Differential Transformers[5] (LVDT). This system allowed for $\pm$5 mm of motion about the nominal telescope focus, which was sufficient for accurate positioning. The flight computer commands each motor individually by communicating with the stepper motor controllers over a RS485 bus.

Pre-flight focussing of the system was hampered by the fact that water vapor absorption makes ground-based submillimeter observations in the far-field of the telescope (about 10 km) impossible. To mitigate this, the secondary mirror was physically offset to 3 positions so that the focal plane was reimaged at 50, 100, and 150 m from the telescope. The focussing system was then used to fine-tune the focus at each position. These results were extrapolated to determine the far-field focus for the flight.

In flight, the focus of the system was verified and had to be manually adjusted by maximizing the response when scanning over bright point sources: a correction of 300 μm to the position set at launch was found required. Subsequently, the temperatures of the primary and secondary were monitored and the secondary automatically repositioned to account for thermal variations that would produce a focus displacement of 100 μm or more. In flight, the primary and secondary mirror diurnal temperature fluctuations were $\pm$1.5°C for most of the flight.

3.5. Array Bandpass Characteristics

Low-pass edge dichroic filters (Ade et al. 2006) split the incoming radiation emerging from M5. The first dichroic reflects wavelengths shorter than 300 μm and transmits longer wavelengths. The bandpass for the 250 μm array is further defined by a filter directly in front of the array, which reflects wavelengths shorter than 215 μm, and by the waveguide cutoff at the exit of each of the feedhorns. For the 350 μm array, the band is defined at the short wavelength end by the transmission of the first dichroic and at the long wavelength end by the waveguide cutoff. The 500 μm band is defined at the short wavelength end by the transmitted radiation from the second dichroic and at the long wavelength end by the feedhorn cutoff. Each band has a 30% width. The filter stack frequency performance was evaluated with Fourier Transform Spectroscopy. Bandpasses are shown in Figure 2.

4. Receiver

The BLAST focal plane consists of arrays of 149, 88, and 43 detectors at 250 μm, 350 μm, and 500 μm, respectively. The arrays are cooled to a temperature of 300 mK. Each array element is a silicon nitride micromesh "spider web" bolometer (Bock et al. 1996). The detector arrays, the feeds, and the mounting scheme are based on the SPIRE

[4]Ultra Motion, 22355 Route 48, #21, Cutchogue, NY 11935.
[5]Macro Sensors, 7300 US Route 130 North, Building 22, Pennsauken, NJ 08110, 0.6μm or better repeatability.

instrument design (Turner et al. 2001). Each array hosts a number of diagnostic channels: two dark bolometers (channels that have been capped to avoid illumination), two thermistor, and one resistor. The detector parameters are summarized in Table 2.

Each bolometer consists of a photolithographed mesh that provides high absorption efficiency over a wide frequency range, as well as providing low heat capacity (Turner et al. 2001). An additional advantage to this design is the relatively small cross-section to cosmic rays. Balloon flights at high-latitudes have about 100 times the mid-latitude cosmic ray flux. A Neutron Transmutation Doped (NTD) germanium thermistor glued to the absorber measures the bolometer temperature and therefore the flux of incoming photons.

The detectors and the readout electronics are designed so that the sensitivity is ultimately limited by the photon "BLIP" noise. To achieve this performance, other contributions to the bolometer noise have to be controlled. A bolometer is foundamentally limited by phonon noise in the thermal link with the heat sink. The Noise Equivalent Power (NEP) is in this case $\mathrm{NEP} = \gamma\sqrt{4k_\mathrm{B}T^2G}$, where G is the thermal conductance, T is the bath temperature and γ takes into account the Johnson noise in the thermistor. For a given background load Q, the maximum sensitivity is achieved when $G \sim Q/T$ (Mather 1984). The detectors have been optimized for loads of 55, 40 and 30 pW at 250 μm, 350 μm, and 500 μm, respectively. The detector transfer function is measured using cosmic ray hits, as described in Crill et al. (2003), and we have found typical time constants of ~ 2 ms.

4.1. Readout Electronics

A schematic diagram of the readout electronics is shown in Figure 3. Each bolometer is pre-amplified with a Siliconix U401 differential JFET with 5–7 nV Hz$^{-1/2}$ noise at $\nu > 100$ Hz. Compact 24 channel JFET modules are integrated into the design of the cryostat, allowing us to sink their power dissipation (240 μW per pair) to the vapor-cooled shield (see Section 5) and decrease the load on the helium bath by approximately 60 mW. The JFET are operated at a temperature of $\sim$ 145 K. Their output is then amplified using the Analog AD624 instrumentation amplifier (5 nV Hz$^{-1/2}$) with a 100 Hz wide band-pass filter, centered at 208 Hz. To mitigate the effects of $1/f$ noise, the detectors are AC biased with a sine wave at 200.32 Hz. A reference square wave at this frequency is generated by dividing down the main 32 MHz clock serving the readout electronics, making the bias synchronous with the sampling. This signal is then split into three paths (one per band), stabilized to a voltage amplitude that is selectable from 0 to 300 mV with a resolution of 7 bits, and filtered into a sine wave using low-noise operational amplifiers (Analog OP470). The bias is delivered to the detectors and a reference is sent back to the Data Acquisition System (DAS) where a digital lock-in is implemented on the DSP (Analog ADSP21062) in the readout electronics. The bolometric AC signals and the bias reference are digitized with a 24 bit $\Sigma\Delta$ (Burr-Brown ADS1252) fed by a low-noise dual instrumental amplifier (Burr-Brown INA2128) and sampled at 10 kHz. The reference is phase-locked and a numerical sine wave is generated in-phase at the bias frequency (the clock is shared). The rectified signal is then low-passes with a 4 stage boxcar filter having a first null at 50.08 Hz, and decimated to match the DAS sampling frequency (100.16 Hz).

The resulting flat-phase filter is well approximated by a Gaussian and is computationally efficient in the time domain, allowing up to 25 independent channels to be locked-in on a single DSP. Only the real part of the signal is sampled, hence the relative phase between signal and reference must be manually set. Since the phase difference is a function of the bolometer impedance, it needs to be adjusted in flight along with bias levels. This is achieved by maximizing the signal from the pulsed calibration lamp at the Lyot stop.

The overall data acquisition electronics noise is kept below the estimated photon noise and provides stability to low frequencies (< 30 mHz), which allows the sky to be observed in a slowly-scanned mode.

4.2. Detector Noise

The voltage noise is determined by taking the power spectral density of a deglitched time stream acquired in flight. The electronic time constant is then deconvolved and common-mode signals are removed as described by Patanchon et al. (2007).

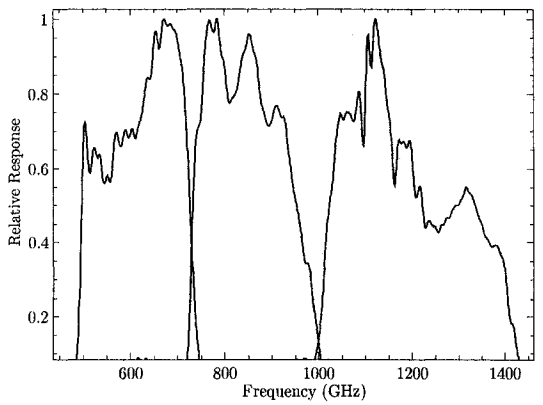

Fig. 2.— Relative spectral response of the three BLAST channels for a flat-spectrum source, measured during the BLAST06 campaign. The peak response in each band has been normalized to one. Absorption from residual water vapor inside the Fourier transform spectrometer is visible in all the bands.

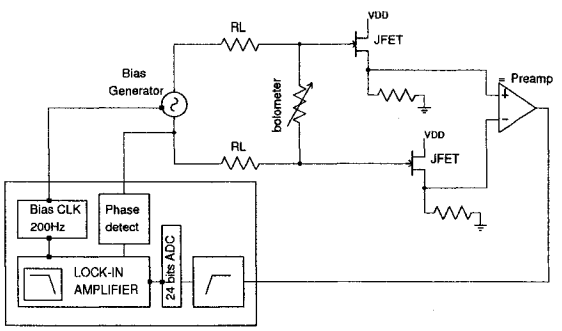

Fig. 3.— A schematic diagram of the detector readout electronics. A 200.32 Hz sine wave biases each bolometer across two 7 MΩ load resistors. JFET pairs buffer the detector signal to the warm electronics. The two signals are then differenced and digitized. A digital lock-in rectifies and filters the output sending it to the flight computers over the BLASTbus.

The final average noise is plotted in Figure 4 as a function of frequency for a representative detector.

5. Cryogenics

The cryostat houses most of the receiver system (Figure 5) and was fabricated by Precision Cryogenics[6]. It is constructed of aluminum, for its strength to weight ratio, and G10 woven fiberglass reinforced resin epoxy when minimal thermal conduction is required. The cryostat is maintained at vacuum to prevent thermal convection, and each thermal stage fully encloses the next colder stage to reduce radiative thermal loading, except for the optical path, which is thermally protected with infrared blocking filters. Super-insulation, consisting of twenty layers of aluminized Mylar, is used to further reduce the emissivity of the aluminum and G10, and therefore the radiative load.

Liquid baths of nitrogen and helium maintain the temperatures of the 77 K and 4.2 K stages. In flight, an absolute pressure regulator[7] is used to maintain approximately 1 atm above each bath. Tests were performed to verify the pressure regulator would not introduce flutter causing vibrations or temperature oscillations. A vapor-cooled shield (VCS) is located between the nitrogen and helium stages. Boil-off gas from the helium bath passes through a heat exchanger in thermal contact with the VCS before venting out of the cryostat. The VCS reduces the thermal loading on the helium stage and therefore increases the hold-time. Simulations of the cryostat with TAK 2000 Lite[8] thermal analysis software were used during the design process to ensure long-duration (> 11 day) hold time with a minimum weight and size. Radiative and conductive loading is 7.2 W on the nitrogen tank and 71 mW on the helium tank. An additional effective load of 9 mW and 7 mW on the helium tank is due to the liquid drawn into the pumped-pot by the capillary (discussed below), and heating required to cycle the ^{3}He refrigerator, respectively. The cryostat holds 43 L of nitrogen and 32 L of helium.

A liquid He pumped-pot maintains the optics

[6]http://www.precisioncryo.com/

[7]Tavco, Inc, 20500 Prairie St., Chatsworth, CA.

[8]http://www.tak2000.com/

box at 1.5 K. A long, thin capillary connects the helium bath to the pumped-pot with a volume of $\sim$ 100 mL. A pump line between the pot and the exterior of the cryostat keeps the pot at near vacuum, maintaining the temperature at 1.5 K. The pressure difference between the helium bath and the pot forces helium into the pot; the length and diameter of the capillary are tuned to provide the minimum amount of helium to keep the pot cold. On the ground, a vacuum pump is used; at float altitude, the pump line is open to the atmosphere, which is at a pressure < 0.01 atm.

The bolometers and feed horns are maintained at < 300 mK by the closed-cycle ^{3}He refrigerator. The ^{3}He is condensed by the 1.5 K pumped-pot, and collects in the ^{3}He cold stage. Once all the ^{3}He has condensed, a charcoal sorption pump lowers the pressure above the ^{3}He, bringing the temperature below 300 mK. When the liquid ^{3}He is exhausted, the charcoal is heated to > 20 K, and the ^{3}He is released to be condensed by the pumped-pot and the cycle repeats. During a cycle, the added heat load on the helium tank increases the boil-off and therefore further cools the VCS. The ^{3}He refrigerator is able to extract 5 J of energy, and needs to be recycled every 48–60 hours. Each cycle takes less than 2.5 hours.

The cryostat performed as expected during both science flights. The nitrogen and helium baths maintained constant temperature, and the VCS fluctuated by less than 3 K due to the ^{3}He refrigerator cycles. The pumped-pot maintained a temperature below 1.8 K with fluctuations less than 10 mK. During ^{3}He refrigerator cycles the pumped-pot temperature rose as high as 2.5 K. The bolometer temperature was maintained below 300 mK with less than 1 mK fluctuations on hour time scales. The first science flight was too short to test hold time. In the second 12.5 day flight, the helium tank was exhausted 11.5 days after reaching float altitude. The nitrogen tank was not exhausted before termination.

6. Gondola

The BLAST gondola provides a pointed platform for the telescope and the attachment point to the balloon flight train. The gondola was designed and built by AMEC Dynamic Structures[9], based on initial designs from members of the BLAST team. Schematics of the gondola are shown in Figures 6 and 7. The breakdown of the mass of various components is given in Table 3.

6.1. Requirements

The gondola design is driven by the stringent pointing requirements of the science-case. The elevation range of the inner frame, including the 2 m primary mirror and the $\sim$ 200 kg cryostat, is $25 - 60°$. The entire gondola can rotate to any azimuth angle. The in-flight pointing is accurate to $\sim 30''$ and post-flight pointing reconstruction is accurate to better than $5''$. The telescope's primary observing mode is to scan in azimuth at $\sim 0.1° \, s^{-1}$. Finally, the mirrors are shaded from solar radiation.

As a consequence of the pointing requirements, the feedback rate of the control system is $\sim$ 10 Hz. To accommodate this, the gondola is designed to be rigid, with a minimum resonance frequency greater than 14.4 Hz. All mechanical tolerances are set to minimize backlash. All bearings are low friction and low stiction with low-temperature grease. The center-of-mass of the system is on the rotational axis so that translations of the gondola (by wind or from the balloon) do not generate torques which re-orient the telescope.

A target weight of $\sim$ 2000 kg was set for the entire system. The maximum width and height of the gondola are constrained by the geometry of the buildings in the field where the gondola is assembled. The launch procedure requires that, in the launch orientation, no part of the gondola intersects a plane 20° from vertical passing through the launch vehicle/gondola attachment point. A final constraint on geometry is that all components of the gondola must fit into standard sea shipping containers. Additionally, the gondola must survive the vibrations and shocks suffered during launch and there must be no structural failure during any of the possible load cases under parachute shock, that can be as high as 10 g along the vertical. Finally, the mechanical tolerances must account for temperatures which vary by as much as ~ 100 °C during the course of the flight.

[9] http://www.amecds.com/

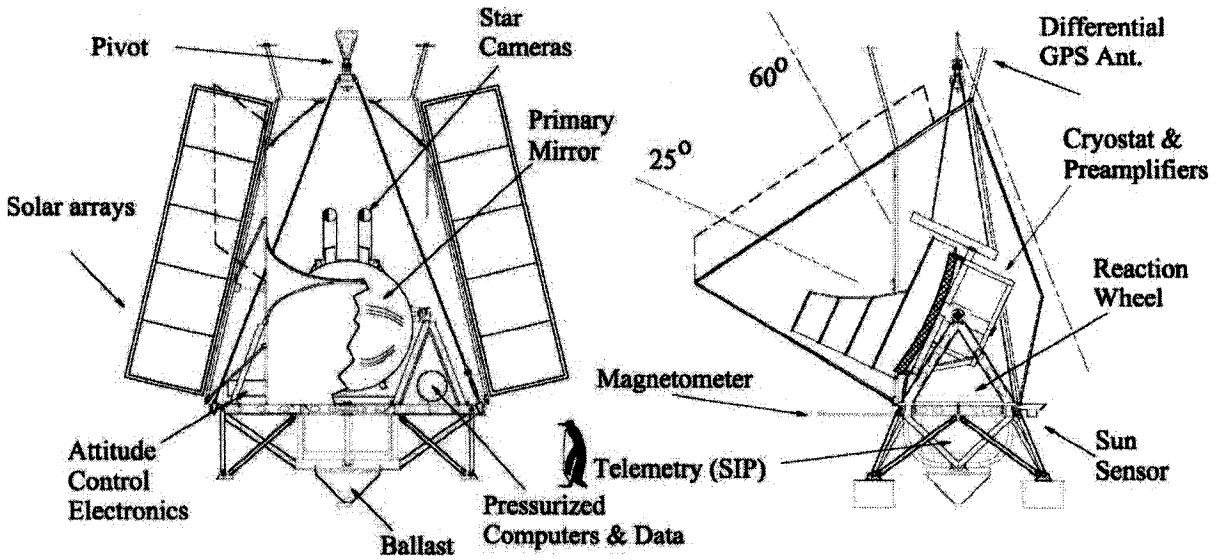

Fig. 6.— Front and side schematic drawings of the BLAST gondola. A 1 m tall Emperor penguin is shown for scale. The height of the pivot is set by the size of the launch vehicle and the width of the gondola *without* deploying the solar panel arrays matches the width of the laboratory doors. The inner frame, which can be pointed in elevation, consists of the two star cameras, the telescope and its light baffle, the receiver cryostat and associated electronics. The telescope baffle shown at right, which was used in 2005, was replaced by a smaller system in 2006. The CSBF solar panels and transmitting antennae are suspended below the structure shown here. The lines marked 25° and 60° show the useful range of orientation of the optic axis. The dot-dashed line at the right originating above the pivot shows a 20° avoidance zone required to avoid accidental contact at launch. The dashed parallelogram at the top in the right hand diagram, and to the left in the left hand diagram shows the shape of an extension to the sun shields added for the Antarctic flight to allow observations to be made further from the anti-sun direction.

6.2. Layout

The gondola frame consists of three components: an outer frame, suspended from the balloon flight train by cables and a pivot motor; an inner frame which is attached to the outer frame at two points along a horizontal axis; and a set of Sun shields that attach to the outer frame. The frame is mostly constructed of light-weight aluminum tubing and I-beams. BLAST incorporates large-diameter torque motors for all motion control.

6.2.1. Major Components

The outer frame consists of a horizontal surface, 2 yokes to support the inner frame, and four legs. The outer frame is pointed in azimuth using a reaction wheel and pivot. It also provides mounts for various electronics boxes, including the flight computers, the Columbia Scientific Balloon Facility (CSBF) electronics, various pointing sensors, and flight batteries.

The inner frame is made from thin-wall aluminum box beam. It supports the telescope, cryostat, detector read-out electronics, gyroscopes and star cameras. It is attached to the outer frame at two points, defining an axis of rotation.

The back, sides and bottom of the gondola are surrounded by Sun shields, allowing the telescope to point as low as 25° in elevation. A lightweight aluminum frame encloses the telescope and is covered with extruded polystyrene panels wrapped in aluminized Mylar. The original design shielded the secondary mirror from the Sun at 30° above the horizon, the highest the Sun rises during an Antarctic flight, with the telescope pointing directly away from the Sun. Additional panels were added for the BLAST06 flight to improve the shading when the telescope is not pointed anti-Sun. The telescope is also protected from solar radiation scattered from the ground. As well as the opening for the telescope, there are forward-facing openings in the Sun shields to allow for cooling of the electronics by radiation (see Figure 7).

6.2.2. Attitude Control

The telescope's attitude is controlled by three torque motors: the reaction wheel, pivot and elevation motors. The motors are rare-earth, permanent-magnet, direct-drive DC torque motors[10] with a peak torque of 13.6 Nm. They are controlled by 50 A pulse-width modulated servo amplifiers.[11] The housings, made of hardened steel, are custom designed and incorporate the bearings. The original design called for a dry Teflon bearing lubricant, but we found that low-temperature bearing grease[12] provides lower friction and stiction.

The telescope is controlled in azimuth by a 1.5 m reaction wheel, made of 7.6 cm thick aluminum honeycomb, and forty-eight, 0.9 kg brass disks mounted around the perimeter to maximize the ratio of moment of inertia to mass. The reaction wheel is mounted on the outer frame, at the center of the platform, with its rotation axis going through the pivot. Torquing the gondola against the reaction wheel controls azimuth pointing.

The gondola is subject to external torque from wind shear acting on the gondola and from balloon rotation acting through the flight train. The second term is minimized, but not entirely eliminated, by installing a vertical axis pivot at the attachment of the gondola to the flight train. See Figure 6. Torque motors can not run at high rotational speeds, and the reaction wheel motor might saturate while trying to overcome these torques, so an additional torque motor placed in the pivot is used to reduce excess angular momentum and keep the rotation of the reaction wheel within reasonable limits. Figure 8 demonstrates that this nested servo system, where the reaction wheel is driven to maintain telescope orientation and the pivot is driven to maintain low reaction wheel speed, successfully decouples the telescope from external torques.

The elevation of the inner frame is controlled by a motor mounted on one side of the inner frame, at the attachment point to the outer frame. A free bearing provides the connection point on the other side. The motor housing incorporates a 16-bit shaft encoder[13] which measures the orientation of the inner frame relative to the outer frame. A fluid transfer system, consisting of a pump and two tanks containing $\sim$ 10 L of a high-density non-

[10] Koll Morgen QT-6205.

[11] Advanced Motion Controls, model 12A8K.

[12] Dow Corning Molykote ® 33.

[13] Gurley Precision Instruments A25SB.

toxic fluid[14], corrects for long time-scale balance offsets induced by the boil-off of the cryogens.

The balloon environment introduces small oscillations in pitch and roll of the gondola. A roll damping system consisting of a motor and a small 30 cm diameter reaction wheel is mounted perpendicular to the flywheel on the outer frame. Oscillations in pitch are removed by controlling the elevation of the inner frame.

7. Command and Control

The BLAST observatory is designed to operate autonomously, without need of ground commanding. Telescope control is provided by a pair of redundant flight computers with Intel Celeron processors at 366 and 850 MHz, running Slackware[15] Linux 9.2 with 2.6.8 Kernel. The computers are kept at near atmospheric pressure to allow the hard drives to function properly, and to provide the appropriate thermal environment for the CPUs.

7.1. Telemetry

The communication link between the telescope and the ground is provided by CSBF through a number of line-of-sight (LOS) transmitters and satellite links. The LOS data-link is available while the payload is in line-of-sight of a receiving station, usually the first part of the flight; satellite link is available for the whole duration of the flight. On board, the interface between the flight computer and telemetry is provided by CSBF's Support Instrumentation Package (SIP). The ground station computers interface with CSBF's ground station equipment to send commands to the payload and display down-linked data. The ground station software uses kst[16] and other Linux applications developed by BLAST team members.

7.2. Gondola Electronics

The flight computers are built upon a passive PCI-bus backplane and contain a single board computer, a four port 8250 serial port extender card, and a custom made PCI controller card, which interfaces major components as well as the LOS data transmitter. This card interfaces with the BLASTbus, a proprietary RS485 bus with three differential pairs (data, clock, strobe). The BLASTbus protocol is a poll and response architecture composed of a 32-bit request followed by a 32-bit response containing 16 bits of data. The BLASTbus clock runs at 4 MHz, giving an effective bandwidth on the BLASTbus of 1 Mbit/s.

The BLASTbus connects the flight computers to the Attitude Control System (ACS) and DAS. Each DSP card in these systems monitors the BLASTbus. They provide data upon request, and receive command input from the flight computers via the BLASTbus.

Data are marshalled on the BLASTbus into 100 Hz frames. Bolometers are polled once per frame, as are the gyroscopes and other high-precision pointing data. The majority of housekeeping signals do not need to be polled at 100 Hz. These "slow data" signals are polled at 5 Hz with groups of twenty multiplexed into a single 100 Hz channel. The 100 Hz frames provide the basic data structure for data archival. The frames are written to disk and transmitted by the line-of-sight 1 Mbit/s transmitter.

In addition to the BLASTbus, the flight computers also collect data via 8250-style serial connections to the differential GPS, the SIP computers, the lock motor, and the secondary actuators. Ethernet provides further connectivity to the star camera computers and Sun sensor computer. Data collected on the auxiliary channels is written back to the BLASTbus in order to synchronize these data with the 100 Hz frame clock. The star cameras are triggered via the BLASTbus to provide data synchronization.

7.3. Flight Software

The flight computers run a single, monolithic program, the "master control program" (mcp), written in C, which performs primary control of all aspects of the telescope including in-flight pointing solution, motion, commanding, telemetry, data archiving, and thermal control.

7.4. Pointing Control

BLAST is a scanning experiment. The primary scan-mode involves an azimuthal raster coupled with a slow elevation drift or discrete elevation

[14] Dynalene HC-40.

[15] http://www.slackware.com/

[16] http://kst.kde.org/

steps.

Detector response times, τ, together with $1/f$ noise, and star camera integration times set limits on the azimuthal scan rate, v_{az}. A Gaussian beam is fully sampled at a rate of $\sim$ 2 / FWHM. The maximum angular rate allowed by the detector τ is therefore

$$v_{az} = \frac{\text{FWHM}/2}{2\pi\tau}$$

or about $0.3^\circ\,s^{-1}$ for the $30''$ beam at $250\,\mu$m, and $\tau \sim 2$ ms. Mid-scan smearing in the star cameras also limits azimuthal scan speeds to about $0.1^\circ\,s^{-1}$. A scan rate larger than this is acceptable only for relatively small scans where star camera solutions at the turn-around are frequent enough. Low frequency ($1/f$) noise sets the largest angular mode that can be constrained to $\sim v_{az}/f_0 \sim 2^\circ$ at $0.1^\circ\,s^{-1}$ (f_0 is the $1/f$ knee at about 50 mHz). Therefore, BLAST scans most of the time at $v_{az} \simeq 0.1^\circ\,s^{-1}$, occasionally going twice as fast on small ($\lesssim 0.3^\circ$ wide) maps. Azimuthal acceleration is limited to $0.1^\circ\,s^{-2}$, resulting in, typically, 2 s for an azimuthal turn-around.

Elevation drift speeds of $10''\,s^{-1}$ or elevation steps of $40''$–$100''$ in adjacent azimuth scans provide adequate spatial sampling of the sky by the detector arrays.

Three primary scan modes are implemented (Figure 9): "cap", a circle centered on a target RA/Dec; "box", a rectangle in azimuth and elevation centered on a target RA/Dec; and "quad", an arbitrary quadrilateral specified by its four corners in RA and Dec.

8. Pointing Sensors

The primary pointing sensors for BLAST are a pair of CCD-based star cameras which provide absolute pointing, and Fiber-Optic rate Gyros that provide velocity information which can be integrated to allow interpolation of the gondola's attitude between star camera solutions. Coarse attitude determination is provided by several additional sensors. In elevation, there is an encoder on the elevation axis, and a tilt sensor on the inner frame. In azimuth, there is a Sun sensor, a differential GPS unit, and a magnetometer. The system provides post-flight pointing reconstruction to $\lesssim 5''$ rms.

8.1. Star Cameras

Four primary factors drove the design of the star cameras: (i) an absolute pointing accuracy of $\sim 5''$ was required to over-sample the diffraction-limited size of the $250\,\mu$m beam; (ii) integration times (and hence efficiency) had to be short enough to avoid significant smearing at the maximum normal scan angular-velocity of the gondola ($0.1^\circ\,s^{-1}$); (iii) the system must *always* detect stars to calibrate gyroscope drift; and (iv) the frequency of the solutions must be high enough to control the $1/f$ random walk noise in the integrated gyroscopes.

To meet these requirements, we incorporated two star cameras for redundancy, and to enable increased positional accuracy in post-flight processing. A detailed description of the cameras can be found in Rex et al. (2006), and a summary of the camera specifications is given in Table 4. Each camera uses a 100 mm Nikon lens with a 200 mm focal length to produce a $2.5^\circ \times 2.0^\circ$ FOV with $7''$ pixels. Each camera is controlled by its own PC/104, 300 MHz Celeron computer which calculates pointing solutions for the gondola at a rate of $\sim$ 1.5 Hz. The computers command the CCD cameras via FireWire, control the focus and aperture size using stepper motors via a serial port, and regulate the temperature of the camera using a small USB DAQ module. The entire system is contained in a pressure vessel to allow the operation of the hard drives, the thermal environment, and to maintain mechanical rigidity. Since the cameras operate during the day, the dominant source of noise is from the sky background, despite the altitude of the experiment. A Nikon R60 red filter is used to attenuate the background. In addition, a 1.2 m long cylindrical baffle is attached to the front of each camera to reduce stray-light contamination beyond 10° from the optical axis.

The pointing algorithm locates blobs in the camera image, rejecting the known bad pixels. The best fit positions of star candidates are then used by a pattern recognition algorithm to identify a unique constellation matching the observed angular separations in a star catalog (Guide Star Catalogue 1.1, see Lasker et al. 1987). The magnitude limit of the catalog is chosen manually and no brightness information for the stars is otherwise used. The algorithm is aided by an approx-

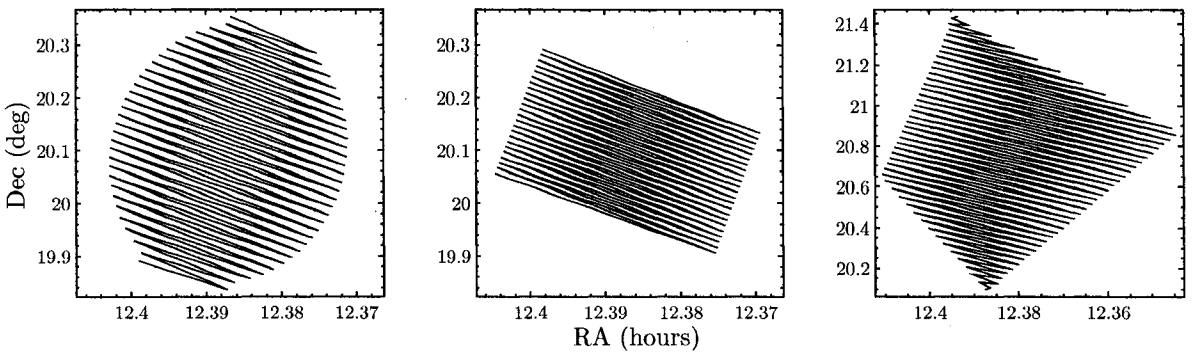

Fig. 9.— Idealized representations of BLAST's three scan modes: from left to right a "cap", a "box", and a "quad". In practice the gyroscopes are used to control the speed and orientation of each single scan, while star camera based orientation solutions at the endpoints are used to prevent gyroscope errors from accumulating.

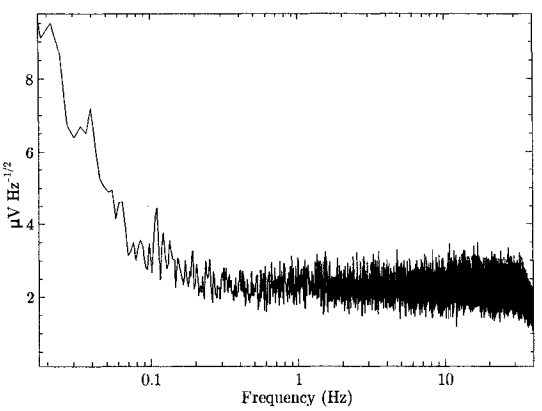

Fig. 4.— A 250 μm detector noise power spectrum density, acquired during the BLAST05 flight with the telescope scanning one extragalactic target. Common modes are corrected as described by Patanchon et al. (2007). The telescope fundamental scan frequency is visible at ~ 0.04 Hz as well as its first odd harmonic at ~ 0.12 Hz. Detectors at different colors have similar performance. The BLAST05 calibration can be found in Truch et al. (2007).

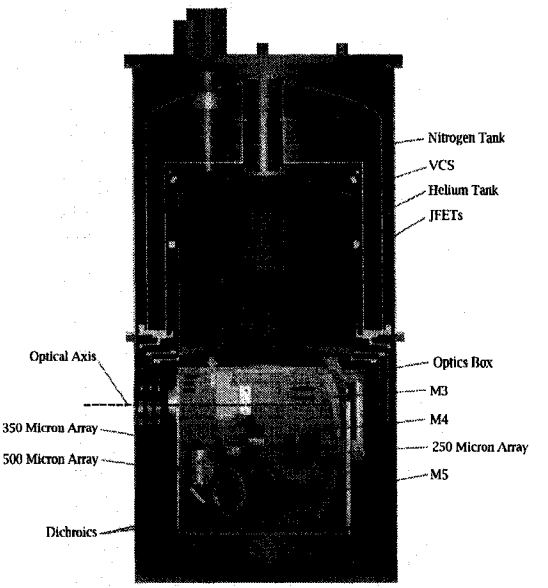

Fig. 5.— Cutaway drawing of the BLAST receiver showing the optics box. The ^{3}He refrigerator is omitted for clarity. The cryostat is held to the telescope structure via bolts in the top flange and jack screws around the perimeter near the base.

imate pointing solution from the flight computer, required to be accurate to $\sim 5°$ (see Section 8.3) to reduce the number of candidate star identifications. A visual magnitude limit of 9 was required to obtain sufficient completeness. A "Lost in Space" algorithm based on the Pyramid technique (Mortari et al. 2001) was also implemented to be used in case the approximate solution was found to be unreliable (which, ultimately, never happened during the BLAST flights).

Once the CCD object centroids are matched to stars with known coordinates (α, δ), the pointing solution is calculated, parameterized by the celestial coordinates of the center pixel, α_0 and δ_0, and the roll of the camera, r. A model in which the image is assumed to be a perfect gnomic tangent-plane projection, with the tangent point at α_0 and δ_0, is used to project each star RA and Dec into the plane of the CCD. The rms distance between the CCD and model star coordinates is then minimized using an iterative Newton solver with respect to the three model parameters. This procedure produced pointing solutions in which the uncertainty in the position of the tangent point was $\sim 3.5''$, and the roll $\sim 200''$. A post-flight comparison of simultaneous pointing solutions from both cameras results in an rms uncertainty of $< 2''$.

8.2. Gyroscopes

Fiber-Optic rate Gyroscopes (FOG) are used to extrapolate the star camera absolute attitude, providing pointing information at each detector's time sample. Two redundant sets of three FOGs are mechanically arranged to measure the gondola angular velocity along orthogonal axes. One of these sets uses ECORE 2000 analogue gyroscopes while the other uses DSP 3000 digital output gyroscopes from the same company[17], with an angle random walk of $5'' \, s^{-1/2}$ and $4'' \, s^{-1/2}$, respectively. Since FOG are sensitive to magnetic fields (Bohm et al. 1982), they were wrapped in a 250 μm thick μ-metal sheet. This reduced the signal induced from the Earth's magnetic field by a factor ~ 10. The gyroscope assembly is temperature controlled to mitigate bias drifts. For BLAST05 both sets worked flawlessly. In BLAST06 two out of the three digital gyroscopes stopped working temporarily, possibly due to a cosmic ray interaction with the gyro electronics. A power cycle of the gyroscope itself restored function. Post-flight attitude reconstruction of the 2005 data, shows that the FOG performed at near their specified sensitivity.

8.3. Coarse Sensors

Two distinct Sun sensors were used on BLAST for coarse azimuth determination. For BLAST03 and BLAST05 a linear CCD behind a thin slit was used. It was replaced by an array of photo-diodes arranged in a azimuthally oriented ring in BLAST06. The photo-diode Sun sensor was designed to be smaller and lighter than the CCD Sun sensor, as well as to consume significantly less power (5 W instead of 50 W).

The photo-diode Sun sensor is a small, all-in-one unit. A PC/104 embedded computer system is mounted below a dodecagonal ring. Twelve photo-diodes are mounted radially around the ring, and the ring is mounted with its axis parallel to the azimuth axis. The intensities of light incident on the photo-diode with the highest intensity and on its 2 nearest-neighbors are compared and fit to a $\cos\theta$ function to determine the azimuth relative to the Sun. The flight computer uses the time and longitude to calculate the azimuth of the Sun, hence recovering the azimuth of the gondola. The CCD Sun sensor, used during the first science flight, had a short-time, relative precision of $2'$, but an overall absolute accuracy of $5°$. The photo-diode Sun sensor, used during the second science flight, had a precision of $4'$, with an absolute accuracy of $5°$. Both units provide azimuthal data at > 5 Hz. In BLAST06, the sun sensor computer crashed several times, possibly due to cosmic ray interactions with the electronics.

BLAST's second coarse azimuth sensor was an ADU5 differential GPS unit[18]. The four required antennae were installed on booms above the Sun shields to minimize multi-path reflections from the gondola (see Figure 6). This orientation was predicted to provide better than $10'$ rms absolute pointing. However, for BLAST05, the GPS stopped providing azimuthal solutions before the instrument reached float altitude and never recovered. For BLAST06, the GPS did not provide solutions until 110 hours after launch. It then began

[17]KVH Industries, Inc.

[18]Magellan Navigation, Inc.

providing solutions and the unit operated with a precision from 0.1° to 0.2° rms. The cause of the irregular reliability of the GPS is uncertain, but may be due to a lack of thermal rigidity in the antenna mounts. The position, altitude, velocity, and time data provided by the GPS unit worked well at all times.

BLAST's third, and most reliable coarse azimuth sensor was a 3-axis, flux-gate magnetometer[19] which was used to determine the gondola's attitude relative to the Earth's magnetic field. The magnetic field orientation was determined using the World Magnetic Model[20]. Even though BLAST passed close to the magnetic pole, the model was accurate enough and the gondola pendulations small enough that the magnetometer-based pointing solution was good to 5° peak to peak in both science flights.

9. Thermal Environment

The LDB thermal environment is characterized by continuous but variable solar illumination, combined with small coupling to the atmosphere. Extensive shielding is used to regulate the temperature of the instrument. Following the design of BOOMERANG (Crill et al. 2003), BLAST is surrounded by shields comprised of 24 μm thick aluminized Mylar applied to 2.5 cm thick polystyrene open-celled foam. The Mylar side faces out on all surfaces which may be exposed to the Sun. While bare aluminum surfaces can be expected to reach temperatures in excess of 130°C in the LDB float environment, Sun-facing aluminized Mylar surfaces reach temperatures of around 45°C due to their high ratio of thermal IR emissivity to visible light absorptivity. For telescope azimuth ranges of ±60° from anti-Sun, the shielding blocks direct radiation from reaching the optics and all electronics, except for the pivot motor controller and Sun sensor. The actual angles of Sun avoidance have a weak dependence on the elevation of the telescope.

The majority of the electronics dissipate their heat radiatively. A high IR emissivity is achieved by painting electronics enclosures with white paint. Painting white the interiors of boxes aids in radiative transfer between the electronics and the box. This is effective for all boxes, except for the detector readout electronics boxes, each of which dissipate about 100 W. To cool these boxes, emissive vertical plates were installed between each card to couple heat from the electronics to the top and bottom walls of the boxes. A closed-cycle fluid cooling loop was used to distribute the heat to the gondola frame.

The thermal strategy was effective in keeping the temperatures of essentially all electronics well within their operational range. For BLAST06, the shield, added to keep the Sun from illuminating the secondary mirror, reflected solar radiation back onto the pivot motor controller. This increased the average temperature of the pivot by up to 20°C compared to what was experienced in BLAST05. As a result, two non-essential observations where shortened when the motor controller temperature exceeded 62.5°C.

For the 2006 flight, the primary mirror was thermally isolated from the inner frame with G10 spacers and a several layer of Mylar Superinsulation was added in the gap between the mirror and the frame. This stabilized the in-flight temperature that had a diurnal excursion of about 3°C.

Please, see Table 5 and Figure 10 for a list of temperatures achieved during the various BLAST flights.

10. Power System

Solar panels provide power to the flight electronics. They are mounted on the support structure for the Sun shields, at the back of the telescope, and are unfolded sideways at port and starboard (Figure 6). The panels face the Sun from only one side and are radiatively cooled to the sky from the other side.

During normal operation, BLAST requires 540 W, divided between two completely isolated systems: the receiver, and the rest of the gondola. During line-of-sight operations, an additional 160 W are required to power the transmitters. Power is provided by the solar power

[19] Applied Physics, model 534.

[20] WMM-2005, National Geospatial-Intelligence Agency (NGA).

system[21] which charges NiMH batteries[22]. The arrays provide 1250 W for normal incidence at float. The arrays are thus able to provide full power to the experiment up to a Sun-array angle of $> 60°$. The batteries are essentially only used during launch and ascent.

As a NiMH battery reaches its top-off voltage, its charge efficiency decreases, leading to heating of the battery. Additionally, the topoff voltage of NiMH batteries decreases with increased temperature. This combination can lead to thermal runaway if the batteries are charged with a fixed top-off voltage. For BLAST, the charge controllers were modified to allow the fight computer to reduce the top-off voltage as the battery temperature increases, permitting full battery charge without thermal runaway.

11. Flight Planning

BLAST is designed to target multiple regions with a variety of science goals. Unlike a ground-based telescope at a fixed geographic location, the visibility constraints for BLAST change in real-time. The instantaneous region of the sky that is available varies with time, and location of the payload. Finally, the launch date and time are highly uncertain; for every launch opportunity, a new flight plan must therefore be created.

BLAST functions autonomously using schedule files that consist of a sequential list of observations or actions as a function of the Local Sidereal Time. This system is robust against temporary system failures because the telescope only needs to know the current time and location to resume operation upon recovery. Using a local sidereal clock rather than a clock fixed in some time zone, it is possible to account for purely astronomical visibility constraints using a static description, such as the RA of the Sun and of the astronomical targets. It has the disadvantage that the duration the telescope spends on a given observation will vary depending on telescope longitudinal drifts.

A schedule file generator was developed to interpret a high-level description of the desired scientific observations, (e.g. map a circular region centered at a given RA and DEC with a given radius). It also accounts for a number of parameters: the launch date and time, projected duration of flight, the start longitude and latitude, a guess for the termination longitude, a latitude range for the payload, and the position of the Sun and the Moon. With this information the scheduler generates an optimized list of consecutive actions. At each instant, observations that are possible under the current visibility constraints are scheduled in order of priority. At regular intervals, calibration observations are assigned maximum priority, so that sensitivity, beam shape, and pointing variations may be tracked throughout the flight. Once a schedule file is generated, a simple model for the power usage of the system, and the charge rate of the solar panels as a function of Sun incidence angle, is used to calculate the available battery charge over time. The schedule is modified if this model indicates that the batteries will have less than 50% of the total charge capacity at any point in the flight. Schedules are then tested using a simulator that mimics the scanning motion of the telescope to determine the coverage (effective integration time across the maps), and cross-linking among each of the maps for a given flight trajectory.

For every launch opportunity, six schedule files are generated. The latitude of the gondola can change by as much as $\sim 15°$ during a flight, hence three different schedules are created in latitude bands that are 6° wide, with 1° of overlap. The gondola uses the GPS to decide which schedule file to use. Two sets of these three schedules are made: the first set assumes the instrument is working with the target sensitivities; the second assumes degradations of the telescope beam size by a factor of $\sqrt{2}$, and sensitivity by a factor of 2. At the beginning of the flight, the sensitivities are estimated from scans across calibrators. Based on this information the ground station team can decide which of the two sets of schedule files the instrument should use, and switch between the two using a single command, if required.

12. Pointing Reconstruction

Post-flight pointing reconstruction estimates the rotation (attitude) of the gondola with respect to the celestial sphere as a function of time, pro-

[21] MEER Instruments, Palomar Mountain, CA, http://www.meer.com/ and SunCat Solar, Phoenix, AZ.

[22] Cobasys Model 9500.

viding RA, Dec, and rotation angle information at each sample of the detectors. The star camera provides absolute attitude on an unevenly sampled time grid (~1.5 s), with an accuracy of $< 2''$ rms. Each solution is sampled at a known phase with respect to the detectors. The detector and gyroscope sampling are synchronized; therefore, the integration of the gyroscopes gives one estimate of the gondola attitude. The star camera is used to correct the random walk drift induced by the integrated gyroscope noise and as an estimate of the integration constant. BLAST implements a Kalman filter approach to estimate the attitude, expressed as the state quaternion $q(t)$, a 4 dimensional quantity describing the solid body rotation of the gondola. The non-linear state model representing the gondola is defined as

$$\begin{cases} \vec{b}_{n+1} = \vec{b}_n + \vec{w}_{bn} \\ q_{n+1} = \begin{pmatrix} 1 \\ \frac{1}{2}\left(\vec{\omega}_n + \vec{b}_n + \vec{w}_{\omega n}\right)\Delta T \end{pmatrix} q_n \end{cases} \quad (1)$$

where $\vec{\omega}_n$ is the gyro angular velocity with $\vec{w}_{\omega n}$ its noise, $\vec{b}_n$ is the gyro bias, $\vec{w}_{bn}$ is the filter process noise and ΔT is the time resolution of the system (10 ms). The filter is run forward and backward in time and the two solutions are weighed together, using the Kalman covariance matrix output from the filter as the weight. Using just one star camera and the digital gyros, the final averaged attitude is better than $5''$ rms; one example is shown in Figure 11 using data from the BLAST05 flight. The achieved precision is sufficient for BLAST beam sizes, but can be improved once the second set of gyroscopes and the additional star camera are included in the solution. An improvement of $\sqrt{2}$ to 2 better can be reasonably expected. The pointing solution is referenced to the star camera reference frame and needs to be rotated into the submillimeter array coordinate frame. Bright optical and submillimeter point sources are used to evaluate the rotation quaternion Q to apply.

The correction Q is ideally static, but, in practice, was found to be a weak function of time. As shown in Figure 6, the star cameras are mounted at the top of the inner frame, and a structural deformation of the frame can modify the relative orientation between the cameras and the submillimeter beam. Therefore, several pointing calibrators are observed each time the geometry of the scan changes. This effect can be as large as $35''$ and has an 80% correlation with the elevation, and a 25% correlation with the temperature of inner frame. Although it is possible to model the effect based on the gondola thermometry and attitude, Q is such a weak function of time that this was found unnecessary.

13. Conclusion

BLAST is a unique instrument designed to probe the local and high-z Universe at short submillimeter wavelengths. Over the course of two science flights, BLAST has addressed a broad range of Galactic and extragalactic topics. The balloon environment requires a novel combination of ground and satellite technology and techniques. This paper is intended to serve as a reference for a suite of science papers from the BLAST05 and BLAST06 flights.

The BLAST collaboration acknowledges the support of NASA through grant numbers NAG5-12785, NAG5-13301 and NNGO-6GI11G, the Canadian Space Agency (CSA), the UK Particle Physics & Astronomy Research Council (PPARC), Canada's Natural Sciences and Engineering Research Council (NSERC), the Canada Foundation for Innovation, the Ontario Innovation Trust, the Puerto Rico Space Grant Consortium, the Fondo Istitucional para la Investigacion of the University of Puerto Rico, and the National Science Foundation Office of Polar Programs; C. B. Netterfield also acknowledges support from the Canadian Institute for Advanced Research. L. Olmi would like to acknowledge Pietro Bolli for his help with Physical Optics simulations during the testing phase of the BLAST06 telescope. We would also like to thank the Columbia Scientific Balloon Facility (CSBF) staff for their outstanding work, the Precision Machining Group at Lawrence Livermore Laboratory, the support received from Amec in the design and construction of the gondola, Daniele Mortari for helpful discussions in the development of the Pyramid code, Dan Swetz for buliding the Fourier transform spectrometer, and Luke Bruneaux, Kyle Lepage, Danica Marsden, Vjera Miovic, and James Watt for their contribution to the project.

REFERENCES

Ade, P. A. R., Pisano, G., Tucker, C., & Weaver, S. 2006, in Presented at the Society of Photo-Optical Instrumentation Engineers (SPIE) Conference, Vol. 6275, Millimeter and Submillimeter Detectors and Instrumentation for Astronomy III. Edited by Zmuidzinas, Jonas; Holland, Wayne S.; Withington, Stafford; Duncan, William D.. Proceedings of the SPIE, Volume 6275, pp. 62750U (2006).

Bock, J. J., Delcastillo, H. M., Turner, A. D., Beeman, J. W., Lange, A. E., & Mauskopf, P. D. 1996, in ESA SP-388: Submillimetre and Far-Infrared Space Instrumentation, ed. E. J. Rolfe & G. Pilbratt, 119–+

Bohm, K., Petermann, K., & Weidel, E. 1982, Optics Letters, 7, 180

Chattopadhyay, G., Glenn, J., Bock, J. J., Rownd, B. K., Caldwell, M., & 2003, M. J. G. 2003, IEEE Trans. Micro. T. Tech

Crill, B. P., Ade, P. A. R., Artusa, D. R., Bhatia, R. S., Bock, J. J., Boscaleri, A., Cardoni, P., Church, S. E., Coble, K., de Bernardis, P., de Troia, G., Farese, P., Ganga, K. M., Giacometti, M., Haynes, C. V., Hivon, E., Hristov, V. V., Iacoangeli, A., Jones, W. C., Lange, A. E., Martinis, L., Masi, S., Mason, P. V., Mauskopf, P. D., Miglio, L., Montroy, T., Netterfield, C. B., Paine, C. G., Pascale, E., Piacentini, F., Polenta, G., Pongetti, F., Romeo, G., Ruhl, J. E., Scaramuzzi, F., Sforna, D., & Turner, A. D. 2003, ApJS, 148, 527

Devlin, M. J., Ade, P. A. R., Aretxaga, I., Bock, J. J., Chung, J., Chapin, E., Dicker, S. R., Griffin, M., Gundersen, J., Halpern, M., Hargrave, P., Hughes, D., Klein, J., Marsden, G., Martin, P., Mauskopf, P. D., Netterfield, B., Olmi, L., Pascale, E., Rex, M., Scott, D., Semisch, C., Truch, M., Tucker, C., Tucker, G., Turner, A. D., & Weibe, D. 2004, in Presented at the Society of Photo-Optical Instrumentation Engineers (SPIE) Conference, Vol. 5498, Millimeter and Submillimeter Detectors for Astronomy II. Edited by Jonas Zmuidzinas, Wayne S. Holland and Stafford Withington Proceedings of the SPIE, Volume 5498, pp. 42-54 (2004)., ed. C. M. Bradford, P. A. R. Ade, J. E. Aguirre, J. J. Bock, M. Dragovan, L. Duband, L. Earle, J. Glenn, H. Matsuhara, B. J. Naylor, H. T. Nguyen, M. Yun, & J. Zmuidzinas, 42–54

Griffin, M. J., Bock, J. J., & Gear, W. K. 2002, Appl. Opt., 41, 6543

Griffin, M. J., Swinyard, B. M., & Vigroux, L. G. 2003, in Presented at the Society of Photo-Optical Instrumentation Engineers (SPIE) Conference, Vol. 4850, IR Space Telescopes and Instruments. Edited by John C. Mather . Proceedings of the SPIE, Volume 4850, pp. 686-697 (2003)., ed. J. C. Mather, 686–697

Hargrave, P., Waskett, T., Lim, T., & Swinyard, B. 2006, in Presented at the Society of Photo-Optical Instrumentation Engineers (SPIE) Conference, Vol. 6275, Millimeter and Submillimeter Detectors and Instrumentation for Astronomy III. Edited by Zmuidzinas, Jonas; Holland, Wayne S.; Withington, Stafford; Duncan, William D.. Proceedings of the SPIE, Volume 6275, pp. 627514 (2006).

Holland, W., MacIntosh, M., Fairley, A., Kelly, D., Montgomery, D., Gostick, D., Atad-Ettedgui, E., Ellis, M., Robson, I., Hollister, M., Woodcraft, A., Ade, P., Walker, I., Irwin, K., Hilton, G., Duncan, W., Reintsema, C., Walton, A., Parkes, W., Dunare, C., Fich, M., Kycia, J., Halpern, M., Scott, D., Gibb, A., Molnar, J., Chapin, E., Bintley, D., Craig, S., Chylek, T., Jenness, T., Economou, F., & Davis, G. 2006, in Presented at the Society of Photo-Optical Instrumentation Engineers (SPIE) Conference, Vol. 6275, Millimeter and Submillimeter Detectors and Instrumentation for Astronomy III. Edited by Zmuidzinas, Jonas; Holland, Wayne S.; Withington, Stafford; Duncan, William D.. Proceedings of the SPIE, Volume 6275, pp. 62751E (2006).

Hughes, D. H., Aretxaga, I., Chapin, E. L., Gaztañaga, E., Dunlop, J. S., Devlin, M. J., Halpern, M., Gundersen, J., Klein, J., Netterfield, C. B., Olmi, L., Scott, D., & Tucker, G. 2002, MNRAS, 335, 871

Lamarre, J. M., Giard, M., Pointecouteau, E., Bernard, J. P., Serra, G., Pajot, F., Désert, F. X., Ristorcelli, I., Torre, J. P., Church, S.,

Coron, N., Puget, J. L., & Bock, J. J. 1998, ApJ, 507, L5

Lasker, B. M., Jenkner, H., & Russell, J. L. 1987, NASA STI/Recon Technical Report N, 88, 30547

Mather, J. C. 1984, Appl. Opt., 23, 584

Mortari, D., Junkins, J. L., & Samaan, M. A. 2001, Lost-in-Space Pyramid Algorithm for Robust Star Pattern Recognition, AAS Paper 01-004 of the 22th Annual AAS Rocky Mountain Guidance and Control

Olmi, L. 2001, Int. J. of Infrared and Millim. Waves, 22, 791

Olmi, L. 2002, in Presented at the Society of Photo-Optical Instrumentation Engineers (SPIE) Conference, Vol. 4849, Highly Innovative Space Telescope Concepts Edited by Howard A. MacEwen. Proceedings of the SPIE, Volume 4849, pp. 245-256 2002., ed. H. A. MacEwen, 245–256

—. 2007, Applied Optics, Accepted for publication, 791

Patanchon, G. et al. 2007, ApJ, submitted

Rex, M., Chapin, E., Devlin, M. J., Gundersen, J., Klein, J., Pascale, E., & Wiebe, D. 2006, in Presented at the Society of Photo-Optical Instrumentation Engineers (SPIE) Conference, Vol. 6269, Ground-based and Airborne Instrumentation for Astronomy. Edited by McLean, Ian S.; Iye, Masanori. Proceedings of the SPIE, Volume 6269, pp. 62693H (2006).

Rownd, B., Bock, J. J., Chattopadhyay, G., Glenn, J., & Griffin, M. J. 2003, in Presented at the Society of Photo-Optical Instrumentation Engineers (SPIE) Conference, Vol. 4855, Millimeter and Submillimeter Detectors for Astronomy. Edited by Phillips, Thomas G.; Zmuidzinas, Jonas. Proceedings of the SPIE, Volume 4855, pp. 510-519 (2003)., ed. T. G. Phillips & J. Zmuidzinas, 510–519

Truch, M. et al. 2007, ApJ, submitted

Turner, A. D., Bock, J. J., Beeman, J. W., Glenn, J., Hargrave, P. C., Hristov, V. V., Nguyen, H. T., Rahman, F., Sethuraman, S., & Woodcraft, A. L. 2001, Appl. Opt., 40, 4921

This 2-column preprint was prepared with the AAS LaTeX macros v5.2.

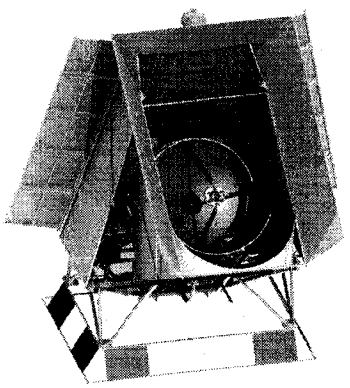

Fig. 7.— A CAD model of the gondola, showing BLAST fully assembled in the BLAST06 configuration. The electronics can cool radiatively through the triangular gaps which are visible in the sun shields. These gaps always point away from the sun in flight.

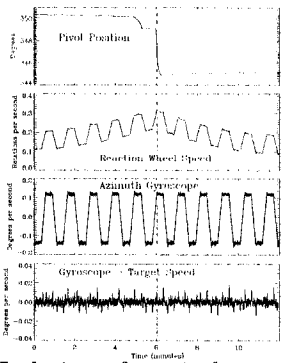

Fig. 8.— Isolation of vertical torques. All panels show data from the same 12 minute segment of the 2006 flight, during which time the telescope was executing a routine azimuthal scan. The third panel shows a trapezoidal angular velocity profile corresponding to constant angular velocity scans connected by constant angular accelerations. The third panel also includes a plot of the desired angular speeds, completely buried by the measured signal. The second panel shows that azimuthal speed is governed by accelerating and decelerating the speed of the reaction wheel. A torque at the pivot proportional to reaction wheel speed reaches threshold and overcomes the stiction in the pivot when the reaction wheel speed is near 0.3 revolutions per second. One such event is marked by the vertical dashed line in all panels. The bottom panel contains a plot of the difference between measured gyroscope signal and desired azimuthal speed. Notice that there are small spikes visible corresponding to the corners in the scan speed but that there is no azimuthal motion of the telescope itself coincident with the release of stiction in the pivot.

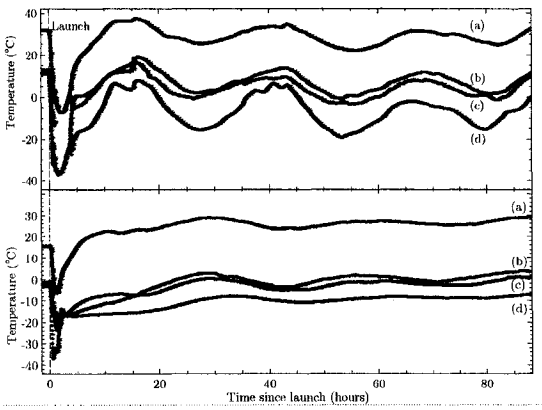

Fig. 10.— Temperatures during the Northern Hemisphere (top panel) and antarctic (bottom) flights: Several gondola temperatures are plotted for the period starting just before launch and extending through the first few days from both science flights. Dramatic cooling in the troposphere, reheating in the stratosphere and diurnal variations due to variation of the solar elevation angle are visible in all traces. The curves are a: the pressure vessel containing the data acquisition computers, b: the gondola inner frame, c: the elevation axis motor and d: the primary mirror. The temperature difference between high power consumption electronics (a) and more passive components (b and c) is only slightly larger at float than it is on the ground. The primary mirror has the best geometry for cooling radiatively and therefore attains the coldest temperature. Notice the relatively large variations in the primary mirror temperature in the 2005 flight which caused us to recognize the need for in-flight focussing capability.

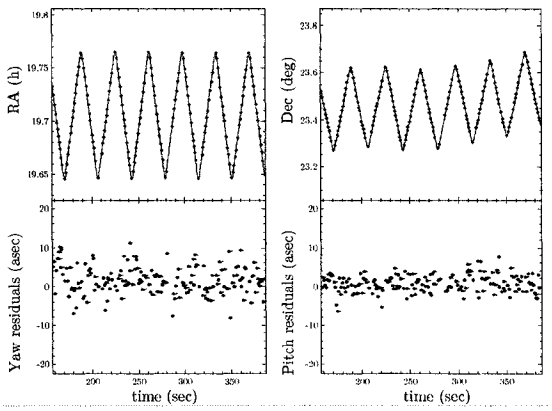

Fig. 11.— An example of pointing reconstruction from the BLAST05 data. In the top plots, the solid blue lines represent the reconstructed pointing solution obtained integrating one set of gyroscopes onto one of the two star cameras. Dots represent the positions reported by the other star camera, which is not used in the solution. The bottom panels show the residuals as yaw ($\sim \Delta\mathrm{RA} * \cos(\mathrm{Dec})$) and pitch (coincident with Dec in this particular case). The yaw residuals are slightly wider, since the telescope scans in azimuth, which is close to RA at the BLAST05 latitudes. The projection of the gongola angular velocity along the yaw axis is always larger than the pitch axis for the elevation range of the telescope (25°–60°), and hence the star centroids in star camera images have larger measurement errors in that direction. The overall error of the pointing solution can be obtained by summing in quadrature the standard deviations of the residuals, yielding $\simeq 4.2''$ rms. Improvements to this result are discussed in Section 12

TABLE 1

BLAST OPTICS DESIGN SUMMARY.

Element	BLAST05	BLAST06
Mirror Diameter	2 m	1.8 m
Focal Length	10 m	9 m
Field Taper	–15 db	–7.5 db
Obscuration	14%	7%
FWHM 250μm	40″	30″
FWHM 350μm	58″	42″
FWHM 500μm	75″	60″
Overall transmission	—— 30% ——	

NOTE.—The BLAST05 instrument used a larger mirror which was under-illuminated. In order to maintain the point-source detectability, the BLAST06 telescope was more aggressively illuminated.

TABLE 2

SUMMARY OF RELEVANT DETECTOR CHARACTERISTICS.

	250 μm	350 μm	500 μm
Light detectors	139	88	43
Dark pixels	2	2	2
Resistors	1	1	1
Thermistors	2	2	2
G (pW/K)	880	640	480
$\Delta(K)$		50	
R_0 (Ω)		55	
R_L (MΩ)		$7+7$	
τ (ms)		2	
Temperature (mK)		270	
NEP (W Hz$^{-1/2}$)		3×10^{-17}	

NOTE.—Bolometer parameters are given for a typical array pixel. Δ and R_o define the bolometric model, $R(T) = R_0\, e^{\sqrt{\Delta/T}}$, while the optical time constant, τ, and the thermal conductance, G, define its thermal behavior. The NEP is computed at 1 Hz.

TABLE 3

WEIGHTS OF THE MAIN COMPONENTS ON THE PAYLOAD.

Component	Weight (kg)
Inner Frame	**705**
Frame	120
Mirror	115
Cryostat (empty)	215
Electronics	65
Cryogens	85
Outer Frame	**1100**
Batteries	80
Solar Panels	30
Electronics	110
Sun Shields	195
Frame	195
CSBF Hardware & Electronics	**215**
Total Weight at Launch	**2020**

NOTE.—Bold face values refer to the BLAST06 configuration and include the items shown here as well as all the other elements on the gondola. The total weight at launch was measured at the hook of the launch vehicle before take-off.

TABLE 4
SPECIFICATIONS OF THE TWO CCD STAR CAMERAS

Camera	PMI 1401	Retiga EXi
Pixels	1312 × 1024	1360 × 1036
Pixel Size	6.8 μm × 6.8 μm	6.45 μm × 6.45 μm
Dynamic range	14 bit	12 bit
Well Depth	45,000 e^-	18,000 e^-

NOTE.—The cameras are manufactured by QImaging (http://www.qimaging.com/). Though both star cameras are nearly identical, the PMI 1401 has deeper pixel wells. It was also found to have a lower measured optical efficiency, significant readout noise and gain variations across the chip compared to the Retiga EXi. However, despite requiring longer integration times to reach a given s.n.r., the greater dynamic range of the PMI 1401 afforded by the extra well depth enabled it to function in backgrounds 1.6 times larger than for the Retiga EXi. The shape of the spectral response for each camera is similar with peaks in the range 400 nm – 850 nm.

TABLE 5
BLAST TEMPERATURES (°C).

	BLAST03		BLAST05		BLAST06		
	Trop	Diurnal	Trop	Diurnal	Trop	Diurnal	Model
ACS 5V DCDC[a]	25	51 to 23	15	62 to 46	3.6	41 to 36	...
ACS Case[b]	...	...	–30	21 to 1	–21	16 to 10	28 to 13
PV Case[c]	...	...	–21	21 to 13	–21	17 to 12	18 to 4
PV Air	–5	26 to 1	–7	35 to 24	–6	24 to 29	...
Preamp Case[d]	–20	10 to –10	...	31 to 19	–5	25 to 21	25 to 19
Inner Frame	–16	-2 to –27	–22	14 to –2	–32	–2 to –5	...
Batteries[f]	10	17 to 10	-3	21 to 10	–6	19 to 17	16 to 0
Solar Panels[g]	...	...	–30	66 to 5	–29	79 to 58	85
Mylar Shields	–30	17 to –55	–34	18 to –4	–38	20 to 10[h]	...
Primary Mirror	–24	–8 to –38	...	8 to –15	–17	–6 to –9	–25 to –10
Secondary Mirror	–33	0 to –70	...	...	–26	–13 to –16[i]	...
Pivot	–33	15 to –50	–38	20 to –5	–35	57 to 36[j]	...
Outer Frame[k]	–11	–1.4 to –37	–30	5 to –13	–24	2 to –3	25 to –5
Star Camera	...	...	–11	15 to 1	–12	6 to 1	18 to 5
Sun Sensor[l]	0	31	–23	43 to 30	...	...	...

NOTE.—BLAST temperatures in the three flights, and as predicted by a Thermal Desktop (http://www.thermaldesktop.com/) model for BLAST06. The model predicted larger diurnal variations than observed, partially because BLAST06 followed a very southerly track, where the sun elevation varied less than the simulation's track. The *Trop* column gives the minimum temperature the component reached during ascent through the Tropopause. The *Diurnal* column gives the daily range of temperatures. In some cases, there was slowly increasing temperature over and above the diurnal variation, due to UV degradation of the Mylar shields.

[a]The inside of the case was painted white before BLAST06.

[b]Partially painted white.

[c]Painted white.

[d]Painted white + cooling loop.

[f]Packaged in a foam box.

[g]The model neglects current draw.

[h]Increased by 20°C over 12 days.

[i]Increased by 5°C over 12 days.

[j]Increased by 4°C over 12 days

[k]Measured at the lock motor near the elevation bearing.

[1]With cooling pump to heat exchanger.

Bibliography

[1] J.-L. Puget, A. Abergel, J.-P. Bernard, F. Boulanger, W. B. Burton, F.-X. Desert, and D. Hartmann. Tentative detection of a cosmic far-infrared background with COBE. *A. A.*, 308:L5+, April 1996.

[2] D. J. Fixsen, E. Dwek, J. C. Mather, C. L. Bennett, and R. A. Shafer. The Spectrum of the Extragalactic Far-Infrared Background from the COBE FIRAS Observations. *ApJ*, 508:123–128, November 1998.

[3] I. Smail, R. J. Ivison, and A. W. Blain. A Deep Sub-millimeter Survey of Lensing Clusters: A New Window on Galaxy Formation and Evolution. *ApJL*, 490:L5+, November 1997.

[4] D. H. Hughes, S. Serjeant, J. Dunlop, M. Rowan-Robinson, A. Blain, R. G. Mann, R. Ivison, J. Peacock, A. Efstathiou, W. Gear, S. Oliver, A. Lawrence, M. Longair, P. Goldschmidt, and T. Jenness. High-redshift star formation in the Hubble Deep Field revealed by a submillimetre-wavelength survey. *Nature*, 394:241–247, July 1998.

[5] E. Kreysa, H.-P. Gemuend, J. Gromke, C. G. Haslam, L. Reichertz, E. E. Haller, J. W. Beeman, V. Hansen, A. Sievers, and R. Zylka. Bolometer array development at the Max-Planck-Institut fuer Radioastronomie. In T. G. Phillips, editor, *Proc. SPIE Vol. 3357, p. 319-325, Advanced Technology MMW, Radio, and Terahertz*

Telescopes, Thomas G. Phillips; Ed., volume 3357 of *Presented at the Society of Photo-Optical Instrumentation Engineers (SPIE) Conference*, pages 319–325, July 1998.

[6] A. W. Blain, I. Smail, R. J. Ivison, J.-P. Kneib, and D. T. Frayer. Submillimeter galaxies. *Phys. Rep.*, 369:111–176, October 2002.

[7] S. C. Chapman, A. W. Blain, R. J. Ivison, and I. R. Smail. A median redshift of 2.4 for galaxies bright at submillimetre wavelengths. *Nature*, 422:695–698, April 2003.

[8] I. Smail, R. J. Ivison, A. W. Blain, and J.-P. Kneib. The nature of faint submillimetre-selected galaxies. *MNRAS*, 331:495–520, March 2002.

[9] D. B. Sanders and I. F. Mirabel. Luminous Infrared Galaxies. *Annu. Rev. Astron. Atrophys.*, 34:749–+, 1996.

[10] R. Genzel and C. J. Cesarsky. Extragalactic Results from the Infrared Space Observatory. *Annu. Rev. Astron. Atrophys.*, 38:761–814, 2000.

[11] D. Hughes. Obscured Star Formation in the High-Redshift Submillimetre Universe. In S. Aalto, S. Huttemeister, and A. Pedlar, editors, *The Neutral ISM in Starburst Galaxies*, volume 320 of *Astronomical Society of the Pacific Conference Series*, pages 317–+, December 2004.

[12] M. J. Griffin, B. M. Swinyard, and L. G. Vigroux. SPIRE - Herschel's Submillimetre Camera and Spectrometer. In J. C. Mather, editor, *IR Space Telescopes and Instruments. Edited by John C. Mather . Pr oceedings of the SPIE, Volume 4850, pp. 686-697 (2003).*, volume 4850 of *Presented at the Society of Photo-Optical Instrumentation Engineers (SPIE) Conference*, pages 686–697, March 2003.

[13] D. H. Hughes, I. Aretxaga, E. L. Chapin, E. Gazta naga, J. S. Dunlop, M. J. Devlin, M. Halpern, J . Gundersen, J. Klein, C. B. Netterfield, L. Olmi, D. Scott,

and G. Tucker. Breaking the 'redshift deadlock'- I. Constraining the star formati on history of galaxies with submillimetre photometric redshifts. *MNRAS*, 335:871–882, October 2002.

[14] E. Pascale et al. The Balloon-borne Large Aperture Submillimeter Telescope: BLAST. *ApJ, submitted*, June 2007.

[15] Ruze J. Antenna tolerance theory–a review. *Proceedings of the IEEE*, 54(4):633–640, 1966.

[16] M. J. Griffin, J. J. Bock, and W. K. Gear. Relative performance of filled and feedhorn-coupled focal-plane architectures. *Applied Optics*, 41:6543–6554, November 2002.

[17] B. P. Crill. *A Measurement of the Angular Power Spectrum of the Cosmic Microwave Background with a Long Duration Balloon-borne Receiver.* PhD thesis, California Institute of Technology, 2001.

[18] B. Rownd, J. J. Bock, G. Chattopadhyay, J. Glenn, and M. J. Griffin. Design and performance of feedhorn-coupled bolometer arrays for SPIRE. In T. G. Phillips and J. Zmuidzinas, editors, *Millimeter and Submillimeter Detectors for Astronomy. Edited by Phillips, Thomas G.; Zmuidzinas, Jonas. Proceedings of the SPIE, Volume 4855, pp. 510-519 (2003).*, volume 4855 of *Presented at the Society of Photo-Optical Instrumentation Engineers (SPIE) Conference*, pages 510–519, February 2003.

[19] M. Rex, E. Chapin, M. J. Devlin, J. Gundersen, J. Klein, E. Pascale, and D. Wiebe. BLAST autonomous daytime star cameras. In *Ground-based and Airborne Instrumentation for Astronomy. Edited by McLean, Ian S.; Iye, Masanori. Proceedings of the SPIE, Volume 6269, pp. 62693H (2006).*, volume 6269 of *Presented at the Society of Photo-Optical Instrumentation Engineers (SPIE) Conference*, July 2006.

[20] Chr. Sterken and J. Manfroid. *Astronomical Photometry.*

[21] J. D. Jackson. *Classical Electrodynamics.*

[22] C. W. Allen. *Astrophysical Quantities.* The Athlone Press, third edition edition.

[23] A. Berk, L.S. Bernstein, and D.C. Robertson. Modtran: A moderate resolution model for lowtran 7. Technical report, ir Force Geophysics Laboratory.

[24] http://www.grc.nasa.gov/WWW/K 12/airplane/atmosmet.html.

[25] T. E. Montroy, P. A. R. Ade, R. Bihary, J. J. Bock, J. R. Bond, J. Brevick, C. R. Contaldi, B. P. Crill, A. Crites, O. Doré, L. Duband, S. R. Golwala, M. Halpern, G. Hilton, W. Holmes, V. V. Hristov, K. Irwin, W. C. Jones, C. L. Kuo, A. E. Lange, C. J. MacTavish, P. Mason, J. Mulder, C. B. Netterfield, E. Pascale, J. E. Ruhl, A. Trangsrud, C. Tucker, A. Turner, and M. Viero. Spider: a new balloon-borne experiment to measure cmb polarization on large angular scales. In *Ground-based and Airborne Telescopes. Edited by Stepp, Larry M.. Proceedings of the SPIE, Volume 6267, pp. 62670R (2006).*, volume 6267 of *Presented at the Society of Photo-Optical Instrumentation Engineers (SPIE) Conference*, July 2006.

[26] P. Oxley, P. A. Ade, C. Baccigalupi, P. deBernardis, H.-M. Cho, M. J. Devlin, S. Hanany, B. R. Johnson, T. Jones, A. T. Lee, T. Matsumura, A. D. Miller, M. Milligan, T. Renbarger, H. G. Spieler, R. Stompor, G. S. Tucker, and M. Zaldarriaga. The ebex experiment. In *Infrared Spaceborne Remote Sensing XII. Edited by Strojnik, Marija. Proceedings of the SPIE, Volume 5543, pp. 320-331 (2004).*, 2004.

[27] Y. Ogasaka, J. Tueller, K. Yamashita, P. Serlemitsos, R. Shibata, K. Tamura, A. Furuzawa, T. Miyazawa, R. Takahashi, M. Sakashita, K. Shimoda, Y. Tawara, H. Kunieda, T. Okajima, H. Krimm, S. Barthelmy, Y. Soong, K.-W. Chan, S. Owens, M. Rex, E. Chapin, and M. Devlin. First light of a hard-x-ray imaging experiment: the InFOCuS balloon flight. In O. Citterio and S. L. O'Dell, editors, *Optics for EUV, X-Ray, and Gamma-Ray Astronomy II. Edited by Citterio, Oberto; O'Dell,*

Stephen L. Proceedings of the SPIE, Volume 5900, pp. 217-224 (2005)., volume 5900 of *Presented at the Society of Photo-Optical Instrumentation Engineers (SPIE) Conference*, pages 217–224, August 2005.

[28] B. M. Lasker, H. Jenkner, and J. L. Russell. The guide star catalog. *NASA STI/Recon Technical Report N*, 88:30547–+, July 1987.

[29] Daniele Mortari, John Lee Junkins, and Malak Anees Samaan. Lost–in–Space Pyramid Algorithm for Robust Star Pattern Recognition. AAS Paper 01–004 of the 22th Annual AAS Rocky Mountain Guidance and Control, January 31–February 4, 2001.

[30] Daniele Mortari, Malak Anees Samaan, Christian Bruccoleri, and John Lee Junkins. The Pyramid Star Identification Technique. *Navigation*, 51(3):171–183, Fall 2004.

[31] Daniele Mortari. Search-Less Algorithm for Star Pattern Recognition. *Journal of the Astronautical Sciences*, 45(2):179–194, April–June 1997.

[32] Vali V. and Shorthill R.W. Fiber ring interferometer. *Appl. Opt.*, 1976.

[33] Post E.J. Sagnac effect. *Review of modern physics*, 1967.

[34] Herve C. Lefevre. In *Proc. of SPIE's Conference.*

[35] D. W. Allan. Statistics of atomic frequency In *Proc. of the IEEE.*

[36] Smith A. M. Polarization and magnetooptic properties of single-mode optical fiber. *Appl. Opt.*, 1972.

[37] P. Yeh and C. Gu. In *Optics of Liquid Crystal Displays*, pages 75–86. New York: Wiley, 1999.

[38] W. R. Hamilton. In *Elements of Quaternions.*

[39] A. Mishenko and Y. Solovyov. Quaternions. *Quantum*, 11:4–17, 2000.

[40] E. W. Kamen and J. K. Su. *Introduction to Optimal Estimation.* Springer, 1999.

[41] C. J. MacTavish. *CMB Angular Power Spectra ans Cosmological Implications from the 2003 Flight od the BOOMERANG Telescpe.* PhD thesis, University of Toronto, 2006.

[42] L. M. Coyle, G. Aurilio, G. U. Nystrom, J. Bortz, B. G. Nagy, K. V. Chance, and W. A. Traub. Design of a single-axis platform for balloon-borne remote sensing. *Rev. Sci. Instrum.*, 1986.

[43] W. A. Traub, K. V. Chance, and L. M. Coyle. Performance of a single-axis platform for balloon-borne remote sensing. *Rev. Sci. Instrum*, 1986.

[44] P. Horowitz and W. Hill. *The Art of Electronics.* Cambridge University Press, 1989.

[45] P. A. R. Ade, G. Pisano, C. Tucker, and S. Weaver. A review of metal mesh filters. In *Millimeter and Submillimeter Detectors and Instrumentation for Astronomy III. Edited by Zmuidzinas, Jonas; Holland, Wayne S.; Withington, Stafford; Duncan, William D.. Proceedings of the SPIE, Volume 6275, pp. 62750U (2006).*, volume 6275 of *Presented at the Society of Photo-Optical Instrumentation Engineers (SPIE) Conference*, July 2006.

[46] D. H. Martin and E. Puplett. "polarised interferometric spectrometry for the millimetre and submillimetre spectrum". *Infrared Phys.*, 1969.

[47] D. H. Martin and E. Puplett. Polarizing (martin-puplett) interferometric spectrometers for millimeter and submillimeter spectra. *Infrared and Millimeter Waves*, 1982.

[48] G. Patanchon et al. SANEPIC: a map-making method for timestream data from large arrays. *ApJ, submitted*, June 2007.

[49] G. Bianchini, U. Cortesi, L. Palchetti, and E. Pascale. Cosmic ray spikes localization and correction in ft spectrometer data. *Infrared Phys. Technol.*, 2002.

[50] William H. Press, Brian P. Flannery, Saul A. Teukolsky, and William T. Vetterling. *Numerical Recipes: The Art of Scientific Computing.* Cambridge University Press, 1992.

[51] P. de Bernardis. Experimental tecniques in astrophysics.

[52] W. C. Jones. *A Measurement of the Temperature and Polarization Anisotropies in the Cosmic Microwave Background Radiation.* PhD thesis, California Institute of Technology, 2006.

[53] S. Prunet, C. B. Netterfield, E. Hivon, and B. P. Crill. Iterative map-making for scanning experiments. *ArXiv Astrophysics e-prints*, June 2000.

[54] J. Delabrouille, J.-F. Cardoso, and G. Patanchon. Multidetector multicomponent spectral matching and applications for cosmic microwave background data analysis. *MNRAS*, 346:1089–1102, December 2003.

[55] K. Coppin, E. L. Chapin, A. M. J. Mortier, S. E. Scott, C. Borys, J. S. Dunlop, M. Halpern, D. H. Hughes, A. Pope, D. Scott, S. Serjeant, J. Wagg, D. M. Alexander, O. Almaini, I. Aretxaga, T. Babbedge, P. N. Best, A. Blain, S. Chapman, D. L. Clements, M. Crawford, L. Dunne, S. A. Eales, A. C. Edge, D. Farrah, E. Gaztañaga, W. K. Gear, G. L. Granato, T. R. Greve, M. Fox, R. J. Ivison, M. J. Jarvis, T. Jenness, C. Lacey, K. Lepage, R. G. Mann, G. Marsden, A. Martinez-Sansigre, S. Oliver, M. J. Page, J. A. Peacock, C. P. Pearson, W. J. Percival, R. S. Priddey, S. Rawlings, M. Rowan-Robinson, R. S. Savage, M. Seigar, K. Sekiguchi, L. Silva, C. Simpson, I. Smail, J. A. Stevens, T. Takagi, M. Vaccari, E. van Kampen, and C. J. Willott. The SCUBA Half-Degree Extragalactic Survey - II. Submillimetre maps, catalogue and number counts. *MNRAS*, 372:1621–1652, November 2006.

[56] D. Scott, E. Chapin, I. Aretxaga, J. Austermann, K. Coppin, M. Crowe, L. Frey, A. Gibb, M. Halpern, D. Hughes, Y. Kang, S. Kim, J. Lowenthal, T. Perera, A. Pope,

K. Scott, G. Wilson, and M. Yun. A Deep AzTEC Map of the GOODS-North Field. In *American Astronomical Society Meeting Abstracts*, page 125.04, December 2006.

[57] M. Truch et al. The Balloon-borne Large Aperture Submillimeter Telescope (BLAST) 2005: Calibration and Targeted Sources. *ApJ, submitted*, June 2007.

[58] D. Rigopoulou, A. Lawrence, and M. Rowan-Robinson. Multiwavelength energy distributions of ultraluminous IRAS galaxies - I. Submillimetre and X-ray observations. *MNRAS*, 278:1049–1068, February 1996.

[59] L. Dunne and S. A. Eales. The SCUBA Local Universe Galaxy Survey - II. 450-μm data: evidence for cold dust in bright IRAS galaxies. *MNRAS*, 327:697–714, November 2001.

[60] U. Lisenfeld, K. G. Isaak, and R. Hills. Dust and gas in luminous infrared galaxies - results from SCUBA observations. *MNRAS*, 312:433, February 2000.

[61] M. Seiffert, C. Borys, D. Scott, and M. Halpern. An upper limit to polarized submillimetre emission in Arp 220. *MNRAS*, 374:409–414, January 2007.

[62] U. Klaas, M. Haas, S. A. H. Müller, R. Chini, B. Schulz, I. Coulson, H. Hippelein, K. Wilke, M. Albrecht, and D. Lemke. Infrared to millimetre photometry of ultraluminous IR galaxies: New evidence favouring a 3-stage dust model. *A. A.*, 379:823–844, December 2001.

[63] L. Spinoglio, P. Andreani, and M. A. Malkan. The Far-Infrared Energy Distributions of Seyfert and Starburst Galaxies in the Local Universe: Infrared Space Observatory Photometry of the 12 Micron Active Galaxy Sample. *ApJ*, 572:105–123, June 2002.

[64] M. J. Griffin and G. S. Orton. The near-millimeter brightness temperature spectra of Uranus and Neptune. *Icarus*, 105:537–547, October 1993.